INTRA-VEHICLE UWB CHANNEL CHARACTERIZATION AND RECEIVER DESIGN

DISSERTATION FOR THE DEGREE OF
DOCTOR OF PHILOSOPHY IN
ELECTRICAL AND COMPUTER ENGINEERING

WEIHONG NIU

OAKLAND UNIVERSITY

2010

INTRA-VEHICLE UWB CHANNEL CHARACTERIZATION AND RECEIVER DESIGN

by

WEIHONG NIU

A dissertation submitted in partial fulfillment of the
requirements for the degree of

DOCTOR OF PHILOSOPHY IN ELECTRICAL AND COMPUTER ENGINEERING

2010

Oakland University
Rochester, Michigan

DOCTORAL ADVISORY COMMITTEE:

Jia Li, Ph.D., Chair
Manohar Das, Ph.D.
László Lipták, Ph.D.
Gautam B. Singh, Ph.D.

© Copyright by Weihong Niu, 2010
All rights reserved

To My Father and Mother

ACKNOWLEDGMENTS

Many thanks go to Dr. Jia Li, my thesis advisor. She introduced me to the road of Ph.D. research and always gave me her invaluable encouragement and guidance whenever I was stuck in my research. Based on her rich knowledge and experiences in the research area of communications, her suggestions enlightened me when I got lost in choosing the direction of my research topics and guided me to the promising world of Ultra-Wideband communications. In addition, she also gave me great help and always showed her support in overcoming the difficulties I met in life. Her patience and kindness helped create a favorable atmosphere for me which was the key reason I was able to focus on the research work and be here today.

I also would like to give my acknowledgment to Dr. Manohar Das, Dr. László Lipták, Dr. Gautam B. Singh, and Dr. Bo-nan Jiang. As my teachers and my Ph.D. committee members, their teaching prepared me for the Ph.D. research. Their insightful comments and suggestions helped me greatly in improving the work of this dissertation.

Furthermore, I sincerely appreciate General Motors Corporation, especially Dr. Timothy Taulty, for sponsoring my Ph.D. research and for providing the measurement vehicle used in my experiments. Acknowledgment also goes to Dr. Shaojun Liu for his help in conducting the experiment to finish my first publication. In addition, I have to thank Michael Corrigan and Asia Walton a lot for their assistance in conducting the intra-vehicle channel measurement and for their significant contributions in developing and implementing the UWB cluster identification algorithm.

Last but not least, I would like to give great appreciation to my family for their unconditional love and support during my years of Ph.D. study and research.

Weihong Niu

ABSTRACT

INTRA-VEHICLE UWB CHANNEL CHARACTERIZATION
AND RECEIVER DESIGN

by

Weihong Niu

Adviser: Jia Li, Ph.D.

One objective of this research is to characterize Ultra-wideband (UWB) propagation within commercial vehicles and obtain the knowledge of UWB channels in intra-vehicle environments. Channel measurement is performed in time domain for two environments and different multi-path models are used to describe the two different propagation channels. In one environment, the transmitting and the receiving antennas are inside the engine compartment. It is observed that paths arrive in clusters and the classical Saleh-Valenzuela (S-V) model can be used to describe the multi-path propagation. In another environment, both antennas are located beneath the chassis. Clustering phenomenon does not exist in this case and the power delay profile (PDP) in this environment does not start with a sharp maximum but has a rising edge. A modified stochastic tapped delay line model is used to account for this rising edge. Furthermore, for this environment, data are collected for a vehicle in both stationary and moving scenarios. Statistical analysis shows that car movement does not significantly affect the characteristics of UWB channel beneath the chassis.

Clustering phenomenon exists for the Ultra-Wideband (UWB) propagation in many environments. To manually identify clusters in the UWB impulse responses is very difficult and time consuming when a large amount of data needs to be processed. Furthermore, visual inspection highly depends on the person who performs the cluster identification task, which may lead to inconsistent and unrepeatable results. In this

dissertation, an automatic procedure to identify clusters in UWB impulse responses is proposed.

Another objective of this research focuses on the design and performance analysis of digital transmitted reference (TR) UWB receivers with slightly frequency shifted (SFS) reference. Motivated by the flexibility of digital system and the availability of sophisticated digital signal processing circuits, this dissertation proposes a digital implementation of the SFS receiver with low quantization resolution. Performance analysis of such a digital receiver is done based on both the measured channel data from the intra-vehicle UWB environments and the channel impulse responses generated by indoor and outdoor channel models available in literature.

TABLE OF CONTENTS

LIST OF TABLES

LIST OF FIGURES

CHAPTER 1
INTRODUCTION

1.1 Motivation

Electronic subsystems are essential components of modern vehicles. For the purpose of safety, comfort and convenience, an increasing number of electronic sensors are being deployed in the new models of automotives to collect such information as coolant temperature, wheel speed, engine oil pressure and so on. It is reported that the average number of sensors per vehicle already exceeded 27 in 2002 [1] [2]. In the current automotive architecture design, sensors are connected to electronic control unit (ECU) via cables for the transmission of collected data. Due to the large number of sensors, the length of cables used for this purpose can add up to as long as 1000 meters [3]. Although the introduction of CAN networks reduced the amount of cables needed in automotives, the wire harness interconnecting sensors and ECU still contributes at least 50kg to the weight of a vehicle [3]. Adding more sensors will lead to further increase in the length and weight of wires deployed in a vehicle. This not only greatly increases the complication of vehicle architecture design and scalability problem, but also negatively affects the cost, fuel economy and environment friendliness which are becoming more and more important for vehicles nowadays [4] [5]. Furthermore, some sensors like those detecting tire pressure are not possible to be connected with wires.

To counteract these disadvantages existing in current intra-vehicle wired sensor networks, T. ElBatt etc. proposed wireless sensor network as a potential way to reduce the cable bundles for the transmission of data and control information between sensors and ECU [6]. A great challenge in constructing such an intra-vehicle wireless sensor network is to provide acceptable level of reliability, end-to-end latency and data rate compared with what is offered by the current wiring system. Accordingly, selecting a proper physical layer radio technology is crucial in the intra-vehicle propagation environment featuring short range, dense multi-path and highly possible interferences from audio, cell phones and other personal Bluetooth gadgets of the passengers. This dissertation considers impulse-based UWB technology a promising candidate for physical layer solution in constructing an intra-vehicle wireless sensor network due to its robustness in solving multi-path fading issue, resistance to narrow band interference, low power consumption, potential capability of high data rate as well as free availability of bandwidth [7] [8].

1.2 UWB Overview

UWB is defined as the wireless radio which takes a bandwidth larger than 500MHz or a fractional bandwidth greater than 25%, where fractional bandwidth is defined as the ratio of -10dB bandwidth to center frequency [9] [10]. In 2002, FCC authorized the unlicensed use of UWB signals in the frequency range between 3.1GHz and 10.6GHz in USA. However, in order to avoid interference to existing systems operating in this frequency range, the power spectral density emission of a UWB system is limited within -41.3dBm/MHz [11] [10]. In other frequency ranges, the emission is even more restricted. Fig. 1.1 illustrates the UWB emission limits prescribed by FCC for indoor and outdoor communication systems respectively. When a UWB device works indoors, its power spectral density emission can not exceed -41.3dBm/MHz, -75.3dBm/MHz, -53.3dBm/MHz, -51.3dBm/MHz, -41.3dBm/MHz and -51.3dBm/MHz corresponding to the frequency ranges of 0GHz-0.96GHz, 0.96GHz-1.61GHz, 1.61GHz-1.99GHz, 1.99GHz-3.1GHz, 3.1GHz-10.6GHz, 10.6GHz and upper, respectively. In comparison, the emission limits are -41.3dBm/MHz, -75.3dBm/MHz, -63.3dBm/MHz, -61.3dBm/MHz, -41.3dBm/MHz and -61.3dBm/MHz for UWB devices working outdoors in the same set of frequency bands as shown in Table 1.1 [10] [11]. Fig. 1.2 de-

Table 1.1: Emission limits for Indoor and outdoor UWB devices

	Indoor	Outdoor
0.96GHz and lower	-41.3dBm/MHz	-41.3dBm/MHz
0.96-1.61GHz	-75.3dBm/MHz	-75.3dBm/MHz
1.61-1.99GHz	-53.3dBm/MHz	-63.3dBm/MHz
1.99-3.1GHz	-51.3dBm/MHz	-61.3dBm/MHz
3.1-10.6GHz	-41.3dBm/MHz	-41.3dBm/MHz
10.6GHz and upper	-51.3dBm/MHz	-61.3dBm/MHz

scribes the bandwidth comparison between UWB and narrow band TV signal. It can be seen that the FCC definition expect UWB systems to work like background noise as far as the existing devices in the same spectral band are concerned.

According to Shannon-Hartley theorem, the extremely wide transmission bandwidth potentially gives the UWB technology a high capacity to support high data rate applications. Furthermore, the extremely short pulse used in impulse radio based UWB communications means fine delay resolution in time domain, which in turn leads to the lack of significant multi-path fading. At the same time, UWB signals also demonstrate strong resistance to narrow band interference because only a small part of the frequency components will be affected by any narrow band signal. Finally, the impulse-based UWB system also has the advantage to utilize a simple baseband radio receiver design without any carrier as well as the benefit of low power consumption due to low duty cycles [12] [13] [14]. These features make UWB a promising technique for implementing intra-vehicle wireless sensor network.

UWB is not a brand new technology and its history dates back to early twentieth century when G. Marconi experimented transmitting the first wireless signal across the Atlantic Ocean with his spark gap transmitter. But such impulse-based radio system did not get a chance to develop until 50 years later when the experimental appliances to measure and create extremely short pulses were available. Contemporary UWB technology first found its usage in military applications like radar systems or covert communications in the 1960s. Approximately 30 years later, this technology was officially termed UWB. In the 1990s, it seized extensive attention from researchers and companies for its potential use in civil applications. To protect conventional wireless system and to encourage the development of UWB technology, FCC released the first UWB report and order in 2002 [11]. Like Bluetooth and many other developing technologies, the UWB commercialization effort made in industry experienced ups and downs in recent years, but the potential capability of UWB to enable short-range, low-power and high-speed communications still attracts a lot of researchers to continuously work on solving the challenging issues in UWB, including the characterization of UWB channels and the design of UWB receivers that are easy to implement.

1.2.1 Intra-Vehicle UWB Channel Characterization

In order to design a UWB communication system, it is important to understand the UWB signal propagation characteristics in the desired environment. To date, lots of measurement experiments have been performed in outdoor and indoor environments [15] [16] [17] [18] [19] [20]. Moreover, channel models are available to describe the UWB propagation in these environments. For the purpose of forming physical layer standards for WPAN high rate and low rate applications, IEEE 802.15.3a and IEEE 802.15.4a channel modeling subgroup developed their UWB channel models respectively for indoor and outdoor environments [21] [22]. However, only a few channel measurement or channel characterization work has been reported for intra-vehicle environment. The only reported effort relevant to the UWB propagation in vehicle environment is from [23]. But in [23], the measurement was taken in an armored military vehicle, which is different from commercial vehicles in both size and equipments. Furthermore, the commercial vehicle sensors are normally located at such locations like wheel axis or engine compartment etc., but the measuring positions in [23] are either inside the passenger compartment or outdoors in proximity to the vehicle, which are not the typical places where commercial vehicle sensors are deployed. One area this dissertation works on is to investigate the intra-vehicle UWB propagation characteristics in commercial vehicle environments and develop suitable channel models based on the measured data.

1.2.2 Intra-Vehicle UWB Receiver Design

Although the fine time resolution of UWB signaling leads to less significant multi-path fading problem as compared to narrow band signals, it brings a large number of resolvable multi-paths in the power delay profiles. The main challenge in the design of UWB system is the implementation of low-cost, low-complexity and high performance receivers. If RAKE receivers used in conventional spread spectrum systems are employed, tens even hundreds of fingers have to be present in the receiver in order to capture sufficient energy, hence making it too complicated and too costly to implement [24] [25] [26]. Furthermore, the estimation of the delays and weights for these fingers is a difficult task when the noise level is high [27] [28]. In the UWB literature, transmitted reference (TR) receiver attracts the attention of researchers because of its simple structure. TR signaling scheme transmits a reference signal and a data signal in a pair with some delay between them and the receivers just detect the signal by correlating the reference with the data. The appearance of TR receivers dates back to the 1950s and they found their first usage in spread-spectrum system

[29]. R. Hoctor and H. Tomlinson proposed a simple structure of UWB receiver taking advantage of the TR signaling scheme [30] [31]. Recently, a lot of work has been done in the performance analysis and the comparison between TR and rake receivers [32] [33] [34] [35] [36]. Although the architecture of such UWB TR receiver is simple in theory, its practical implementation is overwhelming because an analog delay unit capable of processing an ultra-wideband analog signal is required in the time-shifted TR receiver. It is impossible to provide such a delay unit in a highly integrated mode [37] [38] [39]. To eliminate the need for a time delay unit, a slightly frequency-shifted TR receiver (SFS TR) was proposed in [37] [38] [39]. The performance analysis of such a receiver shows that this kind of receiver works well in low-data-rate applications [37] [38] [39]. Currently, the intra-vehicle UWB sensor network is required to be capable of supporting 100 sensors with each transmitting at least one sample of 16 bits to ECU per second. This is a low-data-rate application [40]. Another area the research work in this dissertation focuses on is the design of a digital UWB receiver which is appropriate for the use in the intra-vehicle environment.

1.3 Contributions

This dissertation reports the channel measurement campaign and the channel characterization of UWB communications in the intra-vehicle environments so that better understanding of the UWB potentials in constructing an intra-vehicle wireless sensor can be obtained. The measurement experiments are divided into two groups. The first group is performed in a static Ford Taurus and a static GM Escalade followed by the channel characterization process based on these measurements. Measurements are performed either inside engine compartments which is none-line-of-sight (NLOS) case or beneath chassis which is line-of-sight (LOS) case. It is proposed that the tapped-delay-line model and the modified S-V model be used to describe the UWB channels beneath the chassis and inside the engine compartment respectively, because clustering phenomenon is observed in the latter environment but not in the chassis case. Channel model parameters are extracted from the measurement data and compared with those of indoor and outdoor environments. These channel characteristics will be helpful in designing the UWB systems to support intra-vehicle wireless sensor networks. The second group of measurements is conducted for the channel beneath the Escalade chassis, while the car is either moving or is stationary. The extracted channel parameters are compared between the moving scenario and the stationary scenario to investigate whether the vehicle movement influences the channel and how significant the influence is. In addition, another contribution of this dissertation is a new algorithm designed to identify the clusters in the UWB impulse responses. As mentioned above, UWB signals always arrive in clusters in the engine compartment and clusters have to be identified first before channel model parameters can be extracted. Due to the large amount of measured channel data, it will be a burdensome job if all of the clusters in the channel impulse responses have to be identified manually. Consequently, an efficient and accurate algorithm is designed in this dissertation to help complete the tedious and heavy work to identify clusters existing in UWB impulse responses.

Compared with analog UWB receivers mentioned in the previous section, digital receivers provide more flexibility. In addition, digitization also provides the benefit of reduction in complexity and the convenience to take advantage of powerful digital signal processing (DSP) circuits which are normally less expensive than analog circuits and easier to upgrade by updating the DSP software. In this dissertation, a digital version of TR receiver with slightly frequency shifted reference is developed. Digitization of the receiver is implemented in two steps. The first step is the sampling of the analog UWB signal with Nyquist rate, and the closed-form performance analysis is done for the full-resolution receiver after the sampling. The correctness of the theoretical performance evaluation is verified by the comparison with simulation results based on both the measured UWB data in the intra-vehicle environment and the generated channel data using 802.15.3a/802.15.4a channel models. The second step is quantization of the samples resulted from the first step with low-bit resolution. Performance of the quantized SFS TR receiver is derived based on quantization theorem. Similarly, the final theoretical performance of this quantized digital SFS TR receiver is validated by the simulations based on the same set of channel data as in the first step.

1.4 Organization of Dissertation

The dissertation is organized in the following way. Chapter 2 describes the measurement experiments. It explains the appliances, the measurement positions and the testing scenarios in detail. Examining the details of the experiment setup is very helpful in understanding the statistical results in the following chapters. The multi-path and pathloss models used to describe the statistical characteristics of different intra-vehicle UWB channels are presented in Chapter 3. In addition, the deconvolution technique used to derive channel impulse responses is also given in this chapter. CLEAN algorithm is explained step by step. Chapter 4 explains the way to extract intra-vehicle UWB channel model parameters via statistical calculation. Both multi-path and pathloss model parameters are deducted from the measurement data. Chapter 5 discusses the influences the vehicle movement brings to the multi-path channel characteristics. Chapter 6 explains a new UWB cluster identification algorithm and demonstrates by examples its effect in processing the clustering UWB impulse responses of the engine compartment environment. Chapter 7 proposes a quantized TR receiver with slightly frequency shifted reference and derives the theoretical expression for the receiver's performance. Finally, Chapter 8 concludes this dissertation by summarizing the channel modeling and receiver evaluation results.

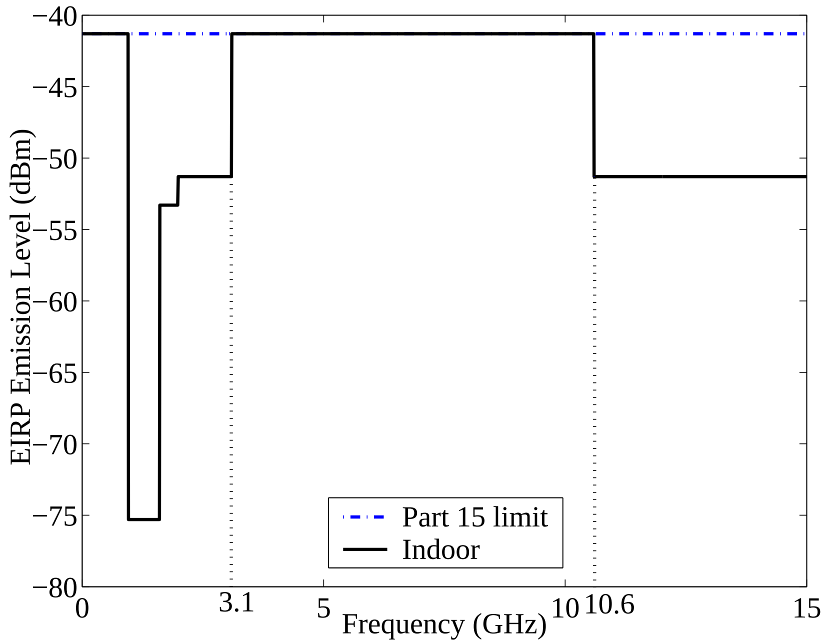

(a) Indoor

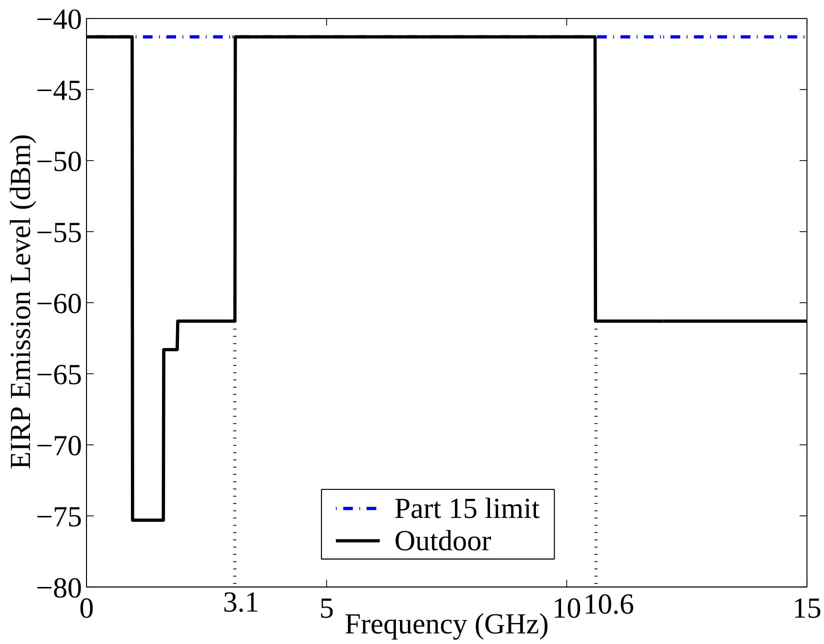

(b) Outdoor

Figure 1.1: Spectrum masks for UWB communications systems.

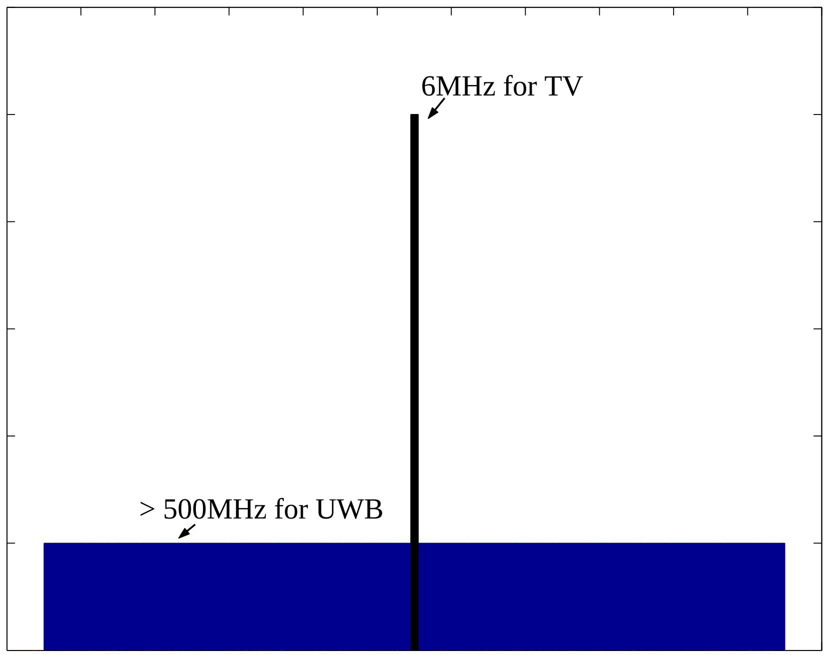

Figure 1.2: Bandwidth comparison between UWB and narrow band signal.

CHAPTER 2
INTRA-VEHICLE UWB CHANNEL MEASUREMENT

2.1 Introduction

One way to characterize a physical channel in time domain is via its impulse response (IR). The channel characteristics which can be extracted from the IR include multi-path profile parameters and power attenuation parameters. Conventionally, in order to get the impulse response of an UWB channel, there are two techniques of channel measurement. The first is to perform channel sounding in time domain by exciting the channel with extremely narrow pulses and recording the responses with a digital oscilloscope. This method provides the direct availability of responding waveforms and the time-variation of the channel can observed easily. The channel impulse responses are obtained by deconvolving the exciting pulses from the responses. However, this method requires a way to create extremely narrow pulses and such a apparatus is normally expensive [41] [42] [43]. A lot of UWB channel measurements have been performed using this technique [44] [45] [46] [47]. The second technique is to conduct channel sounding in frequency domain. A time-varying sinusoidal waveform whose frequency slowly sweeps an UWB frequency band is used to excite the channel and the responding signals are recorded by a Vector Network Analyzer (VNA). These responses are approximately considered to be the channel transfer function. Although normally the apparatus used in this method are available readily, it takes a long time to sweep the frequency range and perform the measurements. As a result, time variation of the channel is very difficult to measure [48] [49]. Frequency domain UWB channel measurements setup can be found in some papers [50] [51]. Due to the availability of an UWB pulse generator in our lab, the intra-vehicle channel measurements have been performed in time domain. The experiments have been divided into two groups. In the first group, measurements are conducted for a Ford Taurus and a GM Escalade when they are parked on the second floor of a large empty three-story parking building at Oakland University. In the second group, channel data has been collected for the Escalade only, in both the moving and the static scenarios. The following sections will explain the details of the setups in these experiments.

2.2 Apparatus

Measurement apparatus needed in the experiment include a pulse generator, a sweeper, two antennas, a high sampling rate large bandwidth digital oscilloscope and the cables. Fig. 2.1 shows the main apparatus and Fig. 2.2 is the block diagram illustrating their connections. At the transmitting side, a Wavetek sweeper and an impulse generator from Picosecond work together to create narrow pulses of width 80 picoseconds. These pulses are fed into a scissors-type antenna. At the receiving side, a digital oscilloscope of 15GHz bandwidth from Tektronix is connected with the receiving antenna to record the received signals. For the purpose of synchronization, three cables of same length are employed. The first cable connects the impulse generator output to the transmitting antenna, the second one connects the receiving antenna and the signal input of the oscilloscope, and the third one is used to connect the impulse generator output to the trigger input of the oscilloscope. This can ensure that all the recorded waveforms at the oscilloscope have the same reference point in time. Hence relative delays of signals arriving at the receiver via different propagation paths can be measured.

2.3 Measurement Setup for Static Taurus and Escalade

The parking building is constructed from cement and mental. In this group of experiments, all channel data were collected in the Escalade first and in the Taurus later. During the experiment, the two vehicles were parked in the same place.

The parking location is in the middle of the building, more than 6 meters away from any wall. Fig. 2.3 is a picture taken when the Escalade is being tested. It shows the building structure and the Escalade in the experiment.

For each vehicle, the measurement was performed in two environments. In the first environment, both the transmitting and the receiving antennas are beneath the chassis and 15cm above the ground. They are set to face each other and the line-of-sight (LOS) path always exists. Fig. 2.4 illustrates the arrangement of the antennas' locations. The transmitting antenna is fixed at location TX in the front, just beneath the engine compartment. The receiving antenna has been moved to ten different spots, namely RX0-RX9. Five of them are located in a row along the left side of the car, with equidistance of 70cm for the Taurus and 80cm for the Escalade between the neighboring spots. The other five sit symmetrically along the right side of the car. Distance between TX and RX1 is 45cm for the Taurus and 50cm for the Escalade. In addition, RX0, RX1, RX8 and RX9 are located very close to the axes of the corresponding wheels. For each position, ten received waveforms were recorded by the oscilloscope when pulses were transmitted repeatedly. When the measurement is being taken, except the carton or package tape to support or attach the antennas to the chassis, there is no other object lying in the space between the metal chassis and the cement ground. Fig. 2.5 is a picture showing the transmitting antenna attached to the Escalade chassis from the bottom. UWB propagation in this environment is measured because there are such sensors as wheel speed detectors installed at the wheel axes in modern vehicles. Sensor signals are transmitted via cables to the ECU, normally located in the front of a car. UWB transmission beneath the chassis is considered by us to be an attractive way of transmitting such sensor signals from the wheel axes or other parts of a vehicle to the ECU.

In the second environment, for each car, the two antennas were put inside the engine compartment with the hood closed. The positions of antennas highly depend on the available space in the compartment. Due to the difference between engine compartment structures of Taurus and Escalade, the arrangement of antenna positions are different as shown in Fig. 2.6. But for both cars, the transmitting antenna is fixed and the receiving antenna has been moved to different spots. Ten waveforms were recorded for each position of the receiving antenna. The engine compartments are full of metal auto components and there are always iron parts sitting between the antennas. Measurement data have been collected for this environment because some sensors like temperature sensors are located in the engine compartment.

2.4 Measurement Setup for Moving and Static Escalade

Most working time of intra-vehicle sensor networks is when vehicles are running on road. It must be investigated if the car movement affects the UWB channel characteristics. Hence a second group of experiment is performed for the Escalade when it is moving around Oakland University campus. The measurement has only been conducted for the environment beneath the chassis because the car movement does not change the material or structure of the engine compartment but the changing ground may bring changes to the channel beneath the chassis. The deployment of the antenna positions are similar to those identified in Fig. 2.4. The distances between neighboring spots are exactly the same as what is described in the above section. At each receiving location, ten continuous UWB pulse responses were recorded when the car is running at a speed between 20 and 45 miles per hour, and another ten were collected when the car is halted but with its engine on.

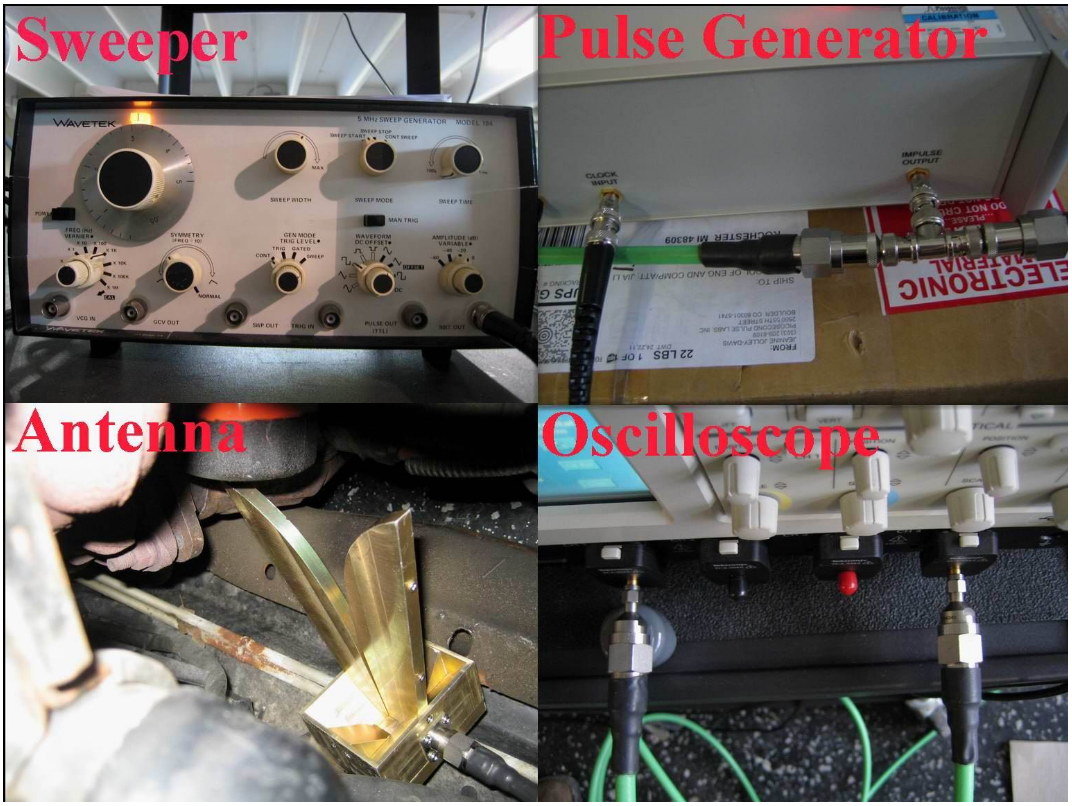

Figure 2.1: Channel sounding apparatus.

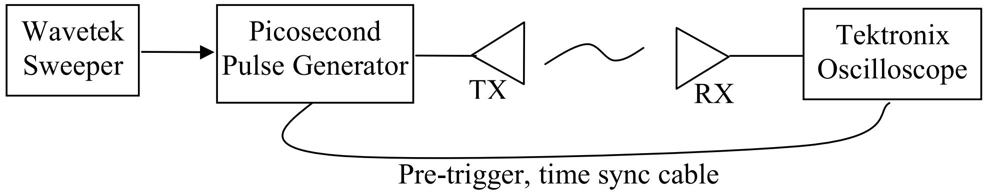

Figure 2.2: Connections of channel sounding apparatus.

Figure 2.3: Parking building and a test vehicle.

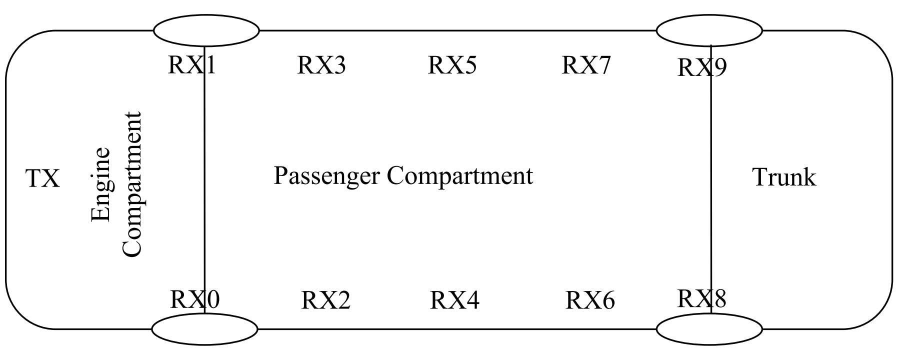

Figure 2.4: Antenna locations for the measurements beneath the chassis.

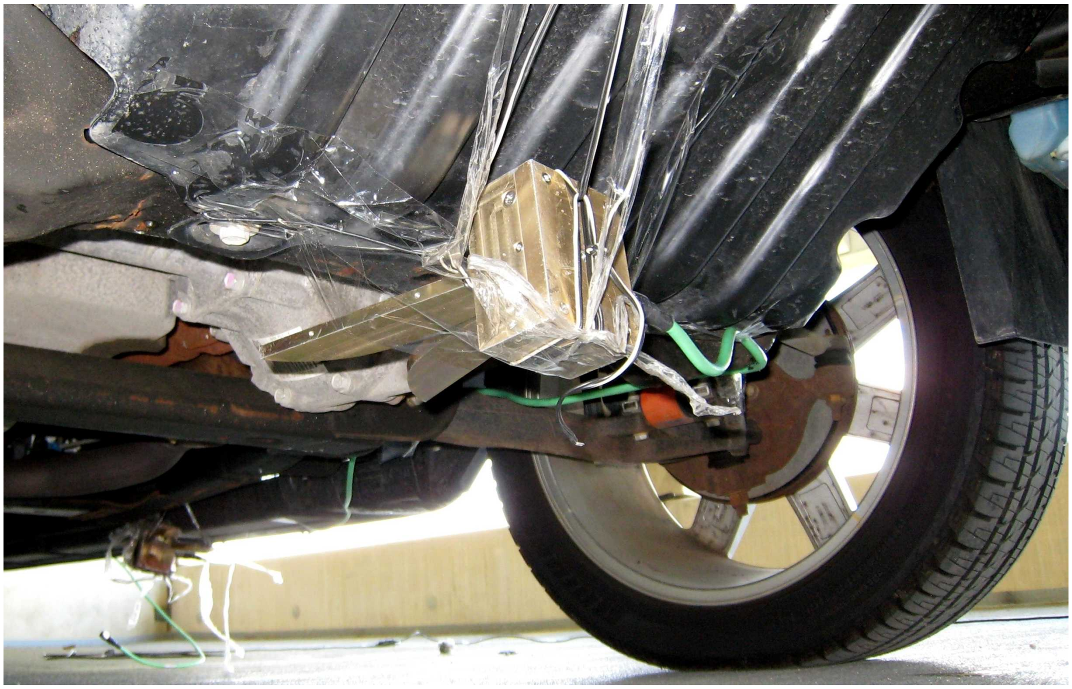

Figure 2.5: Transmitting Antenna Attached to the Chassis.

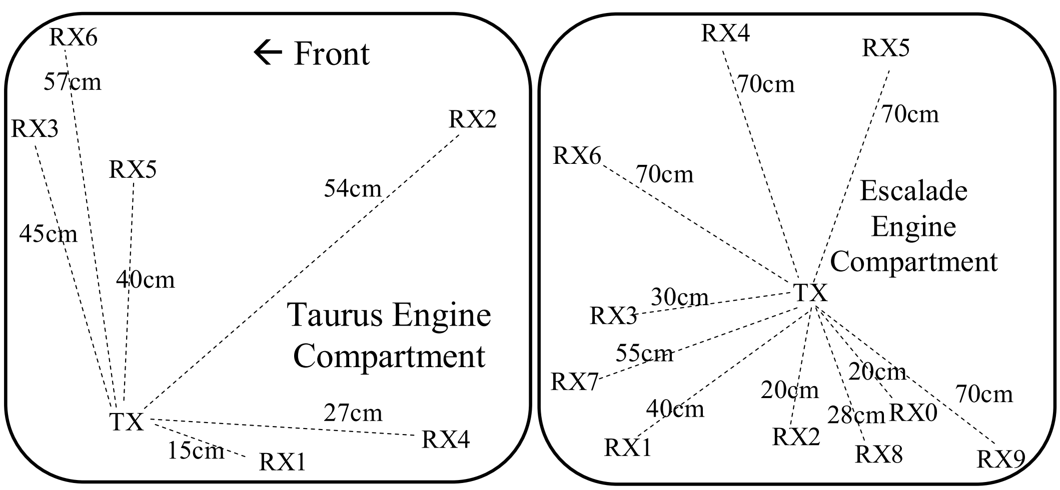

Figure 2.6: Antenna locations for the measurements inside engine compartments.

CHAPTER 3
INTRA-VEHICLE UWB CHANNEL MODELS

3.1 Introduction

In wireless transmissions, the pulse sent out by the transmitting antenna reaches the receiving antenna via different paths due to the reflectors and scatters around the antennas. These paths experience different attenuations and time delays. Hence the waveform recorded at the receiving side is a summation of the signals from these paths. In narrow band communications, these signals interfere with each other and create a seriously distorted version of the transmitted signal. This phenomenon is called multi-path fading and adversely affects the performance of a narrow band system [52] [53] [54]. However, due to the ultra short length of the UWB pulses, signals arriving from different paths do not produce severe interferences and a lot of paths can be recognized in the received waveform. When designing a UWB system, the statistical characteristics of these paths for a propagation channel should be known. A mathematical model used for this purpose is called a multi-path channel model.

This chapter describes the multi-path channel models used in this dissertation for the intra-vehicle UWB propagation inside the engine compartment and beneath the chassis. Because clustering phenomenon exists in the waveforms measured inside the engine compartment but not in those measured beneath the chassis, this dissertation proposes to characterize UWB channels in these two environments with different models. A modified stochastic tapped-delay-line multi-path model is used to describe the UWB propagation beneath the chassis [44] [55]. For the channel inside the engine compartment a modified S-V multi-path model is used [21] [22] [56] [57]. In the experiments, it is observed that for a fixed antenna position there is little difference between the waveforms recorded at different time points when sequences of pulses are transmitted periodically. Thus both of the multi-path channel models for these two environments are time-invariant.

3.2 Deconvolution

The multi-path characteristic of a channel is represented by its impulse responses (IR) in time domain. Multi-path channel model is the statistical mathematic expression describing the channel impulse response. Because each measured waveform is the convolution of the UWB channel IR, the sounding pulse, and the IR of the apparatus including the antennas, the cables and the oscilloscope. Deconvolution must be applied in the first place to extract the channel impulse response from the measured data. In this dissertation, the subtractive deconvolution technique, so called CLEAN algorithm, is employed. CLEAN algorithm was originally used in radio astronomy to reconstruct images [58] [59]. Later it was used to find channel impulse response. As described by Rodney G. Vaughan and Neil L. Scott in their paper [60], when CLEAN algorithm is used as a way of deconvolution, it assumes that any measured multi-path signal $r(t)$ is the sum of a weighted pulse $p(t)$ arriving at different time. The channel impulse response is deconvolved by iteratively subtracting $p(t)$ from $r(t)$ until the remaining energy of $r(t)$ falls below a threshold. In our case, $p(t)$ is the waveform recorded by the oscilloscope when the two antennas are set to be one meter above the ground and one meter away from each other. The shape of $p(t)$ is shown in Fig. 3.1.

In detail, the algorithm is summarized as below [60]:

1. Initialize the dirty signal with $d(t) = r(t)$ and the clean signal with $c(t) = 0$;

2. Initialize the damping factor γ, which is usually called loop gain, and the detection threshold T, which is used to control the stopping time of the algorithm;

3. Calculate $x(t) = p(t)\overline{\otimes}d(t)$, where $\overline{\otimes}$ represents the normalized cross correlation;

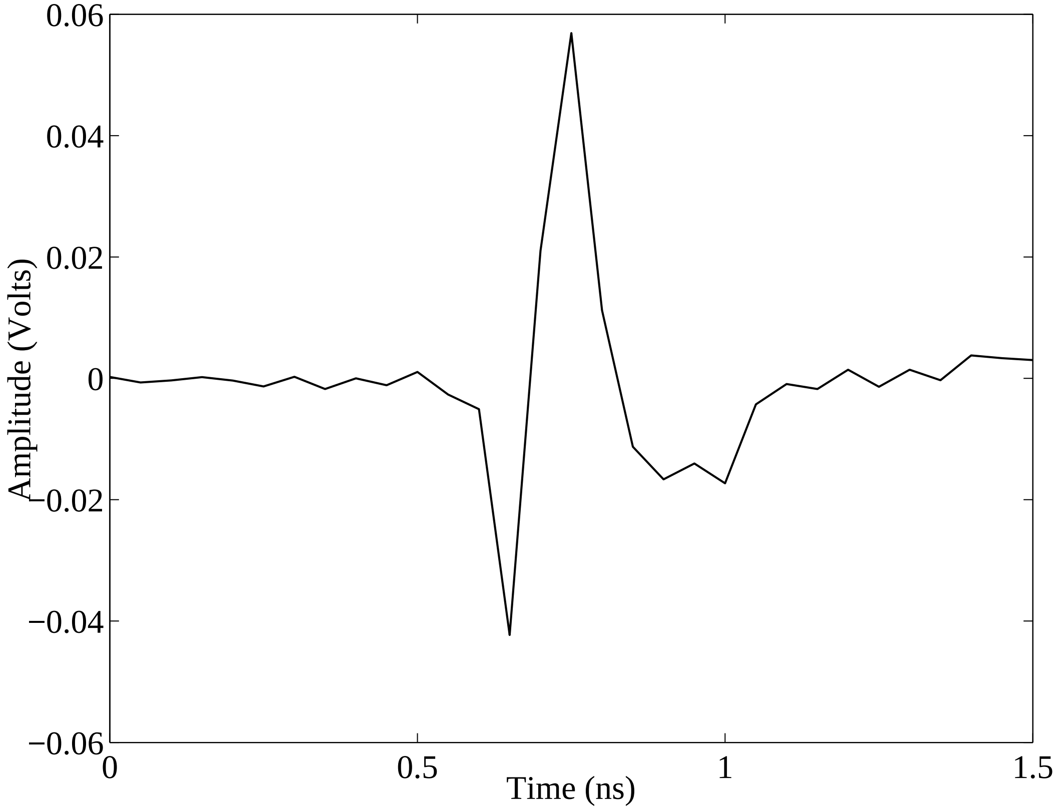

Figure 3.1: Received UWB signal when receiving antenna is 1m away from transmitting antenna.

4. Find the peak value P and its time position τ in $x(t)$;
5. If the peak signal P is below the threshold T, stop the iteration;
6. Clean the dirty signal by subtracting the multiplication of $p(t)$, P and γ : $d(t) = d(t) - p(t-\tau) \cdot P \cdot \gamma$;
7. Update the clean signal by $c(t) = c(t) + P \cdot \gamma \cdot \delta(t - \tau)$;
8. Loop back to step 3;
9. $c(t)$ is the channel impulse response.

The impulse response generated by this algorithm is determined by the value of the loop gain γ and the threshold of the stop criteria T. In our deconvolution process, based on the balance of the computation time and the algorithm performance, γ is set to 0.01 and T is set to 0.04. Fig. 3.2 shows an example of a received signal from beneath the chassis and the impulse response obtained via CLEAN algorithm. Each vertical line in the impulse response figure represents a multi-path component (MPC) whose relative time delay and strength are indicated by the time position and amplitude of the line. An example of measured waveforms from the UWB propagation inside the engine compartments is shown in Fig. 3.3 together with the impulse response. Observation of the recorded waveforms and the deconvolved impulse responses reveals that paths arrive in clusters in this environment. But for the measurements taken beneath the chassis, there is no clustering phenomenon observed. This observation is consistent with the structure of the channels. Normally, the multiple rays reflected from a nearby obstacle arrive with close delays, tending to form a cluster. Strong reflections from another obstacle separated in distance tend to form another cluster. The combined effects result in multiple clusters in an impulse response. Inside the engine compartments, there are auto parts sitting between or nearby the transmitter and the receiver. But the channel beneath the chassis only consists of the air, the ground and the chassis, without other obstacles sitting in the vicinity of the transmitter or receiver. The lack of multiple scattering obstacles leads to the lack of multiple clusters in this environment.

3.3 Tapped Delay Line Model for UWB Propagation Beneath the Chassis

Narrowband propagation channel impulse response can be represented as

$$h(t) = \sum_{k=0}^{K} \alpha_k \exp(j\theta_k)\delta(t - \tau_k), \tag{3.1}$$

where K is the number of multi-path components; α_k are the positive random path gains; θ_k are the phase shifts and τ_k are the path arrival time delays of the multi-path components [61] [62] [63]. θ_k is considered to be a uniformly distributed random variable in the range of $[0, 2\pi)$. However, as stated in [64] [65] [66] [67] [68] [69] [70], for

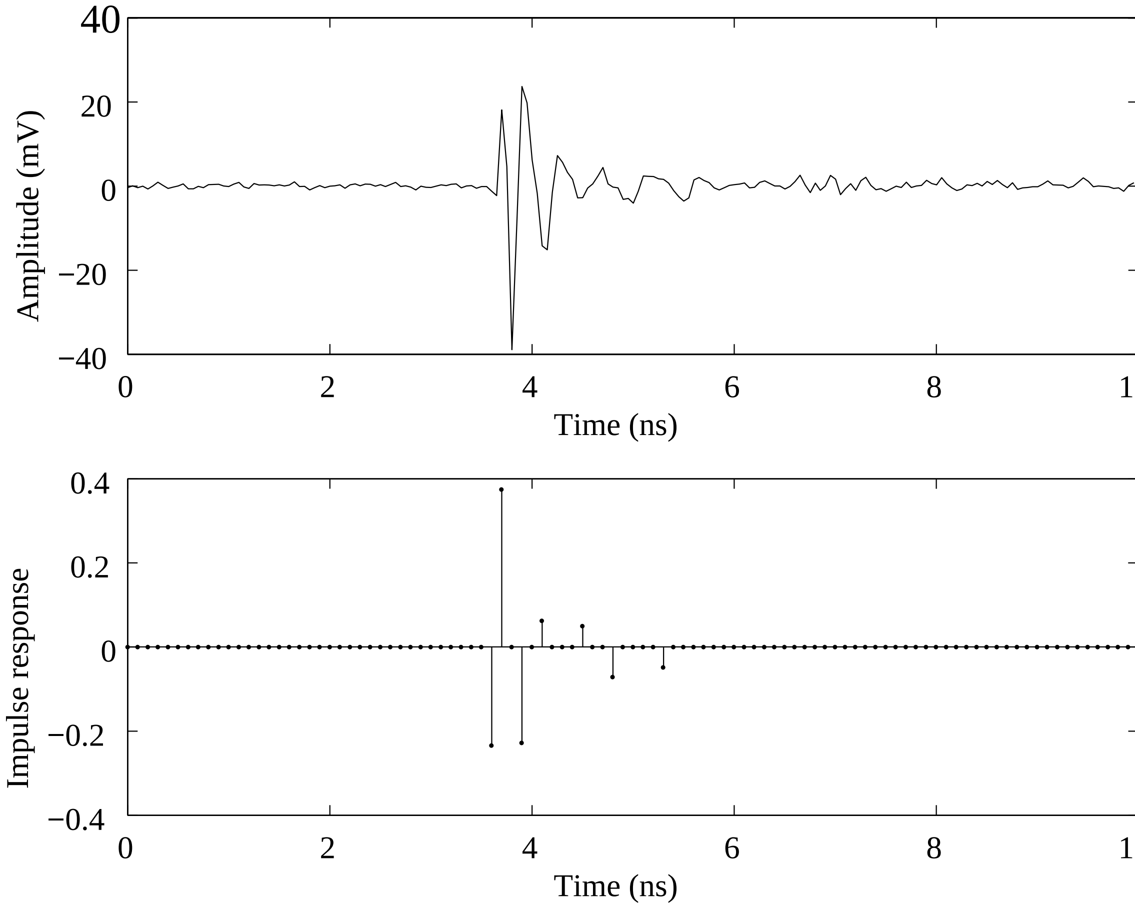

Figure 3.2: Example of received waveform and the corresponding CIR for under-chassis environment.

UWB channels, because of the frequency selectivity in the reflection, diffraction or scattering processes, MPCs experience distortions and the impulse response should be written as

$$h(t) = \sum_{k=0}^{K} \alpha_k \chi_k \exp(j\theta_k)\delta(t - \tau_k), \tag{3.2}$$

in which χ_k denotes the distortion of the kth MPC. In this dissertation, the effect of frequency selectivity will not be considered. The impulse response of the UWB propagation channel beneath the chassis is still described by (3.1) and the phase θ_k equiprobably takes the value 0 or π. In addition, the arrival of the paths is described

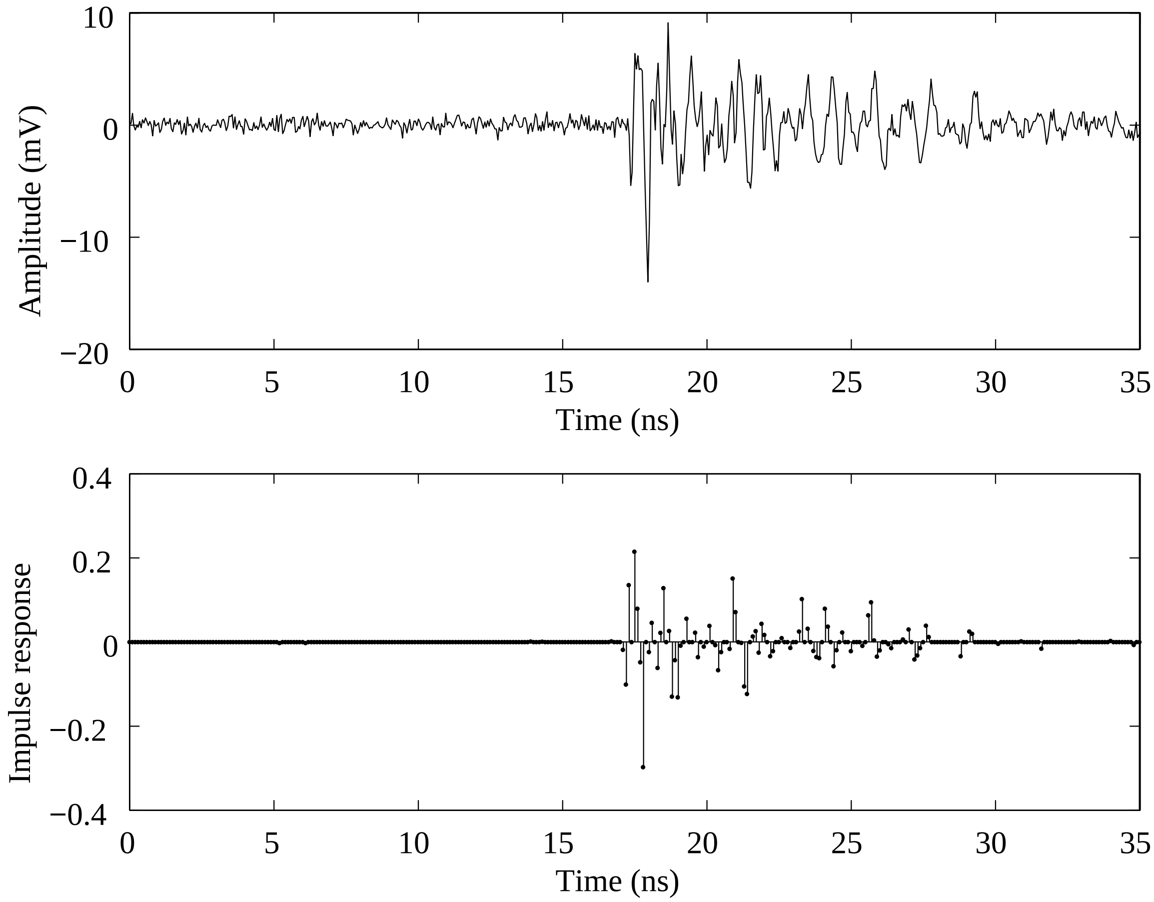

Figure 3.3: Example of received waveform and the corresponding CIR for engine compartment environment.

as a Poisson process and the distribution of arrival intervals is expressed as below

$$p(\tau_k|\tau_{k-1}) = \lambda \exp[-\lambda(\tau_k - \tau_{k-1})], \qquad k > 0, \tag{3.3}$$

where λ is the path arrival rate [57] [71].

The power plot of the IR, which describes the power of each path versus its arrival time, is called power delay profile (PDP) [72]. As for the shape of the power delay profile, measurement results from the chassis environment show that PDPs do not decay monotonically. Instead, each PDP has a rising edge at the beginning, then it reaches the maximum later and decays after that peak. So we adopt the following function proposed in [73] and [74] to describe the mean power of the paths

$$E\{\alpha_k^2\} = \Omega \cdot (1 - \chi \cdot \exp(-\tau_k/\gamma_{rise})) \cdot \exp(-\tau_k/\gamma), \tag{3.4}$$

where τ_k is the arrival delay of the kth path relative to the first path, χ describes the attenuation of the first path, γ_{rise} determines how fast the PDP increases to the maximum peak, γ controls the decay after the peak and Ω is the integrated energy of the PDP.

3.4 S-V Model for UWB Propagation Inside the Engine Compartment

The classical S-V channel model to account for the clustering of MPCs is expressed as

$$h(t) = \sum_{l=0}^{L} \sum_{k=0}^{K} \alpha_{kl} \exp(j\theta_{kl}) \delta(t - T_l - \tau_{kl}), \tag{3.5}$$

where L is the number of clusters, K is the number of MPCs within a cluster, α_{kl} is the multi-path gain of the kth path in the lth cluster, T_l is the delay of the lth cluster, that is, the arrival time of the first path within the lth cluster, assuming the first path in the first cluster arrives at time zero, τ_{kl} is the delay of the kth path within the lth cluster, relative to the arrival time of the cluster, and θ_{kl} is the phase shift of the kth path within the lth cluster [57].

Similar to the chassis model, the MPC distortion of UWB signal mentioned in [64] is not considered in this dissertation and (3.5) has been used to describe the UWB multi-path propagation inside the engine compartment. The phases θ_{kl} are also considered to equiprobably equal 0 or π. In addition, the arrival of the clusters and the arrival of the paths within a cluster are described as two Poisson processes. Accordingly, the cluster interarrival time and the path interarrival time within a cluster obey exponential distribution described by the following two probability density functions [57]

$$p(T_l | T_{l-1}) = \Lambda \exp[-\Lambda(T_l - T_{l-1})], \qquad l > 0, \tag{3.6}$$

$$p(\tau_{kl}|\tau_{(k-1)l}) = \lambda \exp[-\lambda(\tau_{kl} - \tau_{(k-1)l})], \qquad k > 0, \tag{3.7}$$

where Λ is the cluster arrival rate and λ is the path arrival rate within clusters.

Furthermore, S-V model assumes that the average power of both the clusters and the paths within the clusters decay exponentially as below

$$\overline{\alpha_{kl}^2} = \overline{\alpha_{00}^2} \exp(-T_l/\Gamma) \exp(-\tau_{kl}/\gamma), \tag{3.8}$$

where $\overline{\alpha_{00}^2}$ is the expected power of the first path in the first cluster; Γ and γ are the power decay constants for the clusters and the paths within clusters respectively. Normally γ is smaller than Γ, which means that the average power of the paths in a cluster decay faster than the first path of the next cluster.

3.5 Summary

Impulse response is a way to represent the multi-path characteristic of a wireless channel. This chapter first introduces the CLEAN algorithm used to extract the intra-vehicle UWB channel impulse responses. It subtractively deconvolves the exciting ultra-narrow pulse used in time domain channel sounding from the recorded response at the digital oscilloscope. Then this chapter describes the two channel models employed to describe the impulse responses in the two intra-vehicle environments. A modified stochastic tapped-delay-line model, which takes the fast rising edges at the beginning of the impulse responses into consideration, is used to characterize the channel beneath the vehicle chassis. For the channel inside the vehicle engine compartment, the classical stochastic S-V model is suggested to describe the impulse responses and the model parameters are defined and explained in detail.

CHAPTER 4
INTRA-VEHICLE UWB CHANNEL CHARACTERISTICS

4.1 Channel Parameters for Multi-path Model

In this chapter, impulse responses are statistically analyzed to extract channel parameters for the multi-path models. In addition, the pathloss model describing the power attenuation of UWB propagation in the two environments is introduced and the pathloss parameters are extracted from the measurement data. The multi-path parameters are extracted via statistical analysis of the IRs and PDPs from the two environments. When processing those PDPs showing clustering phenomenon, clusters are identified manually via visual inspection. Both the path arrival time and the variations in the amplitudes are considered in the cluster identification process. Generally speaking, when there is no overlap between neighboring clusters, MPCs having similar delays are grouped into a cluster. But when the overlap happens, path amplitude variations will be considered in the identification of clusters. New clusters are identified at the points where there are big variations, normally sudden increase, in the path amplitudes. Fig. 4.1 shows an example of manual cluster identification results in the above two cases. The dotted lines mark the clusters. The upper subfigure illustrates the non-overlapping case and the lower one illustrates the overlapping case.

4.1.1 RMS Delay Spread Distribution

Root-mean-square (RMS) delay spread is the standard deviation value of the delay of paths, weighted proportional to the path power. It is defined as

$$\tau_{rms} = \sqrt{\left[\sum_k (t_k - t_1 - \tau_m)^2 \alpha_k^2\right] / \sum_k \alpha_k^2}, \tag{4.1}$$

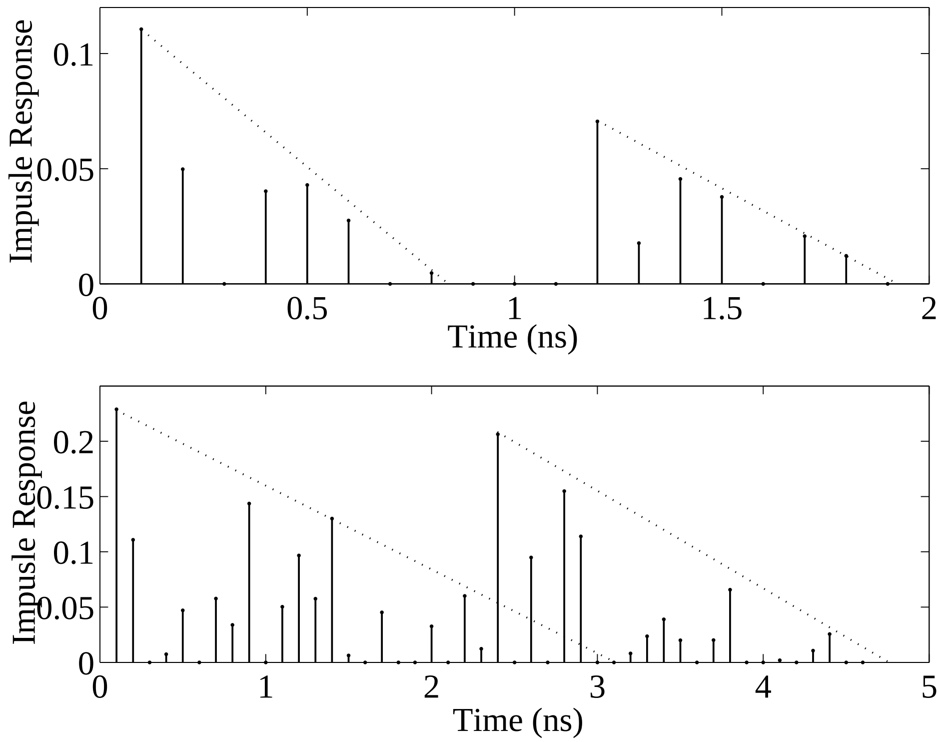

Figure 4.1: Example of manual cluster identfication results.

where t_k and t_1 are the arrival time of the kth path and the first path, respectively; α_k is the amplitude of the kth path; and τ_m is the mean excess delay defined as

$$\tau_m = \left[\sum_k (t_k - t_1)\alpha_k^2\right] / \sum_k \alpha_k^2. \tag{4.2}$$

RMS delay spread is considered to be a good measure of multi-path spread. It indicates the potential of the maximum data rate that can be achieved without intersymbol interference (ISI) [62] [75]. Generally, serious ISI is likely to occur when the symbol duration is larger than ten times RMS delay spread. As an important characteristic of the multi-path channel, RMS delay spread is calculated for each of our deconvolved channel impulse responses. The measured complementary cumulative distribution functions (CCDFs) of the RMS delay spread for the measurements taken beneath the Taurus and Escalade chassis are plotted in Fig. 4.2, with their counterparts for the engine compartment measurements shown in Fig. 4.3. The results show that the mean RMS delay spread in the Taurus and Escalade chassis environment is 0.3101 ns and 0.4431 ns respectively. In the mean time, the engine compartment environment gives the empirical mean RMS delay spread of 1.5918 ns for Taurus and 1.7165 ns for Escalade. All of them are much less than those reported for indoor or outdoor environment, indicating less possibility of serious ISI [21]. Because the multi-path delay spread decreases when the distance between the transmitter and receiver decreases [76], the small RMS delay spreads in our measurement result from the small distance between the antennas. In most cases, they are separated by less than 5 meters, which is much less than that of indoor or outdoor measurement environment. Furthermore, the lack of multiple reflecting obstacles for the chassis environment makes the RMS delay spread even smaller.

4.1.2 Inter-path and Inter-cluster Arrival Times

As stated in Chapter 3, the cluster arrival and intra-cluster path arrival in S-V model are considered to be Poisson arrival processes with fixed rate Λ and λ respectively. Accordingly, their interarrival times have exponential distributions. The method to estimate λ and Λ is to get the empirical cumulative distribution functions (CDFs) of the path and cluster arrival intervals from the measurement data and then find the exponential distribution functions best-fitting them. λ or Λ is just the reciprocal of the mean value of such an exponential distribution function. Following this procedure, $1/\lambda$ for the measurements beneath the Taurus chassis is determined to be 0.2846 ns and it is 0.4101 ns for those beneath the Escalade chassis. In addition, for the data measured inside the Taurus engine compartment, $1/\lambda$ is 0.2452 ns and $1/\Lambda$ equals 3.0791 ns. Their corresponding values for the Escalade are 0.3185 ns and 3.2575 ns respectively. These values are listed in Table 4.1 above and the semi-log plots for the CCDFs of these interarrival times with their best-fit exponential distri-

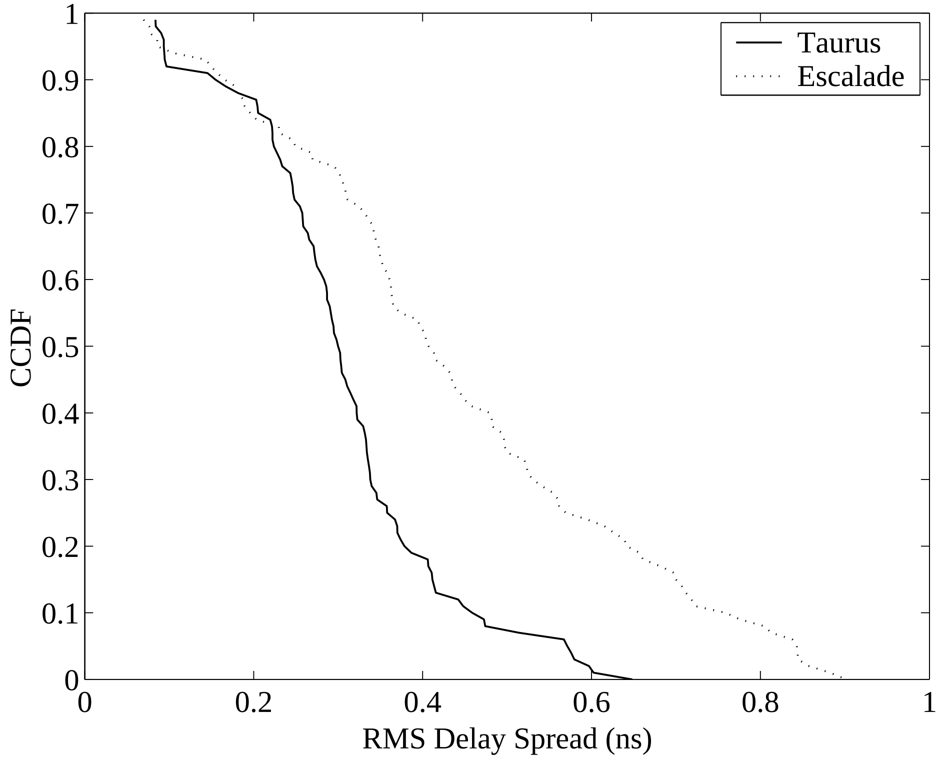

Figure 4.2: CCDF of the RMS delay spread for UWB propagation beneath the chassis.

butions are shown in Fig. 4.4, Fig. 4.5 and Fig. 4.6. In these figures, each best-fit exponential distribution is found in the meaning of maximum likelihood estimation and their mean values just equal the reciprocal of the path or cluster arrival rates. It can be observed that both the path arrival rates and the cluster arrival rates are larger than those reported for indoor or outdoor environments [19] [20] [22] [77]. The reason for these faster arrival rates is due to the much shorter range of the UWB propagation in the intra-vehicle environment. In addition, the fine resolution with a bin width of 0.1 ns used by us contributes to the number of resolved paths, which in turn also contributes to the faster path arrival rates.

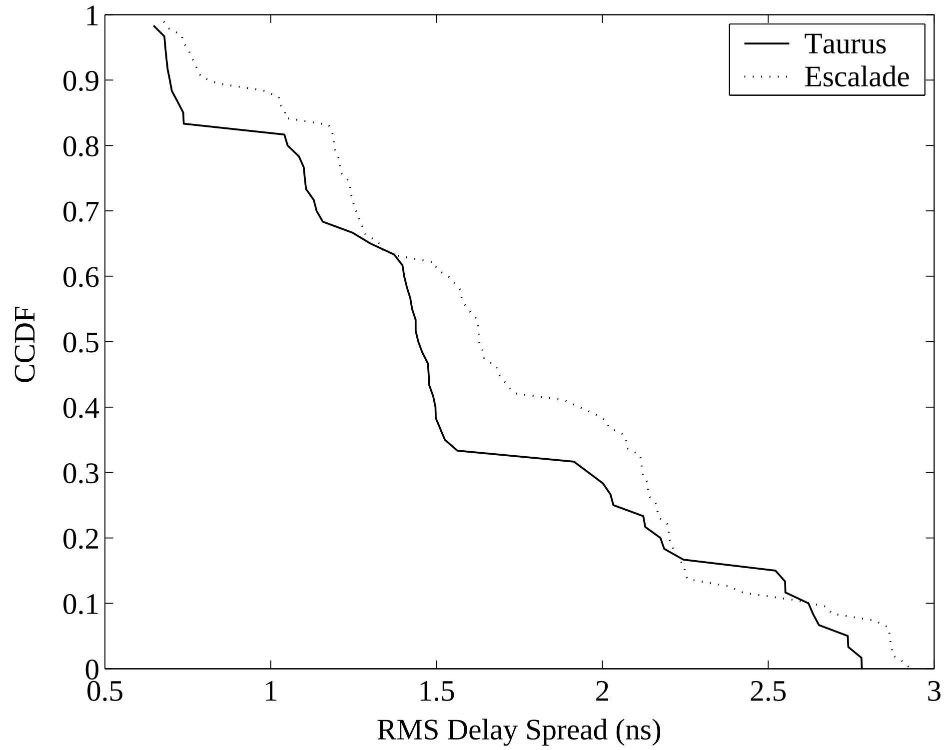

Figure 4.3: CCDF of the RMS delay spread for UWB propagation inside the engine compartments.

4.1.3 Distributions of Path and Cluster Amplitudes

In narrowband models, the amplitudes of the multi-path components are usually assumed to follow Rayleigh distribution, but this is not necessarily the best description of UWB MPCs amplitudes. Due to the ultra-wide bandwidth of the UWB signals, the time delay difference between resolvable paths, which normally equals the reciprocal of the bandwidth, is much smaller than that of the narrowband signals. As a result, each observed UWB MPC is the sum of a much smaller number of unresolvable paths. It is highly possible that the amplitude distribution is not Rayleigh. To evaluate the distributions of UWB path and cluster amplitudes, this dissertation matches the empirical CDF of the measured amplitudes against Rayleigh and Lognormal to find out which one is a better fit.

Table 4.1: Reciprocal of path and cluster arrival rates

Rate reciprocal	Chassis		Engine Compartment	
	Taurus	Escalade	Taurus	Escalade
$1/\lambda(ns)$	0.2846	0.4101	0.2452	0.3185
$1/\Lambda(ns)$	N/A	N/A	3.0791	3.2575

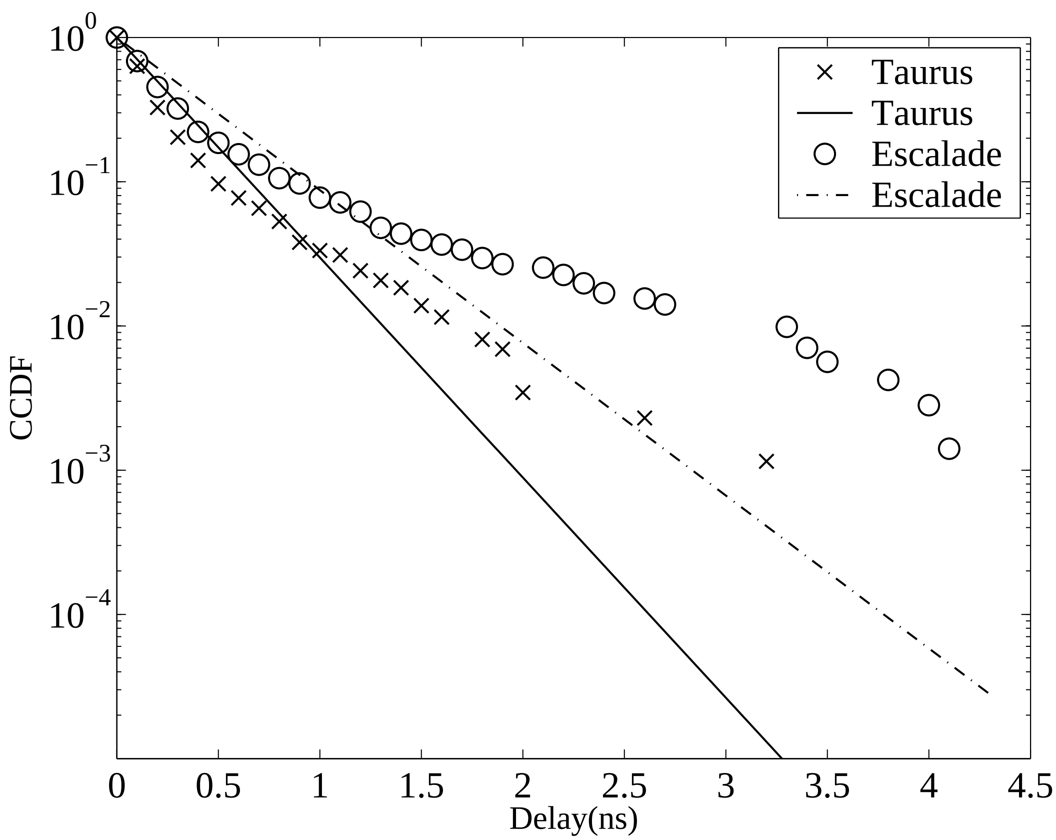

Figure 4.4: CCDF of inter-path arrival intervals and the best-fit exponential distributions for measurements beneath the chassis.

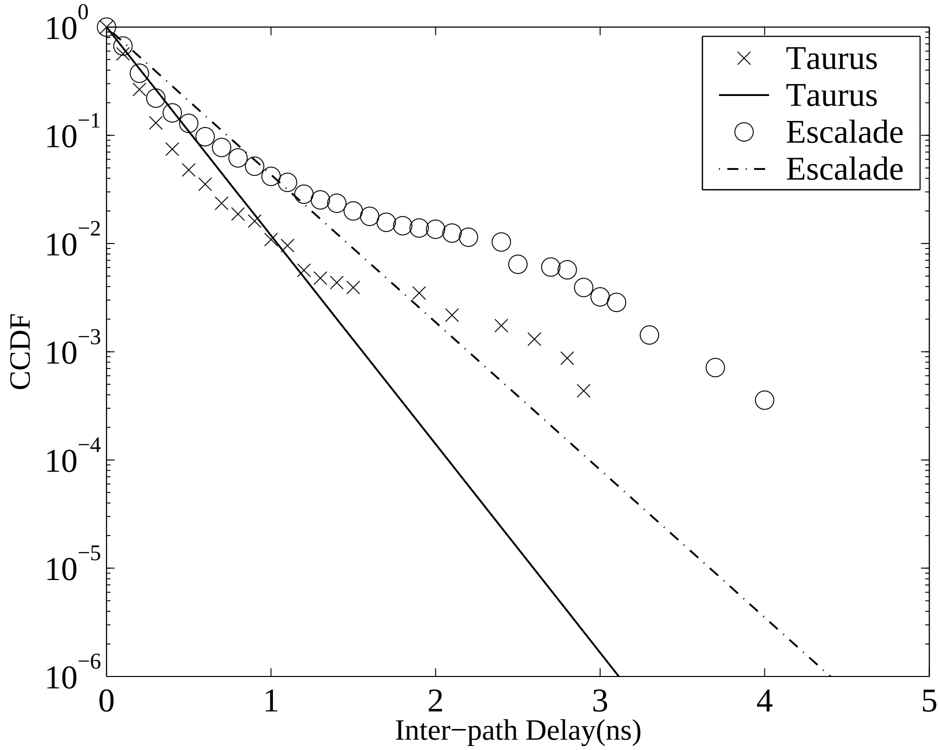

Figure 4.5: CCDF of inter-path arrival intervals and the best-fit exponential distributions for measurements inside the engine compartments.

Before the empirical CDF of the path or cluster amplitudes is calculated, each CIR is normalized by setting the amplitude of the peak path to be one, then the amplitudes of the other paths in this CIR are expressed in values relative to it. In addition, the peak amplitude within a cluster is identified as the amplitude of the cluster. The Rayleigh distribution and Lognormal distribution best-fitting the empirical CDFs of these amplitudes in the meaning of maximum likelihood estimation are found. The probability density function for Rayleigh distribution is

$$f(x;\sigma) = \frac{x\exp(-x^2/2\sigma^2)}{\sigma^2}, \qquad x \in [0,\infty), \tag{4.3}$$

where σ is the standard deviation. For Lognormal distribution, the probability density function is given by

$$f(x;\mu,\sigma) = \frac{\exp[-(ln(x)-\mu)^2/2\sigma^2]}{x\sigma\sqrt{2\pi}}, \qquad x \in [0,\infty), \tag{4.4}$$

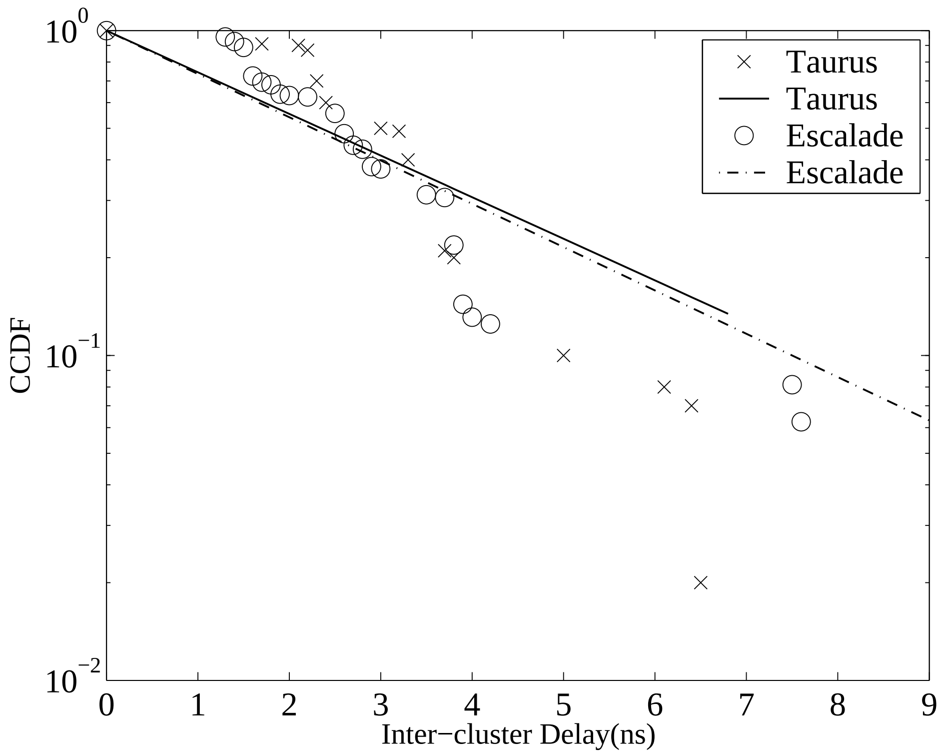

Figure 4.6: CCDF of inter-cluster arrival intervals and the best-fit exponential distributions for measurements inside the engine compartments.

where μ is the expected value and σ is the standard deviation respectively. For our measurements from beneath the chassis and inside the engine compartments, standard deviations of the best-fit Rayleigh and Lognormal distributions are found and listed in Table 4.2. In the mean time, CDFs of the amplitudes for these measurements are plotted in Fig. 4.7 - Fig. 4.12, with their best-fit Rayleigh and Lognormal distributions overlaid. In each figure, it can be easily observed that the best-fit Lognormal distribution curve is closer to the distribution curve of the measured data than that of the best-fit Rayleigh distribution. Calculation of the root mean square errors (RMSEs) for the best-fit Rayleigh and the best-fit Lognormal distribution shows that the latter is a better fit in all cases.

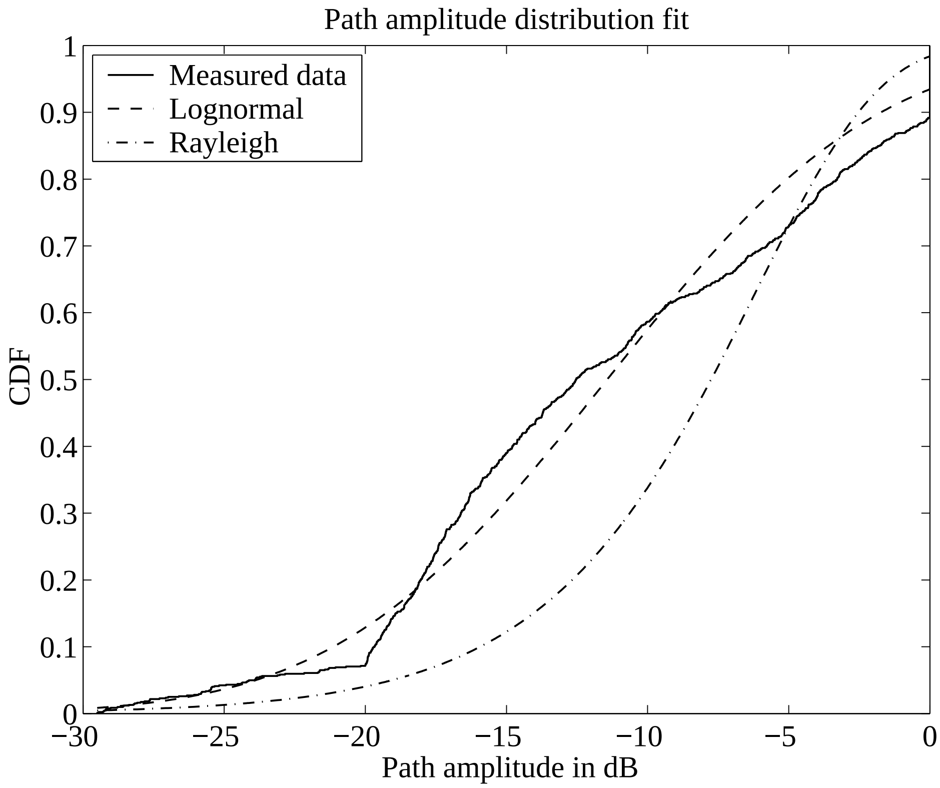

Figure 4.7: Path amplitudes CDF with the best-fit Rayleigh (RMSE=1.1789) distribution and Lognormal (RMSE=0.0489) distribution for measurements beneath the Taurus chassis.

4.1.4 Path and Cluster Power Decay

On one hand, to calculate the PDP model parameters χ, γ and γ_{rise} defined in equation (3.4) for the measured data from beneath the chassis, the deconvolved CIRs are normalized and shifted such that the integrated energy of each CIR equals one and the first path arrives at time zero. The average normalized path powers versus their relative delays are plotted in Fig. 4.13 for the Taurus and in Fig. 4.16 for the Escalade. Values of χ, γ_{rise} and γ introduced in equation (3.4)are found by computing the curve best-fitting these power values in the least squares sense. As illustrated in Fig. 4.13 and Fig. 4.16, such curves give χ, γ and γ_{rise} the values of 0.9452, 0.2117

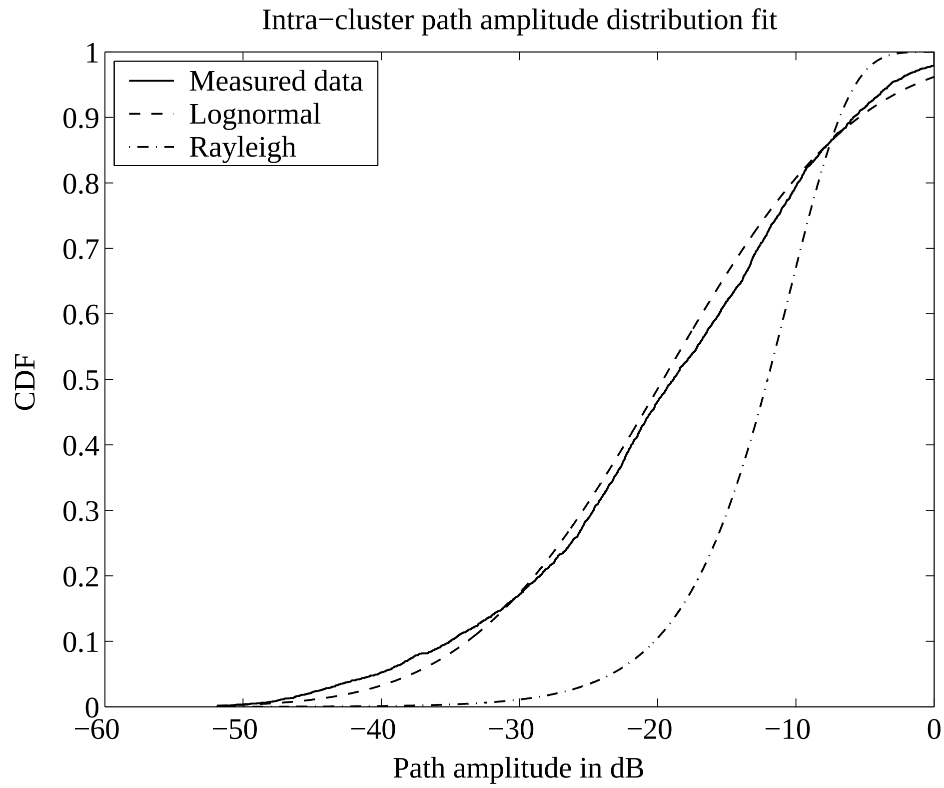

Figure 4.8: Intra-cluster path amplitudes CDF with the best-fit Rayleigh (RMSE=0.2357) and Lognormal (RMSE=0.0239) distributions for measurements inside the Taurus engine compartment.

ns, 0.2524 ns for the Taurus and 0.9240, 0.2141 ns, 0.2997 for the Escalade respectively.

On the other hand, to get the path power decay constant γ for the measured data from the engine compartments, normalization is performed on all clusters in the CIRs so that the first path in each cluster has an amplitude of one and a time delay of zero. Then powers of the paths within these normalized clusters are calculated and superimposed on Fig. 4.14 and Fig. 4.17 for the Taurus and the Escalade. The power decay constant γ is found by computing a linear curve best-fitting these powers in the least squares sense and γ just equals the absolute reciprocal of the curve's slope. In Fig. 4.14 and Fig. 4.17, this curve is shown as the solid line and it gives the intra-cluster path power decay constant γ a value of 1.0840 ns for the Taurus and

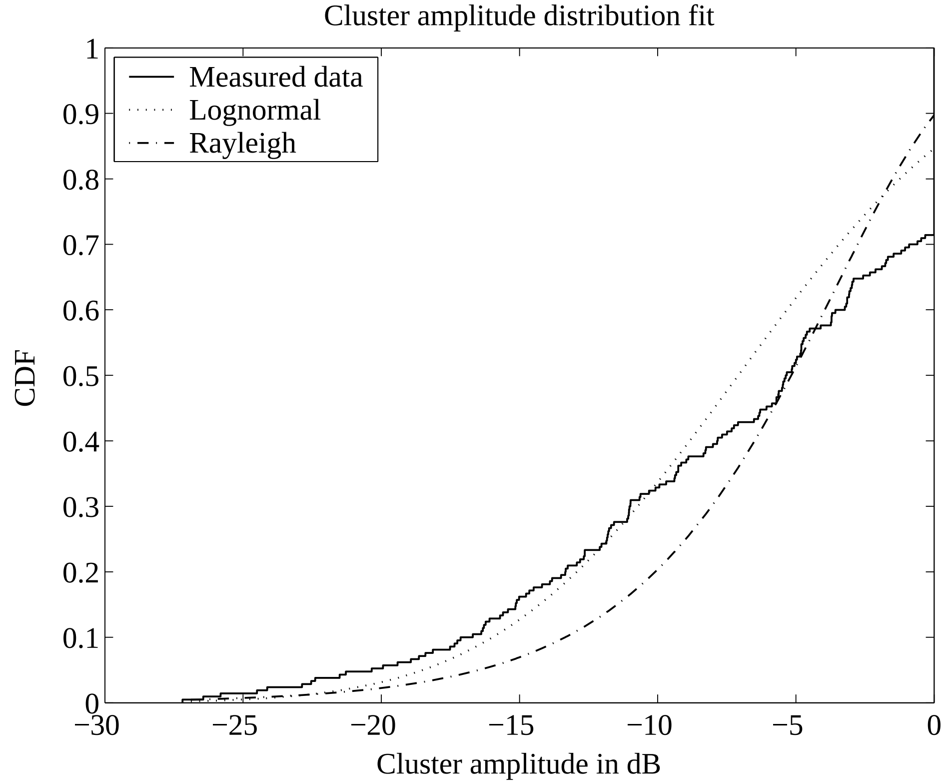

Figure 4.9: Cluster amplitudes CDF with the best-fit Rayleigh (RMSE=0.0840) and Lognormal (RMSE=0.0661) distributions for measurements inside the Taurus engine compartment.

1.9568 ns for the Escalade. Similarly, in order to get the cluster power decay constant Γ, each CIR is normalized in a way so that its first cluster has an amplitude of one and an arrival time of zero. Here cluster amplitude is defined as the peak amplitude within a cluster and cluster delay is defined as the arrival time of the first path within the cluster respectively. Fig. 4.15 shows the superimposition of the cluster powers for the measurements of the Taurus engine compartment and Fig. 4.18 shows that of the Escalade engine compartment. The best-fit curves to these cluster powers which are shown as the solid lines in the figures determine the cluster decay constant Γ to be 3.0978 ns for the Taurus and 3.1128 ns for the Escalade respectively. It is observed that both γ and Γ are smaller than their corresponding values reported in [22] for indoor or outdoor environment, which means faster power decay in the engine compart-

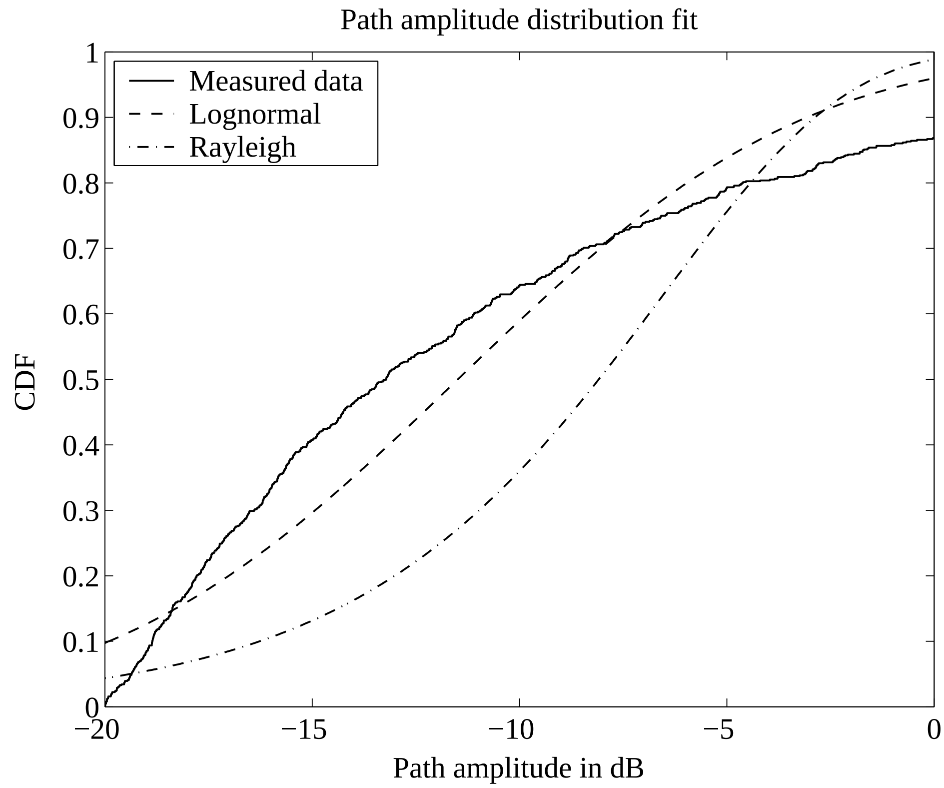

Figure 4.10: Path amplitudes CDF with the best-fit Rayleigh (RMSE=0.2078) distribution and Lognormal (RMSE=0.0726) distribution for measurements beneath the Escalade chassis.

ment. Again, this is caused by the much smaller space in the engine compartment.

4.2 Pathloss Model and Parameters

Path loss describes the ratio of the transmitted signal power to the received signal power. The relation between path loss and the distance is normally described as below [22] [78]

$$PL(d) = PL_0 - 10 \cdot n \cdot log_{10}(\frac{d}{d_0}) + S, \tag{4.5}$$

in which PL_0 is the path loss at the reference distance d_0 of 1m and n is the path loss exponent. d is the distance between the transmitting and the receiving antenna

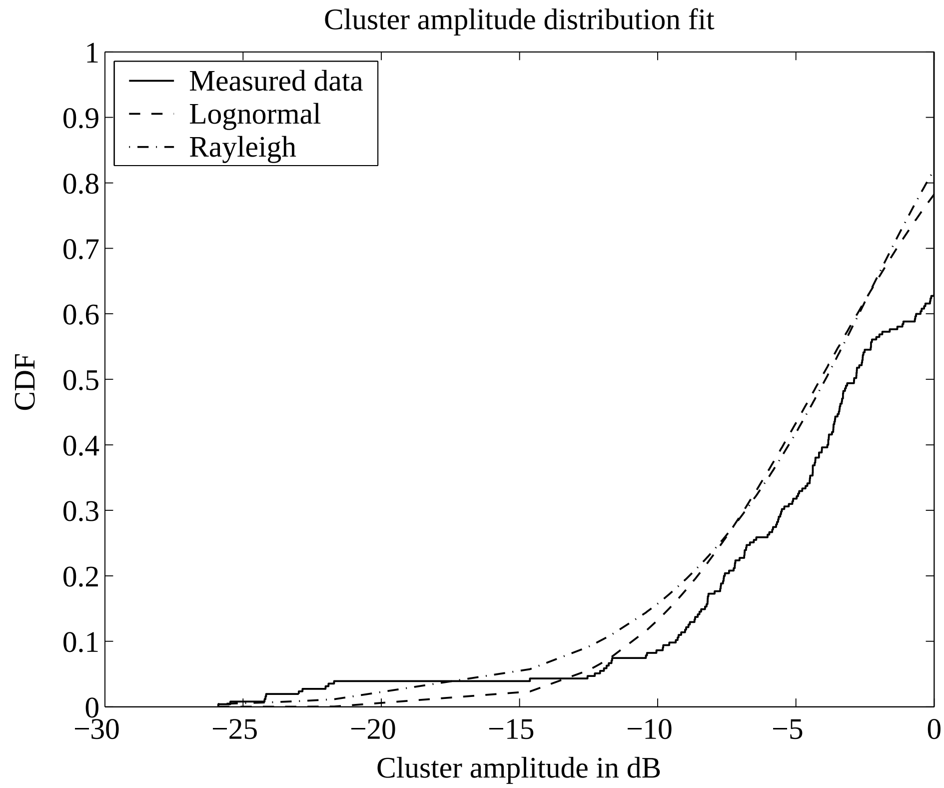

Figure 4.11: Intra-cluster path amplitudes CDF with the best-fit Rayleigh (RMSE=0.2284) and Lognormal (RMSE=0.0319) distributions for measurements inside the Escalade engine compartment.

at each measurement spot. S is a zero mean random variable which has Gaussian distribution with standard deviation σ_S. To evaluate the path loss exponent, the average received energy at each measurement position is calculated directly from the impulse responses. Then the path loss versus $log_{10}(\frac{d}{d_0})$ is plotted in Fig. 4.19 and Fig. 4.20. A least square fit computation is performed in order to get the value of n for the chassis and engine compartment environments. The extracted path loss parameters from the measurement data are listed in table 4.3. Values of these parameters are comparable with those reported for indoor or outdoor UWB measurements [22]. However, it is observed that path loss beneath the Taurus chassis shows big difference from that beneath the Escalade chassis. This is caused by the large path loss values for position RX0 and position RX1 beneath the Escalade chassis. For these

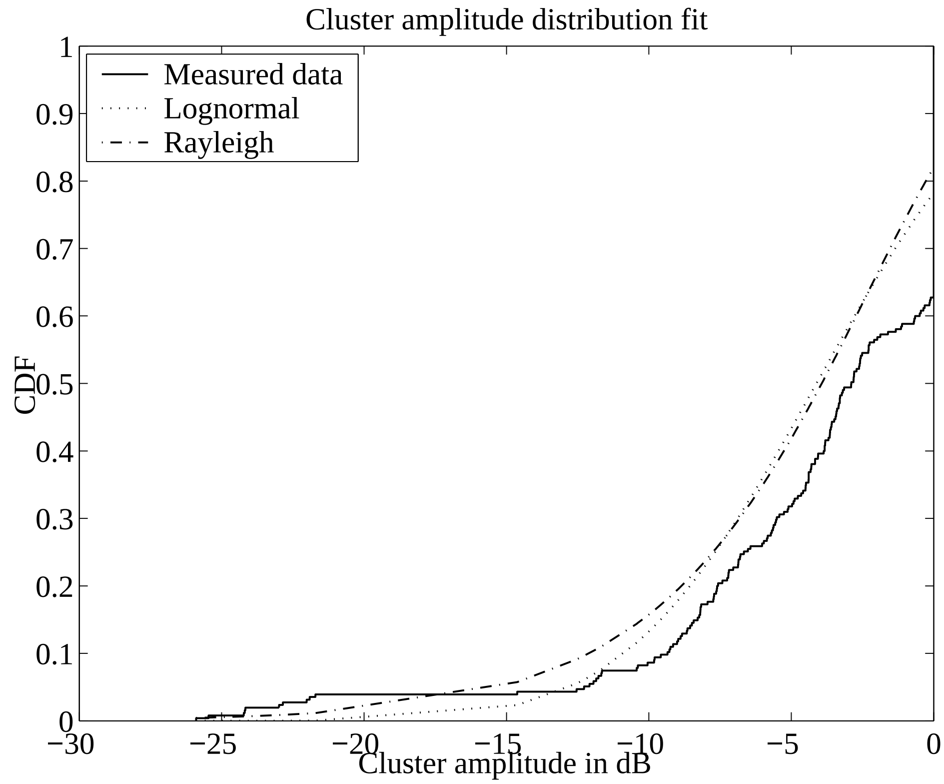

Figure 4.12: Cluster amplitudes CDF with the best-fit Rayleigh (RMSE=0.0891) and Lognormal (RMSE=0.0884) distributions for measurements inside the Escalade engine compartment.

two positions, half the receiving antenna was above the Escalade front wheel axis and half wasn't, when the measurements were being performed. As a result, part of the energy was blocked by the axis and the chassis sitting between the transmitting antenna which was below the chassis plane and the receiving antenna half of which was above the chassis plane. If measurement data from these two positions are excluded when calculating the path loss for the Escalade chassis environment, the extracted PL_0 equals 35.15dB, n equals 4.73 and σ_s equals 1.06.

Equation (4.5) describes the path loss's dependence on distance. For UWB, there is also frequency dependency in the propagation and the path loss is also a function of frequency [64]. The frequency dependency of the UWB path loss is not included in this dissertation and can be a research topic in the future studies.

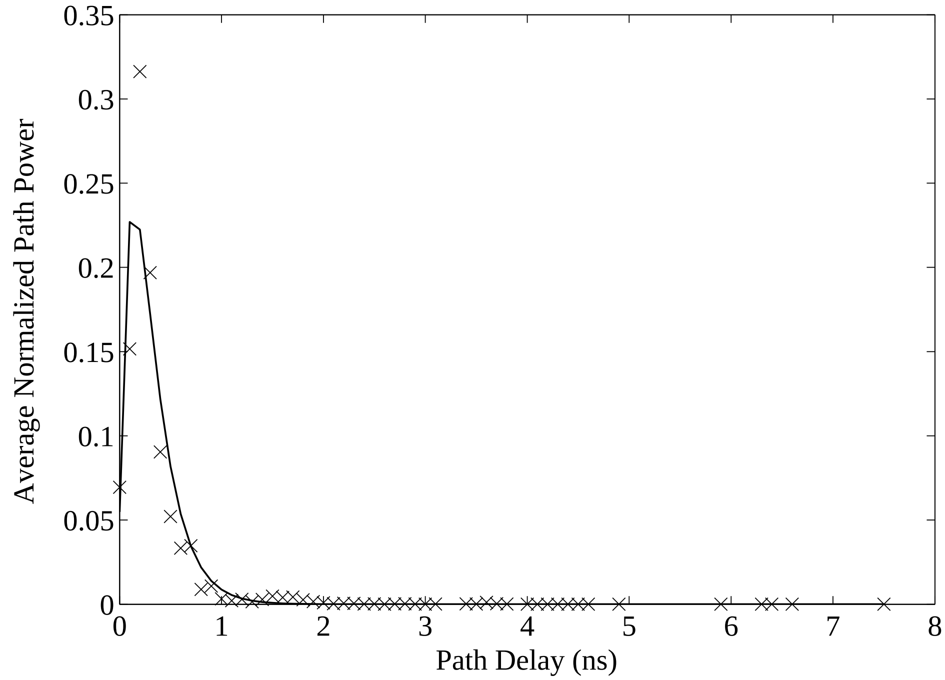

Figure 4.13: Average normalized path power decay for measurements beneath the Taurus chassis.

4.3 Summary

In this chapter, to derive channel model parameters, statistical analysis has been applied to the measurement data from the channels beneath chassis or inside engine compartment of a Taurus and an Escalade. It has been exhibited that in the intra-vehicle environment, the path or cluster arrival rates are greatly larger than those reported for indoor or outdoor environments while the path or cluster power decay constants are smaller. In addition, the RMS delay spreads from the intra-vehicle environments are also less than those reported for the indoor UWB propagation, indicating potential for smaller symbol duration when avoiding inter-symbol interference, hence potential for higher data rate. In addition, this chapter also derives and provides the path loss parameters in the two environments for both vehicles.

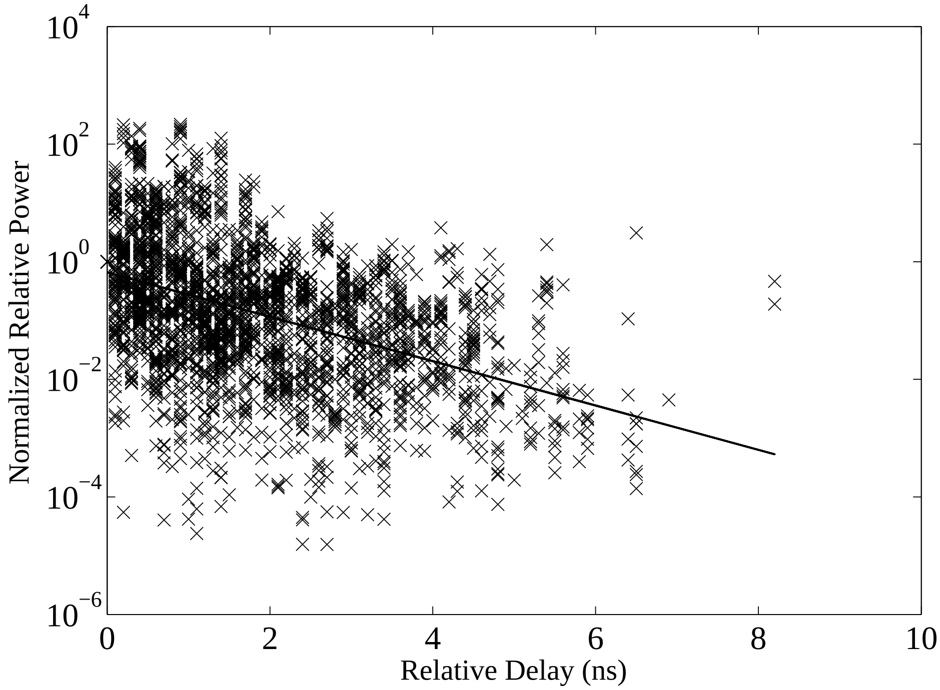

Figure 4.14: Normalized path power decay for measurements from the Taurus engine compartment.

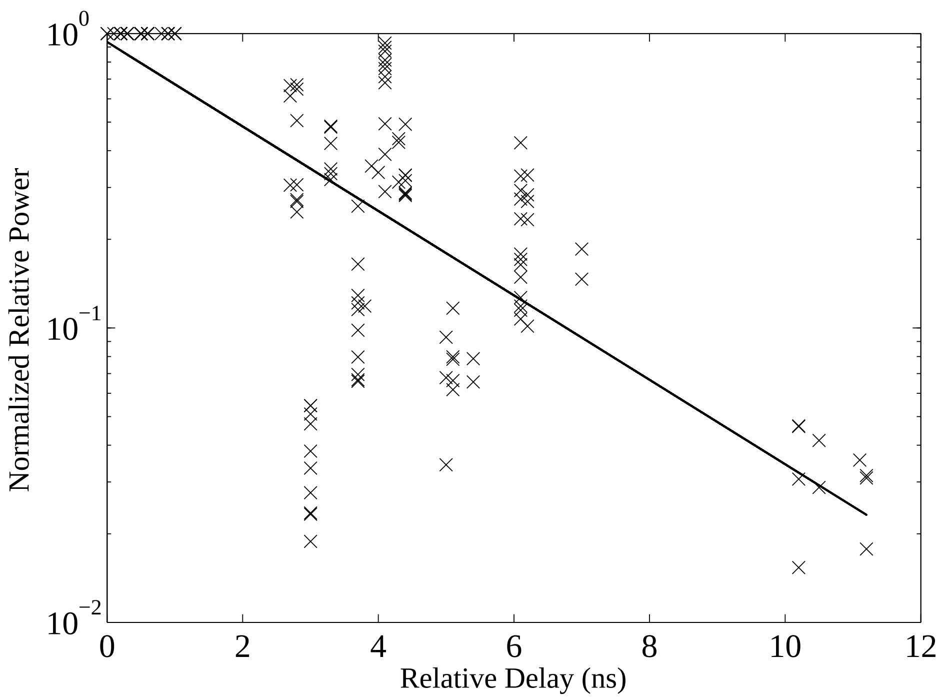

Figure 4.15: Normalized cluster power decay for measurements from the Taurus engine compartment.

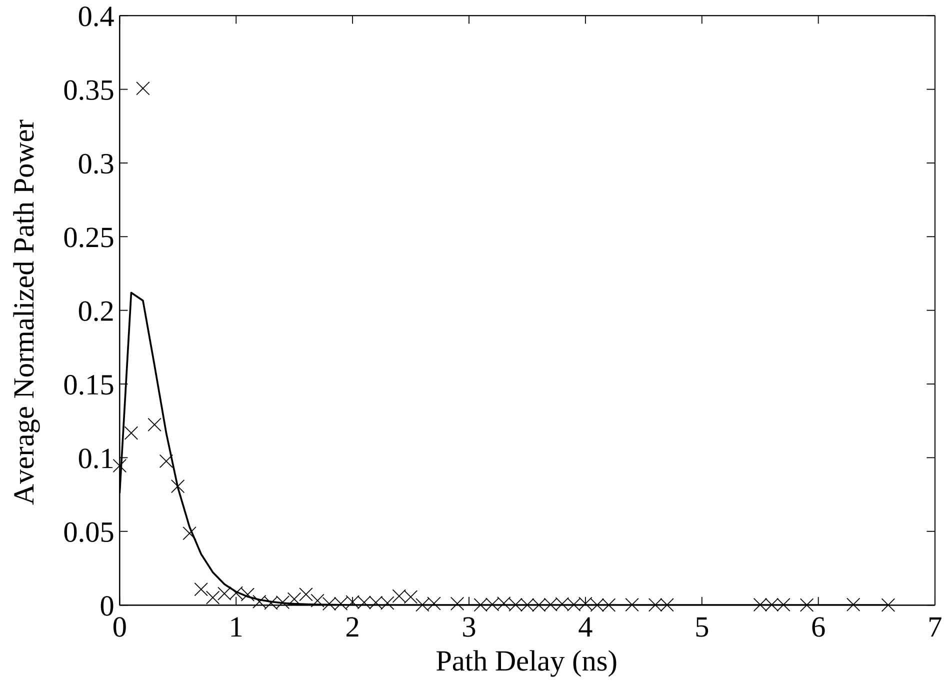

Figure 4.16: Average normalized path power decay for measurements beneath the Escalade chassis.

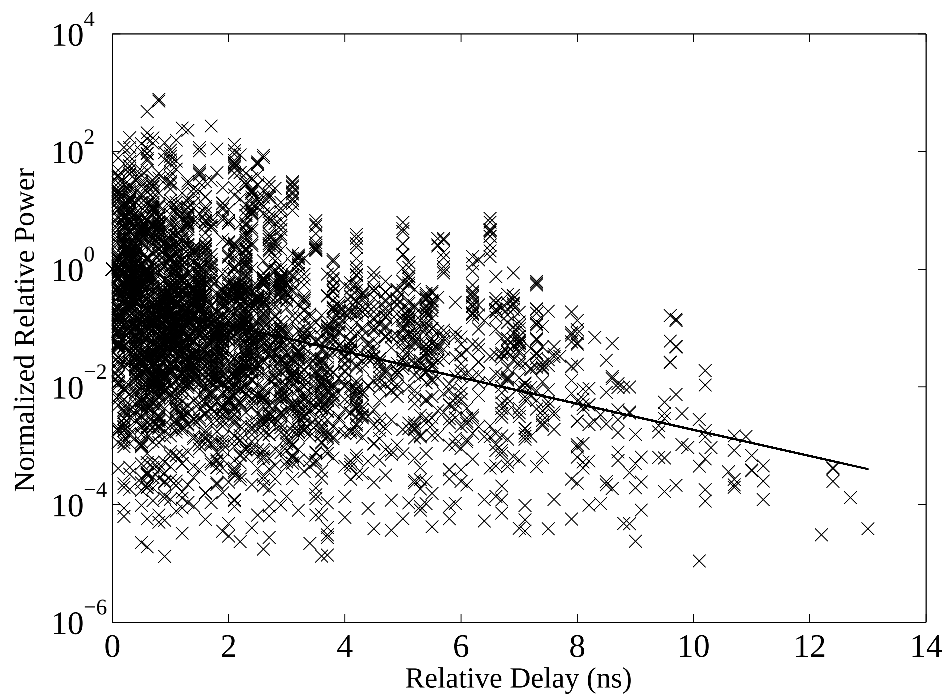

Figure 4.17: Normalized path power decay for measurements from the Escalade engine compartment.

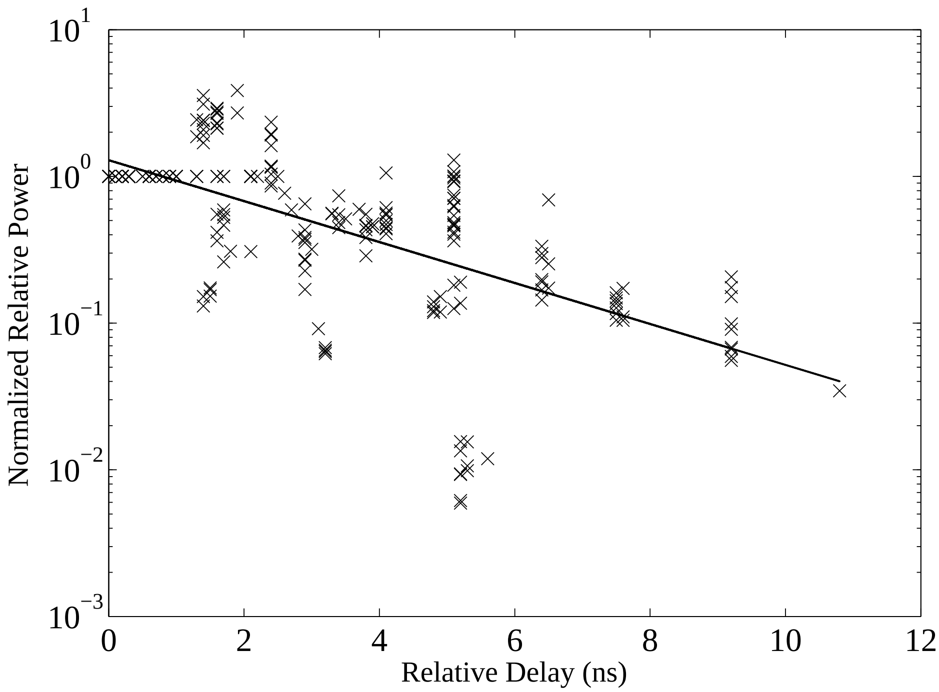

Figure 4.18: Normalized cluster power decay for measurements from the Escalade engine compartment.

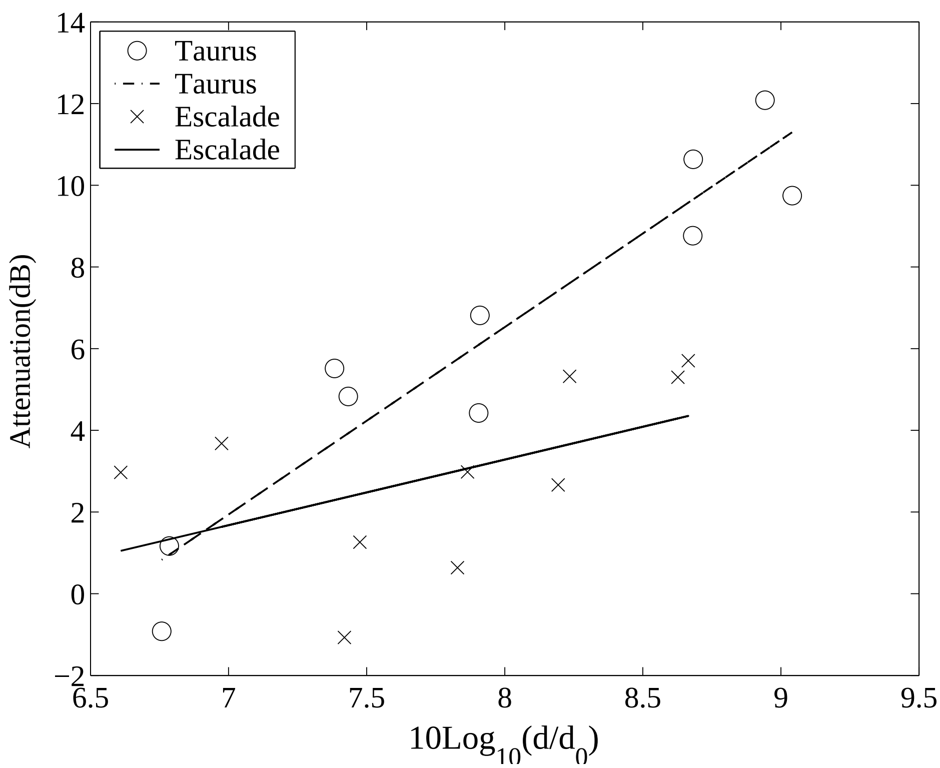

Figure 4.19: Path loss beneath the chassis.

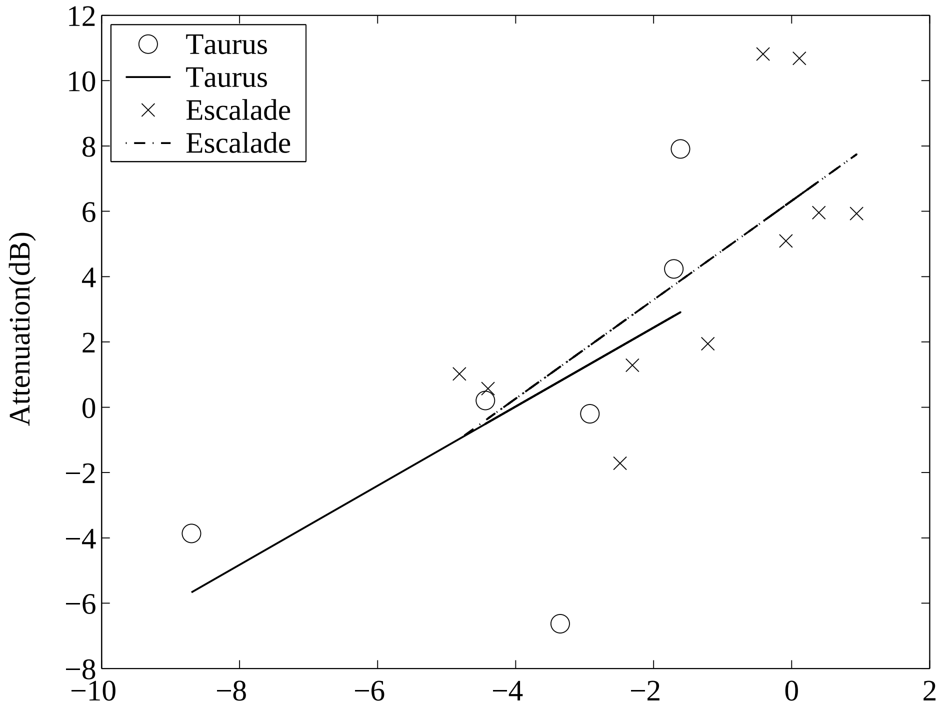

Figure 4.20: Path loss inside the engine compartments.

Table 4.2: Standard deviations of best-fit Rayleigh and Lognormal distributions to the CDFs of path and cluster amplitudes

CDF	Standard deviation σ	
	Rayleigh	Lognormal
Path amplitude (Taurus chassis)	0.3481	7.5688
Path amplitude (Taurus engine compartment)	0.2122	11.0571
Cluster amplitude (Taurus engine compartment)	0.5153	5.1993
Path amplitude (Escalade chassis)	0.3348	6.5672
Path amplitude (Escalade engine compartment)	0.2149	11.3850
Cluster amplitude (Escalade engine compartment)	0.5401	5.2763

Table 4.3: Path loss

	Beneath Chassis		Engine Compartment	
Path loss	Taurus	Escalade	Taurus	Escalade
$PL_0(dB)$	30.15	9.57	4.86	6.32
n	4.58	1.61	1.21	1.51
σ_s	1.34	1.92	4.20	3.00

CHAPTER 5
MOVEMENT INFLUENCES ON INTRA-VEHICLE UWB MULTI-PATH CHANNEL CHARACTERISTICS

5.1 Analysis

As mentioned in Chapter 2, to investigate whether and how car movement influences the UWB channel, the same set of channel measurements have been conducted under the Escalade chassis when it is running and when it is halted. This chapter compares the measuring results of them. Same as that mentioned in Chapter 3, the modified tapped delay line model is used to describe the UWB multi-path propagation in both cases. Channel model parameters extracted from the collected channel data are compared and analyzed.

Two typical multi-path profiles recorded at RX1 in Fig. 2.4 with the absolute amplitudes are shown in Fig. 5.1. The upper profile was collected when the car was stationary and the bottom one was from the moving case. Visual inspection reveals that the lengths of the multi-path profiles are both less than 10 ns. This is also true for all other positions. In addition, the clustering phenomenon does not exist in the measurements from moving vehicle either. It can also be seen that the shape of the profiles looks very similar to each other.

5.1.1 RMS Delay and Number of MPCs

Fig. 5.2 shows the complementary cumulative distribution functions (CCDFs) of the RMS delays for IRs from both the stationary case and the moving case, with the mean value of 0.6233 ns or 0.7491 ns as separately marked by the vertical lines. It can be seen that when the car is moving, the RMS is slightly larger. Furthermore, the average number of multi-path components calculated from all of the IRs is 35 for the

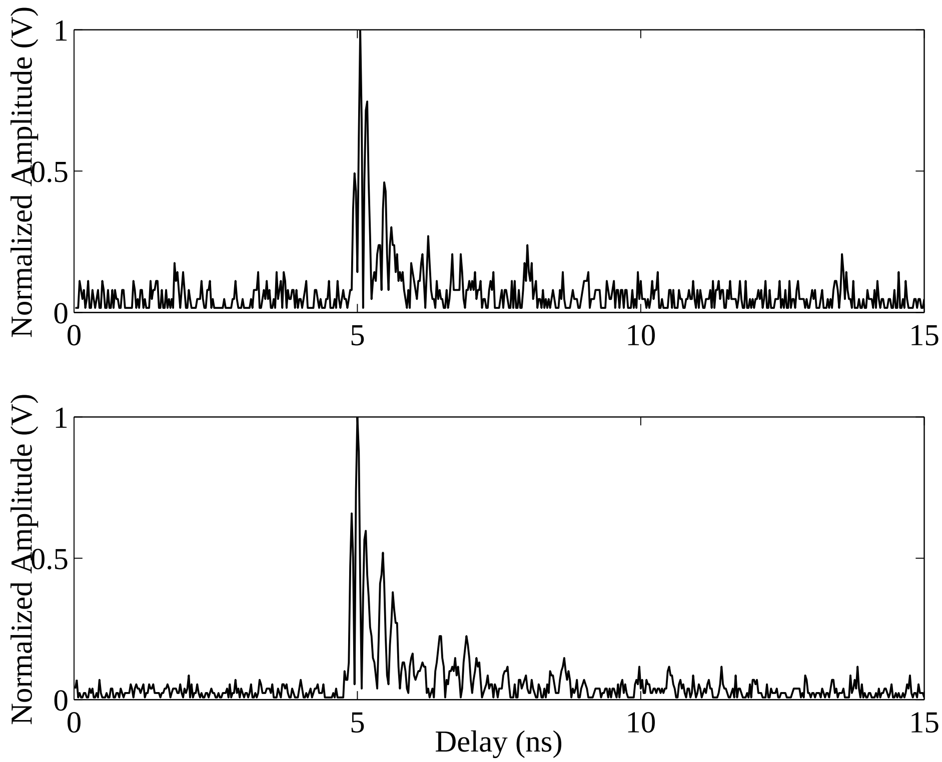

Figure 5.1: Example of Recorded Multi-path Profiles at RX1.

stationary vehicle and again a slightly larger number of 42 in the moving case. When the car was running on road, the part of the ground covered by the chassis was different each time the measurement was conducted. The slight increase in the number of paths may due to such changes of the ground areas covered by the car which constructed a part of the channel environment. In addition, ground areas on road were normally less smooth than that of the parking building where the stationary measurement was taken. Although the larger RMS delay and number of MPCs indicate a slightly lower data rate to avoid inter-symbol interference due to the movement of the vehicle, the magnitude of the influence is tiny.

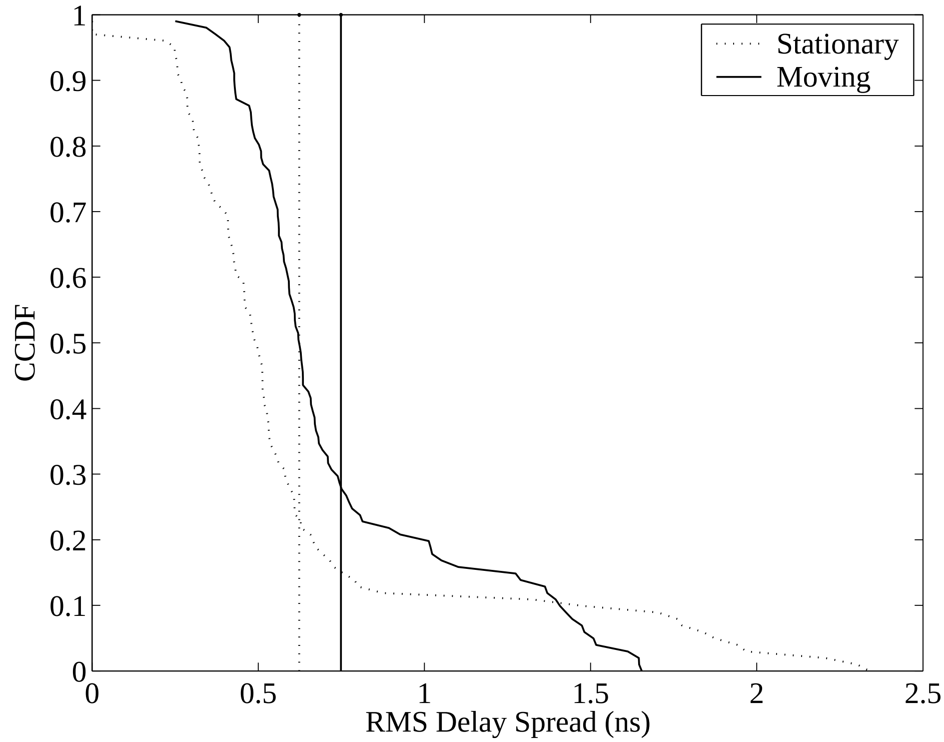

Figure 5.2: RMS Delay CCDF and the Mean Value.

5.1.2 Power Delay Profiles

Observation of the normalized power delay profiles from all IRs reveals that the shape of the PDP always starts with a fast rising edge then decays exponentially from the peak, no matter in moving or stationary case.

The normalized power delay profile averaged over the ten measurement spots from the stationary vehicle is displayed in Fig. 5.3 and its counterpart from the moving vehicle is shown in Fig. 5.4. It can be seen that the average PDP from the moving vehicle has a slightly steeper rising edge and a slightly steeper decaying edge, resulting from a stronger peak path. However, in both cases most power arrives within 2 ns from the first path and the basic shapes of the two average PDPs are similar to each other.

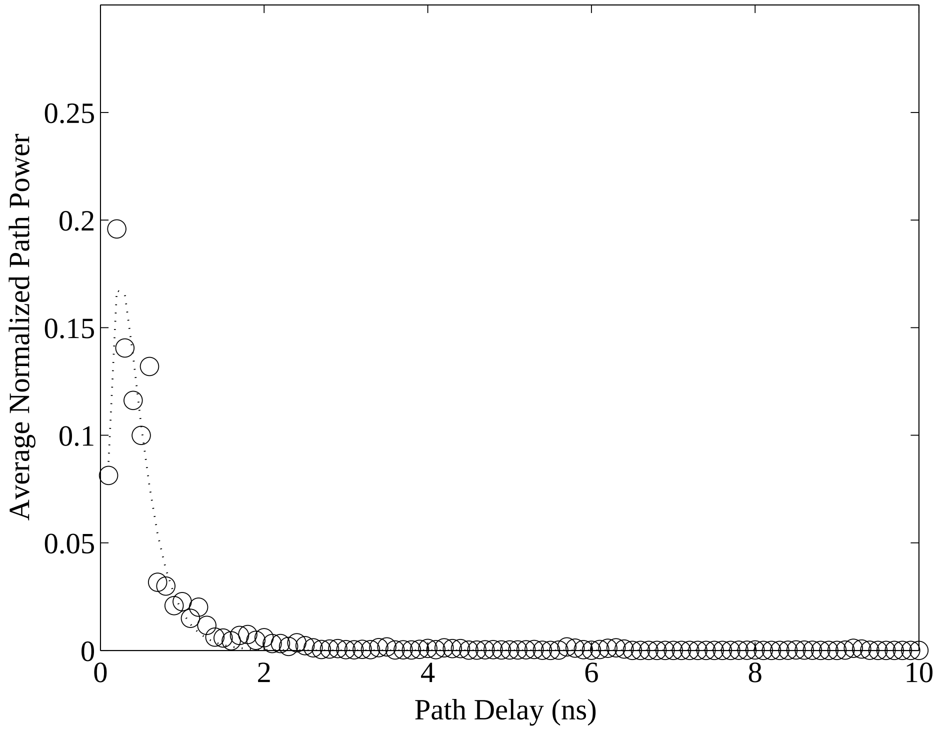

Figure 5.3: Stationary Vehicle: Average Normalized PDP. (χ=0.9108, γ_{rise}=0.4957 ns, γ=0.2311 ns)

5.1.3 Path Arrival

In both the moving vehicle and the stationary vehicle cases, path arrival is modeled as a Poisson process with a fix rate.

Fig. 5.5 shows the CCDFs of the inter-path arrival intervals from the impulse responses of the stationary vehicle and the moving vehicle. It's obvious that the two CCDFs almost coincide with each other when the delay is smaller than 2 ns. In order to quantitatively evaluate the difference, their respective best-fit exponential distribution curves in the maximum likelihood sense are found and superimposed in the figure. In the stationary vehicle case, the average inter-path interval, which is the reciprocal of the arrival rate λ, equals 0.2228 ns. In comparison, it is 0.2212 ns when the vehicle is moving. Furthermore, for both of them, the arrival intervals larger than 1.5 ns represent less than 1% of all values and they always happen at the tailing parts

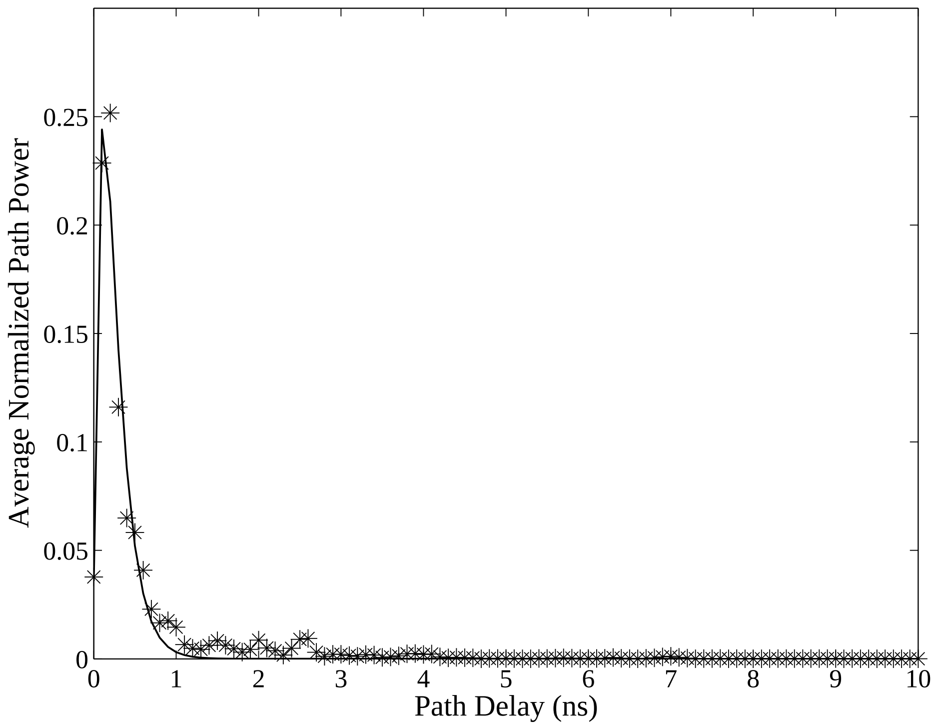

Figure 5.4: Moving Vehicle: Average Normalized PDP. (χ=0.9640, γ_{rise}=0.1874 ns, γ=0.1733 ns)

of the IRs. In general, the average inter-path arrival intervals in the two cases almost equal to each other and the movement of the car produces little effect on the path arrival rate.

5.1.4 Path Amplitude Distributions

To investigate whether the vehicle movement have influences on the statistical distribution of the path amplitudes within the impulse responses of the UWB channel in the intra-vehicle environment, the empirical CDF of the path amplitudes from all normalized IRs of the stationary vehicle are calculated. The same calculation is also performed for the moving vehicle and the two resulting CDFs are overlaid in Fig. 5.6. It can be seen that the two empirical CDF curves nearly overlap with each other,

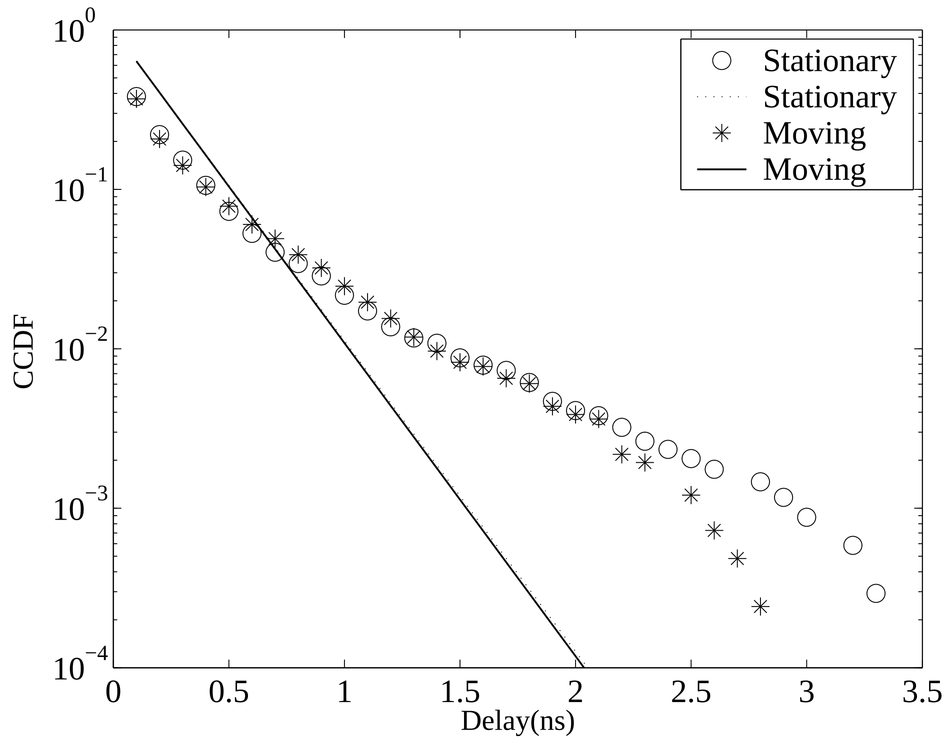

Figure 5.5: CCDFs of Inter-path Arrival Intervals and the Best-fit Exponential Distribution Curves.

indicating that the movement of the vehicle causes very little changes to the distribution of the path amplitudes.

Fig. 5.7 overlays the best-fit Rayleigh and Lognormal distributions with the cumulative CDF of the path amplitudes for stationary vehicle and Fig. 5.8 is for the vehicle in movement. It can be seen that in each case, Lognormal distribution is almost a perfect fit for the path amplitude distribution. In addition, the movement of the vehicle only causes slight changes in the Lognormal distribution parameter values as illustrated by Fig. 5.8 and Fig. 5.7.

5.2 Conclusion

In this chapter, the statistical model parameters of the stochastic tapped-delay-line multi-path model have been derived from the measured data beneath the

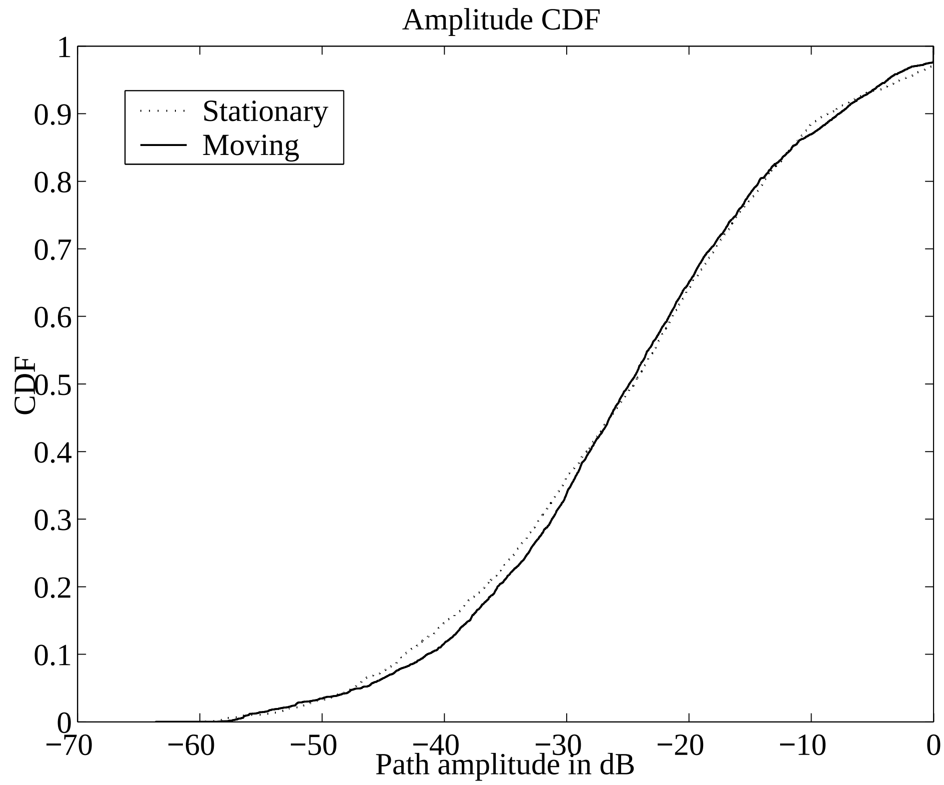

Figure 5.6: Comparison of Empirical CDFs for Path Amplitudes from Stationary and Moving Vehicle.

chassis of the Escalade in both stationary and moving status. Values of these parameters are summarized in Table 5.1 below. Comparison of the parameter values shows that the movement of the vehicle leads to slight increase in RMS delay and the number of MPCs as well as very slight changes in the average power delay profile, in the path arrival and the path amplitude distribution. In conclusion, movement of the vehicle causes very little influence on the UWB propagation beneath the chassis and will not bring any special requirement to the system design.

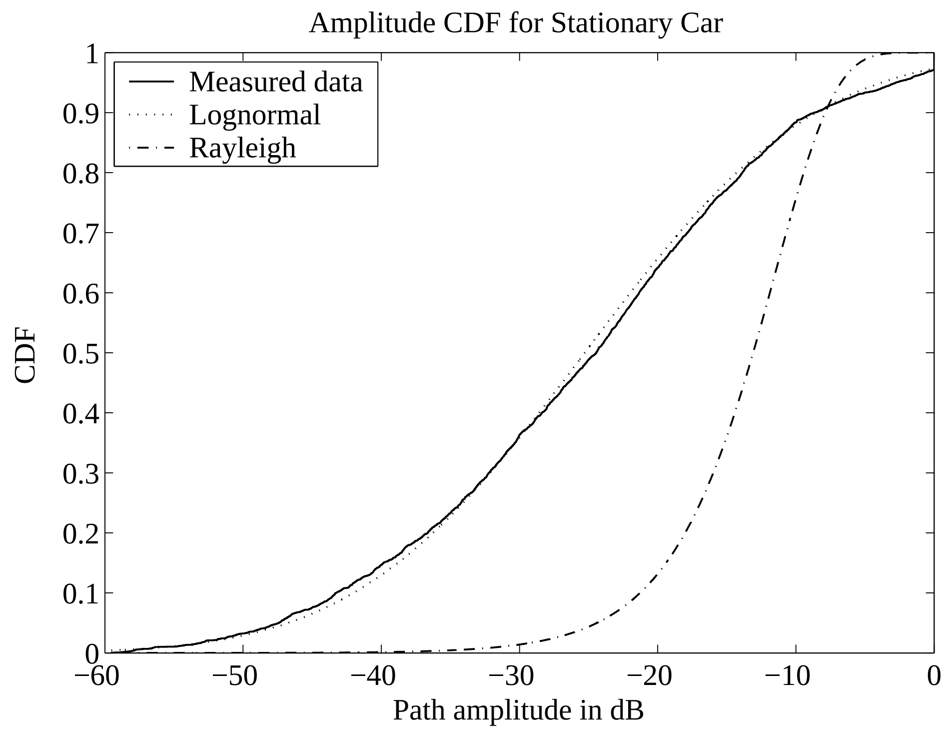

Figure 5.7: Best-fit Lognormal and Rayleigh for Stationary Vehicle Path Amplitudes CDF (Rayleigh: σ=0.1881, Lognormal: σ=13.0571 and μ=-25.2768).

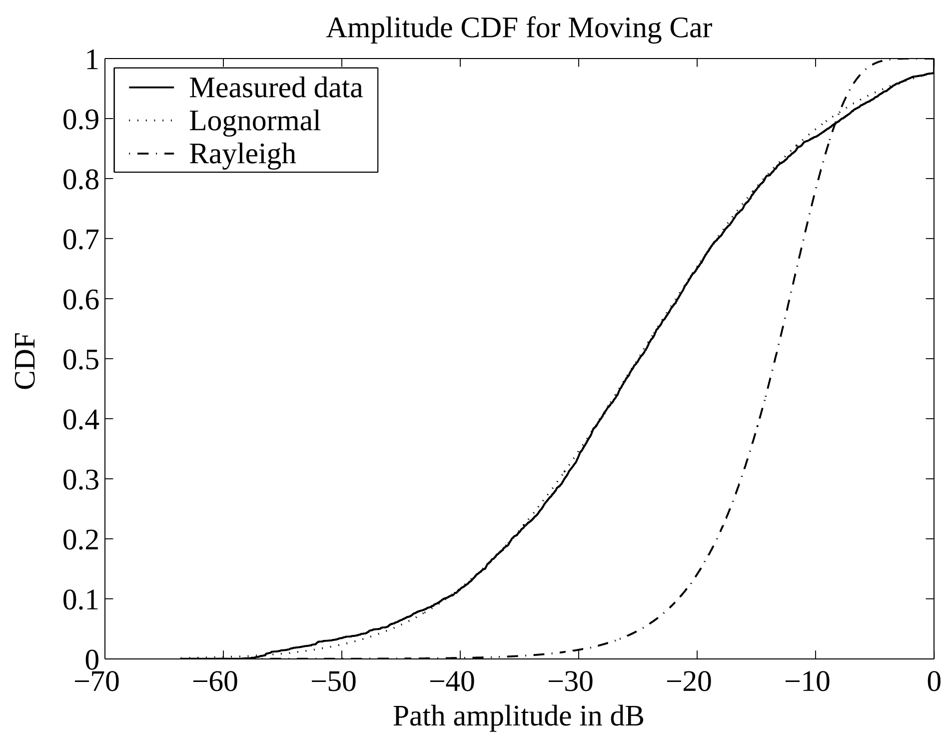

Figure 5.8: Best-fit Lognormal and Rayleigh for Path Amplitudes CDF from Moving Vehicle (Rayleigh: σ=0.1813, Lognormal: σ=12.6417 and μ=-24.9959).

Table 5.1: Channel parameters beneath the chassis of stationary and moving Escalade

	Stationary	Moving
Mean RMS delay	0.6233ns	0.7491ns
Average MPC number	35	42
χ	0.9108	0.9640
γ_{rise}	0.4957ns	0.1874ns
γ	0.2311ns	0.1733ns
$1/\lambda$	0.2228ns	0.2212ns
Best-fit Rayleigh σ	0.1881	0.1813
Best-fit Lognormal σ	13.0571	12.6417
Best-fit Lognormal μ	25.2768	24.9959

CHAPTER 6
AUTOMATIC CLUSTER IDENTIFICATION

6.1 Introduction

As mentioned in the previous chapters, overlapping and fading exist in UWB propagation due to multiple paths or transceiver motions, and the S-V model is widely referenced in the UWB literature to characterize channel impulse responses [57]. One of the main characteristics described by the model is that paths arrive in clusters, which is a phenomenon also existing in the UWB propagation inside the engine compartment [57] [79] [80] [81]. A cluster is defined as a group of multi-path components with similar arrival times and exponentially decaying amplitudes. The first step to derive the S-V model parameters which characterize the UWB propagation is to identify these clusters from the UWB impulse responses. As stated in some papers, in the UWB literature, the identification of clusters are conventionally performed manually via visual inspection [82] [83], which is also the method used in Chapter 4 of this dissertation for the channel measurement data inside the vehicle engine compartment. Although this method can be easily performed on relatively small sets of measurement data, several problems have been found when processing large amount of impulse responses like those in Chapter 4. First, manual cluster identification is very difficult and time consuming when the number of impulse responses grows up to hundreds or even thousands. Moreover, different persons inspecting the same data may create different cluster identification results, which will lead to differences in the channel model parameters. Furthermore, it is highly possible that the clusters identified manually by the same person at different time for a same impulse response will be different. As an alternative method, an automatic cluster identification algorithm is needed to fix the above problems.

A few studies on automatic cluster identification have been made in the literature [82] [83] [84]. The automatic clustering algorithm discussed in [82] involves the setting up of various criteria for the definition of a cluster. Because the criteria proposed in [82] are quantitative, the algorithm must take lots of user input to initialize the program, which makes the procedure semi-automatic. Normally, in the UWB channel measurement campaign, hundreds or thousands of impulse responses for statistical analysis have to be processed and the semi-automatic algorithm is still not convenient enough to process such a huge number of channel data. This motivates us to develop more automatic procedures for cluster identification. The focus of this chapter is an algorithm that can find clusters automatically in channel impulse responses. This algorithm deals with filtering the clusters, setting the threshold and finding the accurate clusters. Our experiments deal with UWB impulse responses with clustering phenomenon, like those inside the vehicle engine compartment, so as to speed up the cluster identification process and to assure the stability of the results.

This chapter is organized as follows. In Section 6.2 the cluster identification problem is defined and the issues that the automatice cluster identification algorithm needs to resolve are listed. In Section 6.3, the automatic cluster identification algorithm is explained in detail. In Section 6.4 we demonstrate the algorithm by giving example results when it is applied to realistic UWB impulse responses inside the engine compartment and Section 6.5 concludes this chapter.

6.2 Problem Definition

The initial point is that we have a large set of impulse responses obtained from intra-vehicle UWB channel measurements and it is observed that paths tend to arrive in clusters. In order to estimate the S-V model parameters to characterize the intra-vehicle UWB channel, we must find a way to identify the clusters with acceptable accuracy. It is always possible that clusters are identified manually with visual inspection. However, it is very impractical to identify clusters manually for a very large amount of data because the workload can become frustrating and overwhelming. This is the key motivation for us to find an automatic way to identify the clusters.

Multi-path propagation is the fact that paths arrive at the receiver with different time delays. It leads to the overlapping of neighboring clusters in the impulse responses. This situation creates a problem for identifying a correct cluster because it is difficult to identify where the clusters begin or end. In addition, there is also some noise, or the unwanted paths, in the impulse responses and this can form fake clusters. This adds further difficulty to recognize the real clusters. We have to find a way to remove these fake clusters.

As stated in previous chapters, our measurement experiments were performed in time domain. When inspecting the impulse responses derived from the measurement data, it was found that the strongest paths or the peaks do not always arrive at the starting point of the power delay profiles of the impulse responses. This phenomenon may also exist within the clusters of the impulse responses, which means that the first path of a cluster is not always the strongest one. Therefore, instead of having a sharp beginning, each cluster may own a rising edge [73] [74]. This observation makes it difficult to recognize the starting point of such kind of clusters. We have to find a way to identify those clusters without a steep onset.

6.3 Cluster Identification Algorithm

The proposed cluster identification algorithm takes both the time distance and the variations in amplitude into account when recognizing clusters. In the previously reported efforts, the algorithms required many user inputs and made the results more subjective [82]. The algorithm proposed in this chapter requires much less inputs from the user. Before any raw measurement data is input to the algorithm, the received multi-path signal waveforms are first deconvolved using CLEAN algorithm to extract the impulse responses. CLEAN algorithm assumes that the received signal is a sum of the same shape pulses arriving at different time and with different strengths. Details of the CLEAN algorithm can be found in Chapter 3. Our algorithm has two main steps. The first step is to find clusters using time distance. Then each cluster found in the first step is further broken down into smaller clusters using the variations in the amplitudes.

6.3.1 Cluster Identification Using Time Delays

The first step in our algorithm is to find the peak paths in the channel data. A peak path is defined as a path which is stronger than its immediate neighboring paths. Assuming that P_i is used to represent the peak paths, where i is the index of the peak path and P_i is the path magnitude. Then P_i is divided into clusters according to the amount of time difference between P_i and P_{i+1}. The time difference between P_i and P_{i+1} is found for all the values of i and they form a time interval set D_i. The algorithm will require the user to input a threshold T which is the minimum amount of time interval between any neighboring clusters. After this, each D_i will be compared with the input parameter T. If a D_i is larger than T, i will mark the beginning of a new cluster. On the contrary, if it is less than T, no action will be taken and the next D_i will be processed. Because as time progresses the impulse responses tend to become more separated, the algorithm is possible to detect that a path is the only one in its cluster and the path amplitude is very small. In such case, the algorithm will combine the path into the previous cluster.

6.3.2 Cluster Identification Using Amplitudes

The second step in our algorithm is to further identify using amplitude changes new clusters inside those recognized by the first step. S-V model states that the beginning of a new cluster should have a large sudden increase in path amplitude compared to the tail of the last cluster [57]. This property is used to further identify the clusters unidentified in the first step. A line best fitting the data points and the error associated with the line can help determine where a large increase in path amplitude occurs, and consequently help recognize the beginning of a cluster. Such a line of best fit is found using the least squares method. This method finds a line for which the sum of the squares of error is minimized. It works because if the error is small, all data points should be close to the line and no one largely deviates from it. Therefore, a large deviation will represent the beginning of a new cluster. With the line of best fit defined above, the goal of this step is to find groups of best-fit lines to cover all data points P_i in an impulse response. The beginnings of lines signify the starting points of clusters.

Procedure flowchart in this second step of our algorithm is shown in Fig. 6.1. The input to this procedure is the output from the first step, that is, the impulse response with identified clusters by the time delay criteria. Assuming that the peak paths are still represented by P_i. In addition, the user is also prompted to manually input an error threshold T. The value of T has to be chosen based on how large the deviations of P_i to the line of best fit should be. If T is too big, paths whose peaks largely deviate from the line will not be identified. But if T is too small, beginnings of clusters will not be identified correctly and too many fake clusters will be recognized mistakenly.

In this procedure, the lines of best fit are found in the least squares sense. It is to minimize the sum of the squared distances x_i of data points P_i from the line of best fit. To complete this, assuming that the residual for a data point is defined as vertical distance of the point to a line of best fit. The error of the line is defined as the norm of all residuals, which is the root mean square of all distances as shown in equation (6.1) below.

$$norm \quad of \quad the \quad residuals = \sqrt{x_1^2 + x_2^2 + x_3^2 + \cdots} \quad . \tag{6.1}$$

The algorithm will find a set of neighboring data points whose line of best fit has the minimum error. These data points will be recognized as a cluster and this cluster identification procedure will iterate until every P_i has been placed into a cluster.

After this procedure completes, the resulting lines of best fit will be checked to see if any line has a positive slope. According to S-V channel model, the power of signals within a cluster must always be decreasing in general. This means that if a line of best fit correctly identifies a cluster, it must have a negative slope. Otherwise, the identification result is incorrect hence a fake cluster. This incorrectly identified cluster is usually the rising edge of a cluster in which the strongest path is not at the beginning. To correct the results, each of those clusters whose best-fit lines have positive slopes is combined with the cluster just after it. One thing to mention here is that this step is not shown in the flowchart in Fig. 6.1.

6.4 Examples

To see how the proposed algorithm works, we tested it on the intra-vehicle UWB channel measurement data. This algorithm was able to correctly identify the number of clusters, where the clusters began and where the cluster ended in our channel data. This section will show some examples of applying the algorithm on the UWB impulse responses in the vehicle engine compartment environment.

Fig. 6.2 shows one example of UWB channel impulse response extracted by the CLEAN algorithm. It will be the input to the cluster identification algorithm. It was assumed that D_i represented the amount of time delay between paths P_i and P_{i+1}. This impulse response was split into clusters by the first step of the algorithm according to the time delays D_i and the user input threshold T. The threshold that was used was $T = 1.6ns$ and the resulting clusters are shown in Fig. 6.3 in which the dash dotted lines mark the clusters.

Each cluster shown in Fig. 6.3 is further divided into new clusters by the second step of the algorithm based on path amplitude. In this step, the user input error threshold T that was used was 0.1. The first cluster, which was identified as 1.3 ns to 4.6 ns in the first step by time delays, was further divided into two sub-clusters, one was from 1.3 ns to 2.6 ns and another was from 3.0 ns to 4.6 ns. All the remaining clusters identified in the first step remained unchanged and no new sub-clusters were found for them. Fig. 6.4 shows the resulting three lines of best fit for the cluster from 1.3 ns to 4.6 ns. It is noticed that the second line has a positive slope. As a result, it should not correspond to a new sub-cluster and this incorrectly identified sub-cluster was consolidated with the sub-cluster following it. Combining the results from the two steps, the final clusters identified with respect to both path time intervals and amplitudes are shown in Fig. 6.5.

In addition, the accuracy of this proposed algorithm was compared to the one described in [82]. It was found that in those impulse responses where there were large time delays between clusters, both algorithms would be able to identify clusters correctly. However, when the time delays between clusters were not very large, the algorithm proposed in this chapter was able to identify the start of clusters more accurately. As an example, the identified clusters for a same impulse response are shown in Fig. 6.6 and Fig. 6.7. The reason that our algorithm identifies the beginnings of clusters more accurately is because the amplitude of the first path within a cluster may not be the largest. Hence there may be a large time delay between the starting point and the peak path of a cluster. Furthermore, the amplitude of the starting path of a cluster could be very small too.

6.5 Conclusion

Our intra-vehicle UWB channel measurement campaign produced a large amount of channel data. Before channel model parameters can be extracted, we need to identify possible clusters in these impulse responses. It is time-consuming to handle such a large number of channel impulse responses manually and the resulting clusters may not be consistent when identified by different persons or at different time. Therefore we designed an algorithm that would identify these clusters automatically. When implementing this algorithm we make sure that it identifies the clusters accurately, as would be if the clusters were identified manually via visual inspection. This algorithm was able to take both the inter-path time intervals and path amplitudes into consideration when identifying clusters. Results of implementing this algorithm on our measured channel data verify that it works accurately.

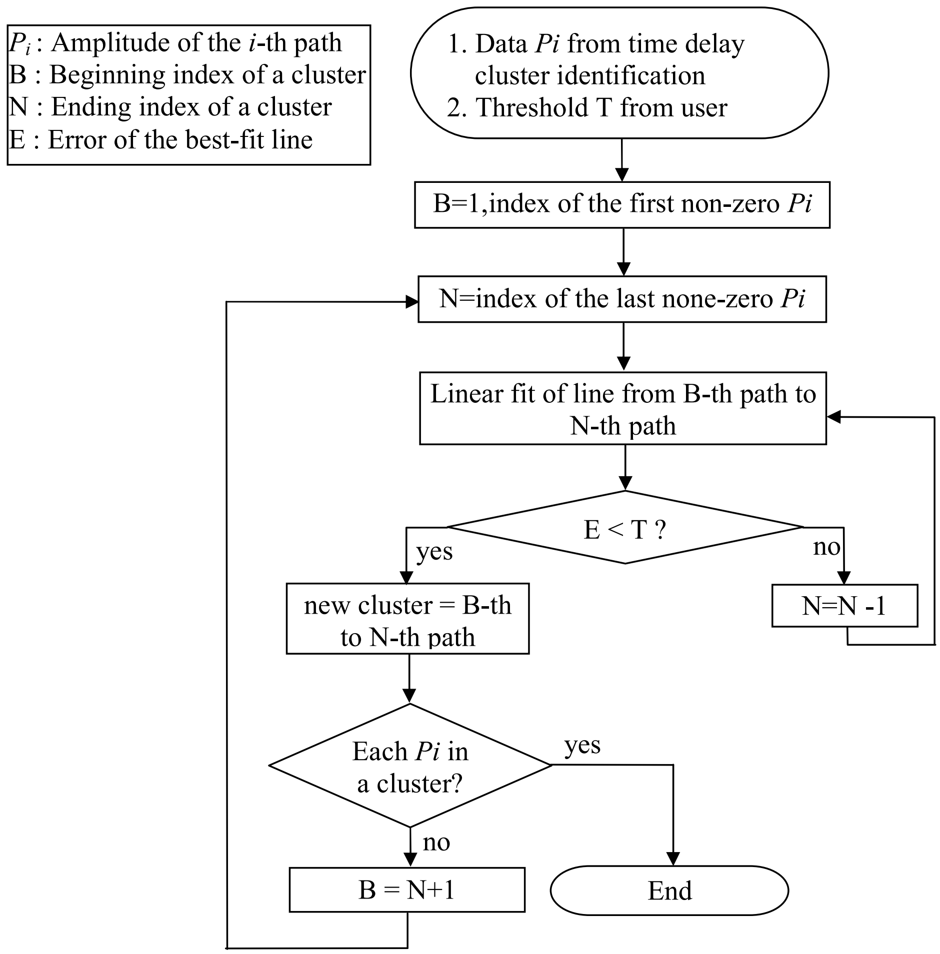

Figure 6.1: Flowchart of cluster identification using amplitude.

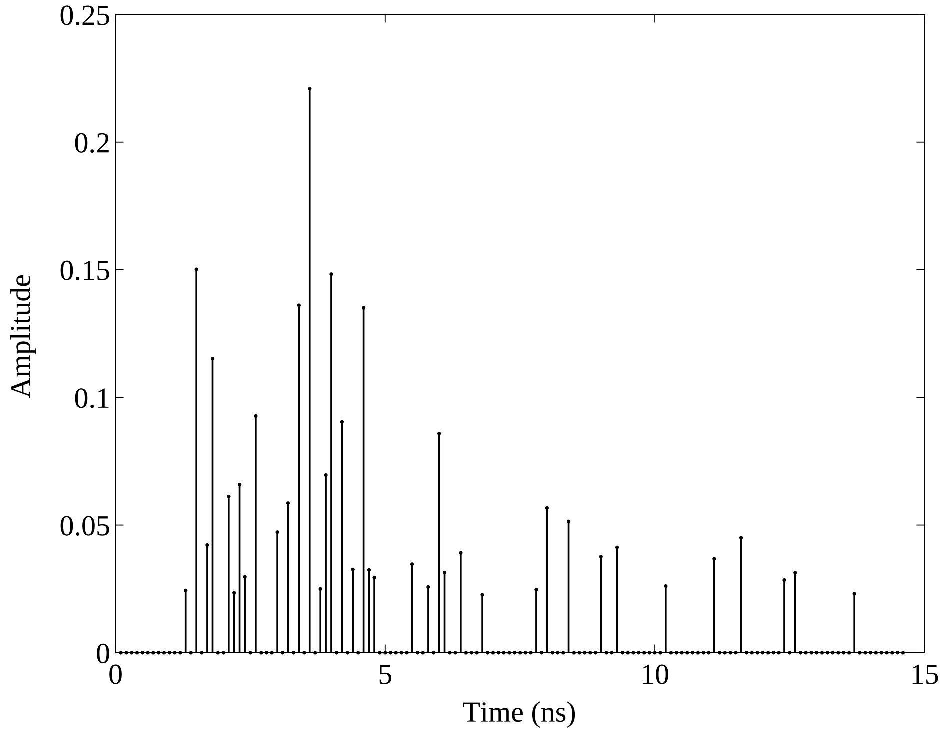

Figure 6.2: Example of deconvolved impulse response inside engine compartment.

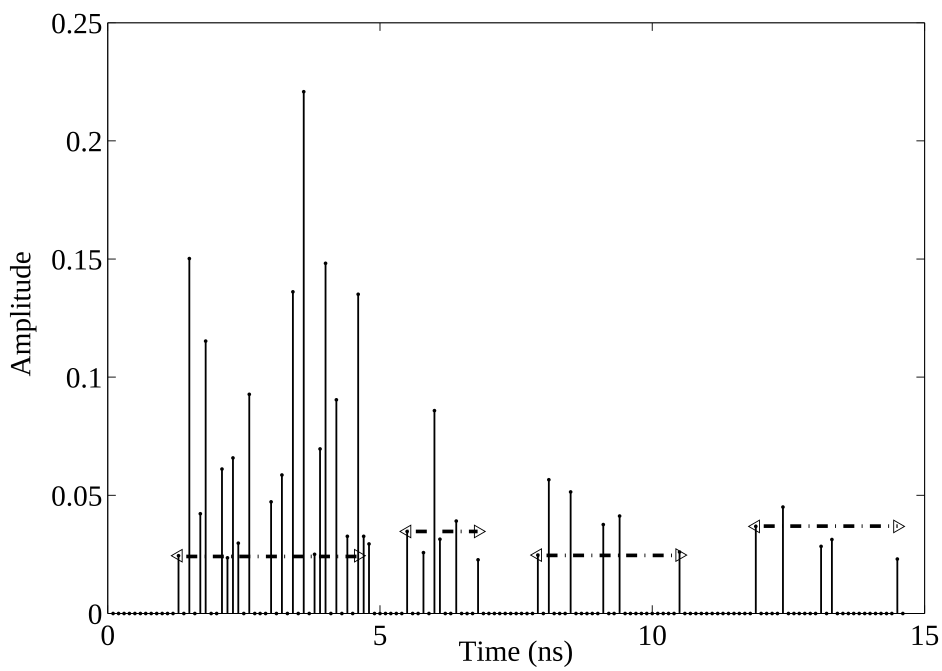

Figure 6.3: Identified clusters according to time intervals of neighboring paths.

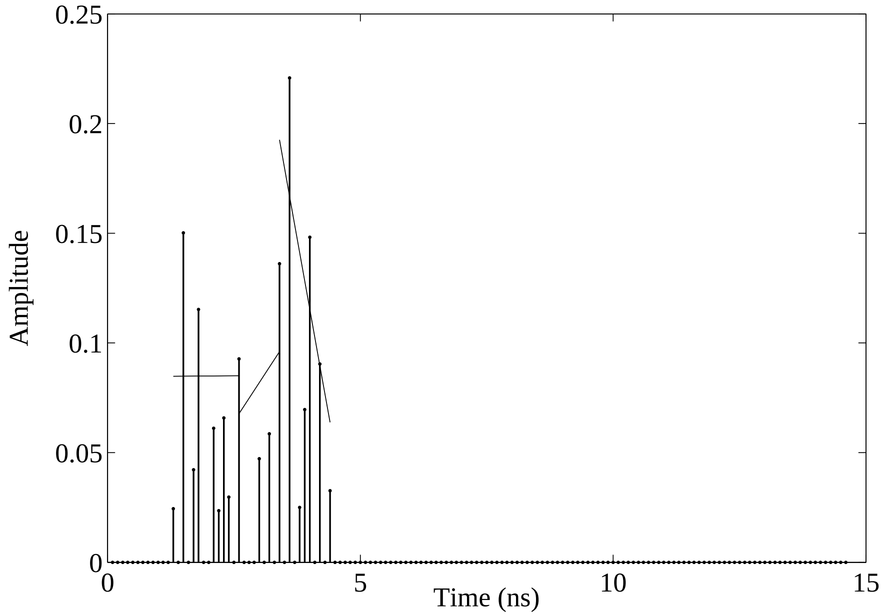

Figure 6.4: Identified clusters according to path amplitudes. The lines of best fit mark the beginnings and ends of possible new sub-clusters.

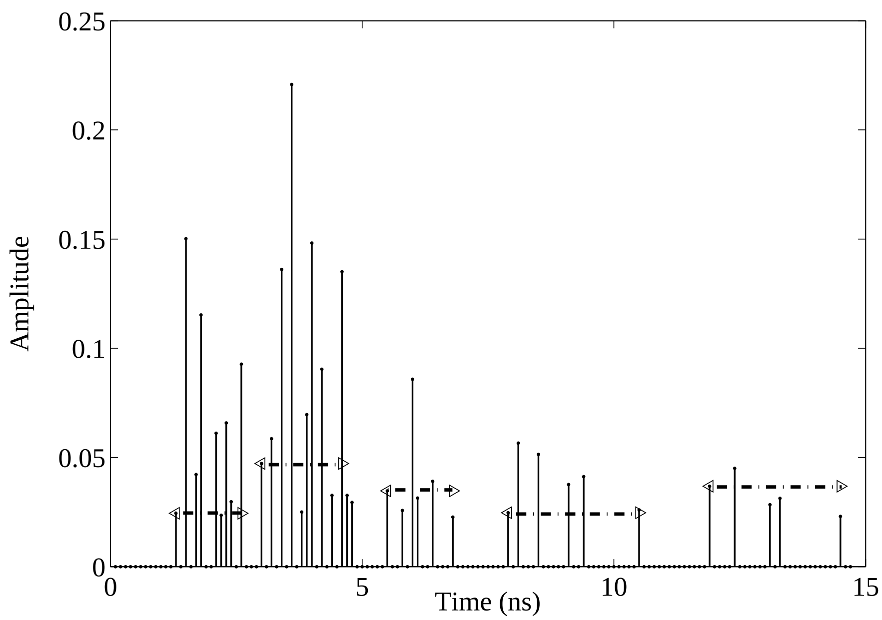

Figure 6.5: Final clusters identified by the algorithm.

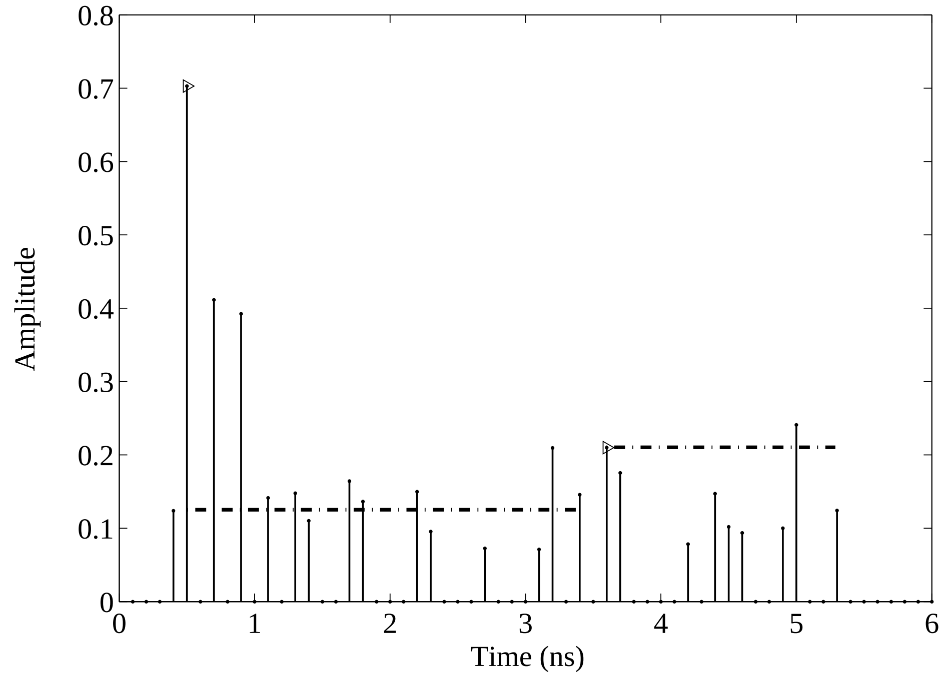

Figure 6.6: Identified clusters using the algorithm described in [82].

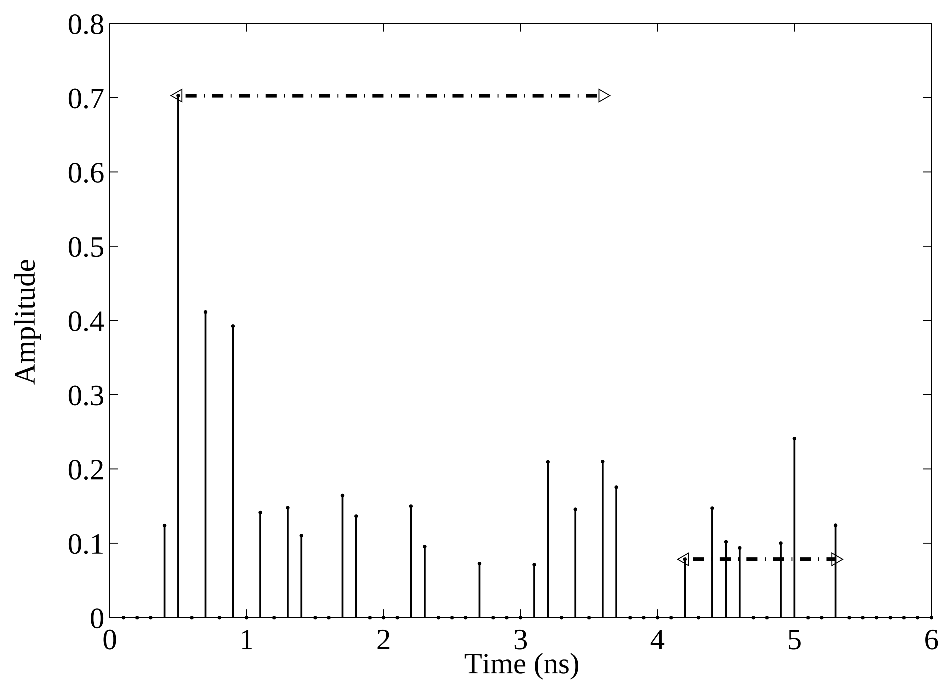

Figure 6.7: Identified clusters using the algorithm proposed in this chapter.

CHAPTER 7
DIGITAL SLIGHTLY FREQUENCY-SHIFTED TRANSMITTED REFERENCE UWB RECEIVER

7.1 Introduction

UWB propagation in the intra-vehicle environments features short range and relatively small delay spread, which means relatively high data rates can be achieved with properly designed UWB receivers [85]. A way to transmit data is to directly take advantage of a train of baseband pulses narrower than a nanosecond whose amplitudes or positions are modulated by the transmitted information. A system working in this way does not require any sinusoidal carrier and is called impulse radio UWB system (IR-UWB). This chapter focuses on the receiver design for such IR-UWB systems and only single user case is considered.

The bandwidth of a UWB pulse is as large as several gigahertz. It provides the ability to resolve multiple paths with ultra-fine delays so that the serious multi-path fading problem in narrow band systems does not exist. However, the large number of resolvable multi-path components also increases the complexity to the signal detection process. The main challenge in the design of UWB systems is the implementation of low-cost, low-complexity and high performance receivers.

In the UWB literature, the conventional rake receiver employed in spread spectrum systems has been intensively analyzed [25] [26]. A rake receiver is composed of multiple correlators which are called fingers. Each finger independently detects a resolvable multi-path component in the received signal and the energy captured at all fingers is combined at last. However, there are two major disadvantages with the UWB rake receiver. On one hand, because the energy in a UWB signal spreads over tens of resolved multi-path components, as many as tens of fingers are required in a rake receiver to capture enough energy. This makes it too complicated and costly to implement the receiver. On the other hand, rake receiver also requires a robust estimation of the delays and strengths of all multi-path components, which is very difficult when the noise level is high because the energy of each component is very low in UWB signals resulting from the energy spreading over a large number of components [24] [27] [86] [87].

To overcome the drawbacks of the conventional rake receiver, R. Hoctor, H. Tomlinson, etc. proposed to apply the transmitted reference signaling scheme to UWB systems [30] [31]. The basic idea of the TR system is to transmit the UWB pulses in pair with some delay between them. The first is a reference pulse and the second is a data-bearing one. At the TR receiver, the received reference signal is correlated with the data-bearing signal to detect the transmitted data. It can be seen that the reference signal is used as the estimation of the UWB channel response and hence an assumption is that the channel keeps invariant during the transmission of the reference and the data-bearing signals. As long as the pair of signals is transmitted within the coherence time of the channel, this assumption is reasonable and acceptable. The TR receiver suffers from power inefficiency caused by the transmission of additional signal as reference and the problem of noise-corrupted reference signal used as the correlator template, but it still attracts the attention of many UWB researchers because its structure is very simple. Some work has been done to overcome the inefficiency by using the previous data signal as reference [34], some other effort has been made to overcome the noisy template by using the average of several reference signals to correlate with the data-bearing signal [32], and a lot of work to derive the performance of TR receivers has been reported in the literature [33] [35] [36].

Although the architecture of the UWB TR receiver is simple in theory, the practical implementation is very difficult because it requires an analog delay unit capable of processing an ultra-wideband signal. To eliminate the need for such a time delay unit, a slightly frequency-shifted TR receiver has been proposed in [37] [38] [39]. Instead of a time-shifted reference signal, SFS TR signaling scheme uses an unmodulated UWB signal shifted in frequency domain as the reference and transmits it together with the data-bearing signal. In order to assure that the reference signal and the data signal experience the same level of channel fading, the frequency shift is selected so that it is a lot less than the coherence frequency of the channel. Performance analysis of such a receiver shows that it works fine for low-data-rate applications, such as the intra-vehicle UWB sensor network where the receiver is required to support 100 sensors with each transmitting at least one sample of 16 bits to ECU per second [37] [38] [39] [40]. Although this SFS TR system removes the requirement for an analog delay unit, which simplifies the implementation, it is still less flexible than a digital version of itself. Due to the availability of integrated and sophisticated digital signaling circuits, digital method provides convenient access to powerful digital signal processing (DSP) algorithms, reduces the complexity and increases the flexibility in the implementation of receivers. This chapter proposes a digital version of the SFS TR receiver which is implemented with an analog-to-digital converter (ADC). The implementation of a high sampling rate high resolution low power ADC is difficult and too expensive to achieve with current CMOS technology [88] [89] [90] [91], so this chapter works on low resolution quantizers which quantize the signals by as low as three bits per sample.

In this chapter, the general system model and the structure of the digital SFS TR receiver are given in Section 7.2. The performance of the discrete time full resolution SFS TR receiver with unquantized samples is derived in Section 7.3. Section 7.4 gives the performance analysis of the quantized SFS TR receiver with low resolution. The simulation and numerical results are given in Section 7.5, and Section 7.6 concludes the chapter.

7.2 System Model

The digital version of a SFS TR receiver is illustrated in Fig. 7.1. The received signal $\tilde{r}(t)$ is filtered by an ideal low-pass filter (LPF) to remove the noise outside the signal bandwidth B. The signal $r(t)$ output from the filter is first sampled with rate f_s larger than Nyquist rate and then quantized by an ADC. The digitized signal $r_q(n)$ is fed into a digital signal processor together with the digitized version of a cosine signal. In the DSP unit, $r_q(n)$ is first multiplied by the digital cosine signal for the purpose of frequency shifting and then correlated with itself to decide the received data.

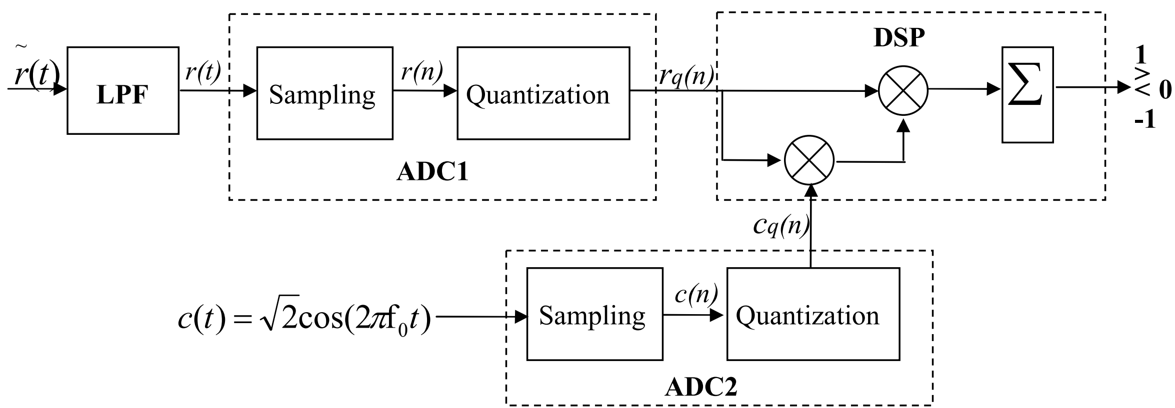

Figure 7.1: Structure of the Digital SFS TR Receiver.

In a single user analog SFS TR signaling scheme, the transmitted signal in one symbol interval consisting of N_f frames of length T_f is given by

$$s(t) = \sqrt{\frac{E_s}{2}}[u(t) + b\sqrt{2}\cos(2\pi f_0 t)u(t)] \qquad (0 \leq t < T_s), \tag{7.1}$$

where

$$u(t) = \sum_{k=0}^{N_f-1} p(t - kT_f) \tag{7.2}$$

is a sequence of N_f unmodulated UWB pulses whose energy is normalized to be $1/N_f$, E_s is the total signal energy within the symbol period, b is the data to be transmitted which equals '-1' or '1', and f_0 is the frequency used to shift $u(t)$ [37] [38] [39]. Assuming the length of a symbol is $T_s = N_f T_f$, the value of f_0 is set to be $\frac{1}{T_s}$ so that it is much less than the channel coherence frequency [37] [38] [39]. It can be seen that the transmitted signal is a sum of the reference signal $u(t)$ and its frequency shifted version modulated by the transmission information. Assuming $h(t)$ is the combined impulse response of the channel and the LPF, the received signal can be expressed as

$$r(t) = x(t) + v(t), \tag{7.3}$$

in which $x(t) = s(t) * h(t)$ is the received noise-free signal after the ideal LPF, and noise $v(t)$ is a zero mean, AWGN random process with two-sided power spectral density $N_0/2$. As defined in paper [37] [38] [39], without ADC, the output from the correlator of an analog SFS-TR receiver used to decide the transmitted data is given by

$$Z = \int_0^{T_s} r(t)r(t)\sqrt{2}c(t)dt, \tag{7.4}$$

where

$$c(t) = \cos(2\pi f_0 t). \tag{7.5}$$

Accordingly, if the received signal $r(t)$ after the LPF is sampled at Nyquist rate f_s to get the discrete time full resolution signal $r(n)$ and then quantized with stepsize Δ by the ADC to get the quantized digital signal $r_q(n)$, we have

$$s(n) = \sqrt{\frac{E_s}{2}}[u(n) + b\sqrt{2}c(n)u(n)], \tag{7.6}$$

$$x(n) = s(n) * h(n), \tag{7.7}$$

$$r(n) = x(n) + v(n), \tag{7.8}$$

$$r_q(n) = r(n) + e_q(n), \tag{7.9}$$

where $s(n)$, $h(n)$, $u(n)$, $c(n)$ are the discrete time signals corresponding to $s(t)$, $h(t)$, $u(t)$, $c(t)$ respectively, $v(n)$ is the i.i.d. zero mean white Gaussian noise sequence with variance $\sigma^2 = N_0 f_s/2$, and $e_q(n)$ is the quantization error.

7.3 Performance Analysis of a Full resolution Digital Receiver

Considering an ADC of infinite resolution in the digital SFS TR receiver, when the data bit $b = 1$ is transmitted and N samples are taken in a symbol period, the received signal without noise is given by

$$x(n) = \sqrt{\frac{E_s}{2}} u(n) * h(n) + \sqrt{E_s}[u(n)c(n)] * h(n), \tag{7.10}$$

and the correlator output is

$$\begin{aligned} Z &= \sum_{n=0}^{N-1} \sqrt{2} r^2(n) c(n) = \sum_{n=0}^{N-1} \sqrt{2}[x(n) + v(n)]^2 c(n) \\ &= \sqrt{2} \sum_{n=0}^{N-1} x^2(n)c(n) + 2\sqrt{2} \sum_{n=0}^{N-1} x(n)v(n)c(n) + \sqrt{2} \sum_{n=0}^{N-1} v^2(n)c(n). \end{aligned} \tag{7.11}$$

Let Z_1, Z_3, and Z_2 denote the three terms in the above equation of Z respectively. We have

$$Z_1 = \sqrt{2} \sum_{n=0}^{N-1} x^2(n)c(n), \tag{7.12}$$

$$Z_2 = 2\sqrt{2} \sum_{n=0}^{N-1} x(n)v(n)c(n), \tag{7.13}$$

$$Z_3 = \sqrt{2} \sum_{n=0}^{N-1} v^2(n)c(n). \tag{7.14}$$

It can be seen that Z_1 only consists of deterministic signal component while Z_2 and Z_3 are noise corrupted signals. The expectations of these sub-terms are

$$E[Z_1] = Z_1, \tag{7.15}$$

$$E[Z_2] = 2\sqrt{2} \sum_{n=0}^{N-1} x(n)c(n)E[v(n)] = 0, \tag{7.16}$$

$$E[Z_3] = \sqrt{2}\sum_{n=0}^{N-1} c(n)E[v^2(n)] = \sqrt{2}\sum_{n=0}^{N-1} c(n)\frac{N_0}{2} = 0. \tag{7.17}$$

As a result, the expectation of the correlator output can be represented by

$$\mu_z = Z_1 = \sqrt{2}\sum_{n=0}^{N-1} x^2(n)c(n). \tag{7.18}$$

To get the performance expression of the receiver, the variance of the correlator output is calculated as below

$$\sigma_z^2 = E[(Z_2 + Z_3)^2] = 4N_0 f_s \sum_{n=0}^{N-1} c^2(n)x^2(n) + \frac{NN_0^2 f_s^2}{2}. \tag{7.19}$$

Based on the above result and the assumption that the transmitted data equals '-1' or '1' with same probability, the bit error probability (BEP) of the discrete time full resolution SFS TR receiver can be expressed as

$$P_e = Q\left(\sqrt{\frac{\mu_z^2}{\sigma_z^2}}\right) = Q\left(\sqrt{\frac{2\left[\sum_{n=0}^{N-1} x^2(n)c(n)\right]^2}{4N_0 f_s \sum_{n=0}^{N-1}\left[x^2(n)c^2(n)\right] + \frac{NN_0^2 f_s^2}{2}}}\right). \tag{7.20}$$

Equation (7.20) represents the receiver's performance based on the received noise-free signal $x(t)$, which is the channel response of the transmitted signal $s(t)$. To derive a closed-form expression of the BEP explicitly including the channel information, it is assumed that the impulse response of the multi-path channel in an intra-vehicle environment can be represented as $h(t) = \sum_{l=0}^{L-1} \alpha_l \delta(t - \tau_l)$ in which L, α_l and τ_l are the number of paths, the amplitude and the delay of the paths respectively. In such a channel, the received noise-free signal can be expressed as $x(t) = \sum_{l=0}^{L-1} \alpha_l s(t - \tau_l)$ whose digital expression after the sampling process with rate f_s is $x(n) = \sum_{l=0}^{L-1} \alpha_l s(n - D_l)$, in which D_l is the discrete time delay of the lth path. Consequently, assuming that the number of samples in a frame time is $F = T_f f_s$, the sum in the denominator item in equation (7.20) can be calculated as

$$\sum_{n=0}^{N-1} x^2(n)c^2(n) = \sum_{n=0}^{N-1} [\sum_{l=0}^{L-1} \alpha_l s(n-D_l)]^2 c^2(n)$$
$$= \sum_{n=0}^{N-1} [\sum_{l=0}^{L-1} \sum_{m=0}^{L-1} \alpha_l s(n-D_l)\alpha_m s(n-D_m)] c^2(n)$$
$$= \sum_{l=0}^{L-1} \sum_{m=0}^{L-1} \alpha_l \alpha_m [\sum_{n=0}^{N-1} s(n-D_l)s(n-D_m)c^2(n)]$$
$$= \sum_{l=0}^{L-1} \sum_{m=0}^{L-1} \alpha_l \alpha_m \sum_{n=0}^{N-1} u(n-D_l)u(n-D_m)c^2(n)$$
$$[\sqrt{\frac{E_s}{2}} + \sqrt{E_s}c(n-D_l)][\sqrt{\frac{E_s}{2}} + \sqrt{E_s}c(n-D_m)]$$
$$= E_s \sum_{l=0}^{L-1} \sum_{m=0}^{L-1} \alpha_l \alpha_m \sum_{n=0}^{N-1} [\sum_{k=0}^{N_f-1} p(n-kF-D_l)][\sum_{i=0}^{N_f-1} p(n-iF-D_m)]$$
$$[\sqrt{\frac{1}{2}} + c(n-D_l)][\sqrt{\frac{1}{2}} + c(n-D_m)]c^2(n). \tag{7.21}$$

It is assumed that the paths in the channel impulse response do not overlay with each other, i.e., the time delay between any two paths is larger than the width of the UWB pulse. For the lth and the mth path in equation (7.21), when $l \neq m$, we have

$$[\sum_{k=0}^{N_f-1} p(n-kF-D_l)][\sum_{i=0}^{N_f-1} p(n-iF-D_m)] = 0. \tag{7.22}$$

As a result,

$$\sum_{n=0}^{N-1} x^2(n)c^2(n) = 0. \tag{7.23}$$

When $l = m$, we have

$$\sum_{n=0}^{N-1} x^2(n)c^2(n) = \frac{E_s}{t_s} \sum_{l=0}^{L-1} \alpha_l^2 [\frac{3}{8} + \frac{1}{4}c^2(D_l)]. \tag{7.24}$$

Similarly, the sum in the numerator item in equation (7.20) can be calculated as

$$\sum_{n=0}^{N-1} x^2(n)c(n) = \frac{1}{\sqrt{2}}\frac{E_s}{t_s}\sum_{l=0}^{L-1}\alpha_l^2 c(D_l). \tag{7.25}$$

Detail derivations of these two equations are given in Appendix A.

Substituting equation (7.24) and equation (7.25) into equation (7.20), we get the closed-form expression of the discrete time full resolution SFS TR receiver as

$$\begin{aligned} P_e &= Q\left(\frac{\frac{E_s}{t_s}\sum_{l=0}^{L-1}\alpha_l^2 c(D_l)}{\sqrt{4N_0 f_s \frac{E_s}{t_s}\sum_{l=0}^{L-1}\alpha_l^2[\frac{3}{8}+\frac{1}{4}c^2(D_l)] + \frac{1}{2}NN_0^2 f_s^2}}\right) \\ &= Q\left(\frac{\frac{E_s}{N_0}\sum_{l=0}^{L-1}\alpha_l^2 c(D_l)}{\sqrt{\frac{E_s}{N_0}\sum_{l=0}^{L-1}\alpha_l^2\left[\frac{3}{2}+c^2(D_l)\right] + \frac{1}{2}N}}\right). \end{aligned} \tag{7.26}$$

7.4 Quantized Low Resolution SFS TR Receiver

As stated in Section 7.1, in the structure of digital UWB receiver shown in Fig. 7.1, because the ADC has to support a high sampling rate in the order of gigahertz for UWB signals, the resolution of the ADC is proposed to be low so that the implementation of such a receiver will be feasible and not too costly. Assuming a roundoff quantizer with a uniform stepsize Δ is used in the ADC and the quantizer is not overloaded, the input to the quantizer is the samples of the received signal $r(n)$ [92]. It relates to the quantizer output $r_q(n)$ by equation (7.9). Now the decision variable of the quantized digital receiver turns into

$$Z_q = \sum_{n=0}^{N-1}\sqrt{2}r_q^2(n)c_q(n) = \sqrt{2}\sum_{n=0}^{N-1}[r(n)+e_q(n)]^2 c_q(n), \tag{7.27}$$

in which $c_q(n)$ is the quantized samples of the cosine function $c(n)$ in equation (7.6). The expected value of Z_q is written as

$$\mu_{Z_q} = \sqrt{2}\sum_{n=0}^{N-1}(E[r^2(n)+e_q^2(n)+2r(n)e_q(n)])c_q(n). \tag{7.28}$$

And the square of the expected value of Z_q is calculated as

$$\begin{aligned}
\mu_{Z_q}^2 &= 2\sum_{n=0}^{N-1}\sum_{m=0}^{N-1} E[r^2(m)]E[r^2(n)]c_q(m)c_q(n) \\
&+ 2\sum_{n=0}^{N-1}\sum_{m=0}^{N-1} E[e_q^2(m)]E[e_q^2(n)]c_q(m)c_q(n) \\
&+ 8\sum_{n=0}^{N-1}\sum_{m=0}^{N-1} E[r(m)e_q(m)]E[r(n)e_q(n)]c_q(m)c_q(n) \\
&+ 4\sum_{n=0}^{N-1}\sum_{m=0}^{N-1} E[r^2(n)]E[e_q^2(m)]c_q(m)c_q(n) \\
&+ 8\sum_{n=0}^{N-1}\sum_{m=0}^{N-1} E[r^2(n)]E[r(m)e_q(m)]c_q(m)c_q(n) \\
&+ 8\sum_{n=0}^{N-1}\sum_{m=0}^{N-1} E[e_q^2(n)]E[r(m)e_q(m)]c_q(m)c_q(n). \qquad (7.29)
\end{aligned}$$

In addition, the expectation of the square of Z_q can be written as

$$\begin{aligned}
E[Z_q^2] &= 2\sum_{n=0}^{N-1}\sum_{m=0}^{N-1} E[r^2(m)r^2(n)]c_q(m)c_q(n) \\
&+ 2\sum_{n=0}^{N-1}\sum_{m=0}^{N-1} E[e_q^2(m)e_q^2(n)]c_q(m)c_q(n) \\
&+ 8\sum_{n=0}^{N-1}\sum_{m=0}^{N-1} E[r(m)e_q(m)r(n)e_q(n)]c_q(m)c_q(n) \\
&+ 4\sum_{n=0}^{N-1}\sum_{m=0}^{N-1} E[r^2(n)e_q^2(m)]c_q(m)c_q(n) \\
&+ 8\sum_{n=0}^{N-1}\sum_{m=0}^{N-1} E[r^2(n)r(m)e_q(m)]c_q(m)c_q(n) \\
&+ 8\sum_{n=0}^{N-1}\sum_{m=0}^{N-1} E[e_q^2(n)r(m)e_q(m)]c_q(m)c_q(n). \qquad (7.30)
\end{aligned}$$

If the variance of Z_q is represented as $\sigma^2_{Z_q}$, based on equations (7.28) - (7.30), we can get the expression of $\sigma^2_{Z_q}$ as

$$\begin{aligned}\sigma^2_{Z_q} = E[Z_q^2] - \mu^2_{Z_q} &= 2N\sigma^4 + 8\sigma^2 \sum_{n=0}^{N-1} x^2(n)c_q^2(n) \\ &- 2\sum_{n=0}^{N-1} E[e_q^2(n)]^2 c_q^2(n) - 4\sum_{n=0}^{N-1} E[r^2(n)]E[e_q^2(n)]c_q^2(n) \\ &+ 8\sum_{n=0}^{N-1} E[r^3(n)e_q(n)]c_q^2(n) + 8\sum_{n=0}^{N-1} E[e_q^3(n)r(n)]c_q^2(n) \\ &- 8\sum_{n=0}^{N-1} E[r(n)e_q(n)]^2 c_q^2(n) + 12\sum_{n=0}^{N-1} E[r^2(n)e_q^2(n)]c_q^2(n) \\ &- 8\sum_{n=0}^{N-1} E[r^2(n)]E[r(n)e_q(n)]c_q^2(n) + 2\sum_{n=0}^{N-1} E[e_q^4(n)]c_q^2(n) \\ &- 8\sum_{n=0}^{N-1} E[e_q^2(n)]E[r(n)e_q(n)]c_q^2(n). \end{aligned} \tag{7.31}$$

It is known from equation (7.8) that the input $r(n)$ to the quantizer is a Gaussian random sequence with mean $x(n)$ and variance $\sigma^2 = \frac{N_0 f_s}{2}$, thus

$$E[r^2(n)] = x^2(n) + \sigma^2, \tag{7.32}$$

and the characteristic function of $r(n)$ is

$$\phi_r(\omega) = e^{jx(n)\omega - \sigma^2\omega^2/2}. \tag{7.33}$$

According to the modified Quantization Theorem as proposed in [93], when such a Gaussian random sequence is quantized with stepsize Δ, the probability density function of the quantization error $e_q(n)$ is

$$f_{e_q}(\epsilon) = \begin{cases} \frac{1}{\Delta} + \frac{1}{\Delta}\sum_{k\neq 0} \phi_r(\frac{2k\pi}{\Delta})e^{\frac{-j2k\pi\epsilon}{\Delta}}, & -\frac{\Delta}{2} \leq \epsilon \leq \frac{\Delta}{2} \\ 0, \quad otherwise. \end{cases} \tag{7.34}$$

By substituting $\phi_r(\omega)$ into equation (7.34), we can get the final expression for the probability density function of $e_q(n)$

$$f_{e_q}(\epsilon) = \begin{cases} \frac{1}{\Delta} + \frac{2}{\Delta}\sum_{k=1}^{\infty} e^{-\frac{2k^2\pi^2\sigma^2}{\Delta^2}} \cos(\frac{2k\pi(x(n)-\epsilon)}{\Delta}), & -\frac{\Delta}{2} \leq \epsilon \leq \frac{\Delta}{2} \\ 0, \quad otherwise. \end{cases} \tag{7.35}$$

As a result, from equation (7.35), we can calculate the following expectations of the quantization error $e_q(n)$ as

$$\begin{aligned} E[e_q^2(n)] &= \int_{-\frac{\Delta}{2}}^{\frac{\Delta}{2}} \epsilon^2 f_{e_q}(\epsilon) d\epsilon \\ &= \frac{\Delta^2}{12} + \sum_{k=1}^{\infty} e^{-\frac{2k^2\pi^2\sigma^2}{\Delta^2}} \int_{-\frac{\Delta}{2}}^{\frac{\Delta}{2}} \frac{2\epsilon^2}{\Delta} \cos(\frac{2k\pi(x(n)-\epsilon)}{\Delta}) d\epsilon \\ &= \frac{\Delta^2}{12} + \sum_{k=1}^{\infty} \frac{(-1)^k\Delta^2}{k^2\pi^2} \cos(\frac{2k\pi x(n)}{\Delta}) e^{-\frac{2k^2\pi^2\sigma^2}{\Delta^2}}, \end{aligned} \tag{7.36}$$

$$\begin{aligned} E[e_q^4(n)] &= \int_{-\frac{\Delta}{2}}^{\frac{\Delta}{2}} \epsilon^4 f_{e_q}(\epsilon) d\epsilon \\ &= \frac{\Delta^4}{80} + \sum_{k=1}^{\infty} e^{-\frac{2k^2\pi^2\sigma^2}{\Delta^2}} \int_{-\frac{\Delta}{2}}^{\frac{\Delta}{2}} \frac{2\epsilon^4}{\Delta} \cos(\frac{2k\pi(x(n)-\epsilon)}{\Delta}) d\epsilon \\ &= \sum_{k=1}^{\infty} e^{-\frac{2k^2\pi^2\sigma^2}{\Delta^2}} \cos(\frac{2k\pi x(n)}{\Delta})[\frac{(-1)^k\Delta^4}{2k^2\pi^2} - \frac{3(-1)^k\Delta^4}{k^4\pi^4}] + \frac{\Delta^4}{80}. \end{aligned} \tag{7.37}$$

Moreover, the correlation between the quantizer input $r(n)$ and the quantization error $e_q(n)$ is drived in paper [93] as

$$\begin{aligned} E[r(n)e_q(n)] = &\sum_{k=1}^{\infty} \sin(\frac{2k\pi x(n)}{\Delta}) e^{\frac{-2k^2\pi^2\sigma^2}{\Delta^2}} \frac{(-1)^k\Delta x(n)}{k\pi} \\ &+ 2\sum_{k=1}^{\infty} \cos(\frac{2k\pi x(n)}{\Delta}) e^{\frac{-2k^2\pi^2\sigma^2}{\Delta^2}} (-1)^k\sigma^2. \end{aligned} \tag{7.38}$$

Finally, because we know that the expectation of $r_q^4(n)$ is

$$E[r_q^4(n)] = E[r^4(n)] + 4E[r^3(n)e_q(n)] + 6E[r^2(n)e_q^2(n)] + 4E[r(n)e_q^3(n)] + E[e_q^4(n)], \tag{7.39}$$

and at the same time the following equation is also established,

$$E[r_q^4(n)] = \phi_{r_q}^{(4)}(\omega)|_{\omega=0}, \tag{7.40}$$

where $\phi_{r_q}(\omega)$ is the characteristic function of the quantizer output $r_q(n)$ and can be represented as [93]

$$\phi_{r_q}(\omega) = \sum_{k=-\infty}^{\infty} \phi_r(\omega - \frac{2k\pi}{\Delta})\frac{\sin(\Delta\omega/2 - k\pi)}{\Delta\omega/2 - k\pi}, \tag{7.41}$$

following similar procedure to the derivation of $E[r(n)e_q(n)]$, by calculating equation (7.40) and comparing its result with equation (7.39), we can get the expectations (refer to Appendix B for detail derivation),

$$E[r(n)e_q^3(n)] = \sum_{k=1}^{\infty} \phi_r'(\frac{-2k\pi}{\Delta})(-1)^k(\frac{\Delta^3}{8k\pi} - \frac{3\delta^3}{4k^3\pi^3}), \tag{7.42}$$

$$E[r^2(n)e_q^2(n)] = \frac{\Delta^2(x^2(n)+\sigma^2)}{12} - \sum_{k=1}^{\infty} \phi_r''(\frac{-2k\pi}{\Delta})\frac{(-1)^k\Delta^2}{2k^2\pi^2}, \tag{7.43}$$

$$E[r^3(n)e_q(n)] = -\sum_{k=1}^{\infty} \phi_r^{(3)}(\frac{-2k\pi}{\Delta})\frac{(-1)^k\Delta}{k\pi}. \tag{7.44}$$

Substitute equations (7.36) - (7.38) and equations (7.42) - (7.44) into equations (7.28) and (7.31), we get the mean value of Z_q as

$$\begin{aligned}\mu_{Z_q} =& \sqrt{2}[\sum_{n=0}^{N-1} x^2(n)c_q(n) \\ &+ \sum_{n=0}^{N-1}\sum_{k=1}^{\infty} c_q(n)\cos(\frac{2k\pi x(n)}{\Delta})e^{\frac{-2k^2\pi^2\sigma^2}{\Delta^2}}(-1)^k(\frac{\Delta^2}{k^2\pi^2} + 4\sigma^2) \\ &+ 2\sum_{n=0}^{N-1}\sum_{k=1}^{\infty} c_q(n)\sin(\frac{2k\pi x(n)}{\Delta})e^{\frac{-2k^2\pi^2\sigma^2}{\Delta^2}}\frac{(-1)^k\Delta x(n)}{k\pi}]\end{aligned} \tag{7.45}$$

The final expression of the variance of Z_q is derived as

$$\begin{aligned}
\sigma_{Z_q}^2 =& 2N\sigma^4 + \frac{N\Delta^4}{180} + \frac{N\sigma^2\Delta^2}{3} + (\frac{2\Delta^2}{3} + 8\sigma^2)\sum_{n=0}^{N-1} c_q^2(n)x^2(n) \\
&+ \sum_{n=0}^{N-1}\sum_{k=1}^{\infty} c_q^2(n)\cos(\frac{2k\pi x(n)}{\Delta})e^{\frac{-2k^2\pi^2\sigma^2}{\Delta^2}}(-1)^k \\
&\quad [\frac{6\Delta^4}{k^4\pi^4} - \frac{2\Delta^4 - 48\sigma^2\Delta^2 + 24\Delta^2x^2(n)}{3k^2\pi^2} \\
&\qquad + (16\sigma^4 - 32\sigma^2x^2(n) - \frac{8\sigma^2\Delta^2}{3} + \frac{64k^2\pi^2\sigma^6}{\Delta^2})] \\
&+ \sum_{n=0}^{N-1}\sum_{k=1}^{\infty} c_q^2(n)\sin(\frac{2k\pi x(n)}{\Delta})e^{\frac{-2k^2\pi^2\sigma^2}{\Delta^2}}(-1)^k \\
&\quad [\frac{4\Delta^3x(n) - 96\sigma^2\Delta x(n)}{3k\pi} - \frac{12\Delta^3x(n)}{k^3\pi^3} - \frac{16k\pi\sigma^4x(n)}{\Delta}] \\
&- 32\sum_{n=0}^{N-1} c_q^2(n)[\sum_{k=1}^{\infty}(-1)^k\sigma^2\cos(\frac{2k\pi x(n)}{\Delta})e^{\frac{-2k^2\pi^2\sigma^2}{\Delta^2}}]^2 \\
&- 2\sum_{n=0}^{N-1} c_q^2(n)[\sum_{k=1}^{\infty}\frac{(-1)^k}{k^2\pi^2}\Delta^2\cos(\frac{2k\pi x(n)}{\Delta})e^{\frac{-2k^2\pi^2\sigma^2}{\Delta^2}}]^2 \\
&- 8\sum_{n=0}^{N-1} c_q^2(n)[\sum_{k=1}^{\infty}\frac{(-1)^k\Delta x(n)}{k\pi}\sin(\frac{2k\pi x(n)}{\Delta})e^{\frac{-2k^2\pi^2\sigma^2}{\Delta^2}}]^2 \\
&- 16\sum_{n=0}^{N-1} c_q^2(n)[\sum_{k=1}^{\infty}\frac{(-1)^k}{k^2\pi^2}\Delta^2\cos(\frac{2k\pi x(n)}{\Delta})e^{\frac{-2k^2\pi^2\sigma^2}{\Delta^2}}] \\
&\qquad [\sum_{k=1}^{\infty}(-1)^k\sigma^2\cos(\frac{2k\pi x(n)}{\Delta})e^{\frac{-2k^2\pi^2\sigma^2}{\Delta^2}}] \\
&- 32\sum_{n=0}^{N-1} c_q^2(n)[\sum_{k=1}^{\infty}\frac{(-1)^k}{k\pi}\Delta x(n)\sin(\frac{2k\pi x(n)}{\Delta})e^{\frac{-2k^2\pi^2\sigma^2}{\Delta^2}}] \\
&\qquad [\sum_{k=1}^{\infty}(-1)^k\sigma^2\cos(\frac{2k\pi x(n)}{\Delta})e^{\frac{-2k^2\pi^2\sigma^2}{\Delta^2}}] \\
&- 8\sum_{n=0}^{N-1} c_q^2(n)[\sum_{k=1}^{\infty}\frac{(-1)^k}{k^2\pi^2}\Delta^2\cos(\frac{2k\pi x(n)}{\Delta})e^{\frac{-2k^2\pi^2\sigma^2}{\Delta^2}}] \\
&\qquad [\sum_{k=1}^{\infty}\frac{(-1)^k}{k\pi}\Delta x(n)\sin(\frac{2k\pi x(n)}{\Delta})e^{\frac{-2k^2\pi^2\sigma^2}{\Delta^2}}].
\end{aligned} \tag{7.46}$$

The performance of the quantized digital receiver is just

$$P_{e_q} = Q\left(\frac{\mu_{Z_q}}{\sqrt{\sigma^2_{Z_q}}}\right), \tag{7.47}$$

where μ_{Z_q} and $\sigma^2_{Z_q}$ are shown in equation (7.45) and (7.46).

7.5 Simulations and Numerical Results

Simulations have been run to evaluate the accuracy of the bit error probability expression for the discrete time full resolution SFS TR receiver in equation (7.26) as well as that for the quantized digital SFS TR receiver in equations (7.45) - (7.47). In all simulations, the second derivative of a Gaussian

$$p(t) = \left\{1 - 4\pi\left[\frac{t - T_p/2}{0.39T_p}\right]^2\right\} exp\left(-2\pi\left[\frac{t - T_p/2}{0.39T_p}\right]^2\right)$$

has been used as the shape of the transmitted UWB pulse and the width of the pulse T_p has been set to 0.668 ns as shown in Fig. 7.2 [24] [94]. In order to assess the receivers' performance in all kinds of typical environments, impulse responses randomly selected for the intra-vehicle UWB channels beneath the chassis and inside the engine compartment as well as for the 802.15.3a channel model 3 (CM3) and 802.15.4a office NLOS channel model have been used in the simulations to characterize the multi-path UWB channels [21] [22] [85]. Fig. 7.3 shows examples of typical impulse responses in these four environments. In addition, the transmitted data have been set to be '1's and '-1's with equal probabilities. At the same time, for the same set of channel impulse responses, BEPs are also calculated via equations (7.26) and (7.47) so that they can be compared with the simulation results.

7.5.1 Discrete Time Full resolution SFS TR Receiver

In the case of the discrete time full resolution SFS TR receiver, the resulting bit error probability from both the simulations and the theoretical calculations are shown together in Fig. 7.4, Fig. 7.5 and Fig. 7.6. Fig. 7.4 is based on the impulse re-

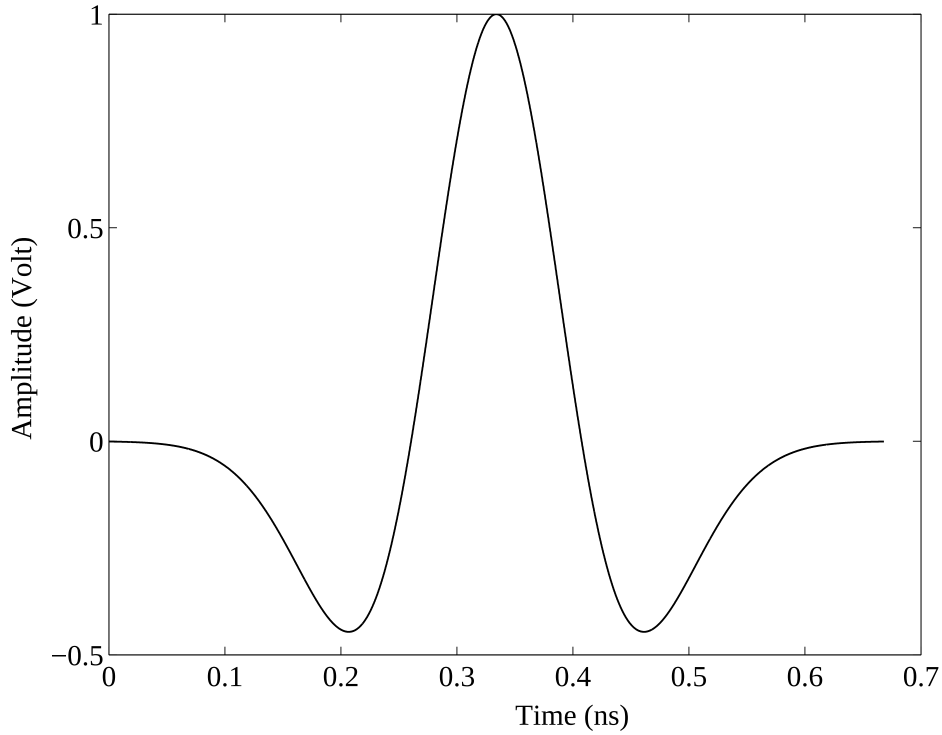

Figure 7.2: The second derivative of a Gaussian used as the shape of UWB pulses in the simulations.

sponses measured beneath vehicle chassis, Fig. 7.5 is based on the impulse responses measured inside vehicle engine compartment, and Fig. 7.6 is based on the impulse responses generated by 802.15.3a channel model 3. In these figures, the dotted lines represent BEPs from theoretical calculations while the solid lines stand for the simulated results. The sampling rate has been set to 40 GHz in both Fig. 7.4 and Fig. 7.5 while it is 6 GHz in Fig 7.6. The frame length T_f has been respectively set to 6.5 ns, 4.5 ns and 431.5 ns in Fig. 7.4, Fig. 7.5 and Fig 7.6. In addition, for all three figures, N_f, the number of frames in a symbol period, has taken the values of 20, 15, 10, 5, 2, corresponding to data rates from low to high marked in each figure. It can be seen that in all environments described here, the receiver's theoretical BEPs calculated from equation (7.26) match their simulated results almost perfectly except when the frame number is 2. This is reasonable because an assumption in the derivation of equation (7.26) is that the frame numbers should be relatively large as mentioned in appendix A. Consequently, the simulated results validate the accuracy of equation (7.26) to describe the bit error rate for the discrete time full resolution SFS TR receiver in each environment.

To compare the performance of this full resolution SFS TR receiver in different environments, Fig. 7.7 shows the theoretical BEPs versus the energy of the UWB pulses calculated against 802.15.3a CM3 and the office none-line-of-sight (NLOS) model defined in 802.15.4a [21] [22]. It is observed that with same data transmission rates, the receiver performs better in the office environment, which is caused by the fact that there are much more paths in the IRs of 802.15.3a CM3 as illustrated in Fig. 7.3. Furthermore, compared with the analog version of SFS TR UWB receiver reported in [37] [38] [39], this discrete time full resolution receiver achieves the same level of BEPs in the same environments at the same data rates, which means that the time discretization with Nyquist rate does not cause deterioration to the receiver's performance.

7.5.2 Quantized Low-resolution Digital SFS TR Receiver

In the case of the quantized digital SFS TR receiver, for simulation purpose, the quantizer scale is set to be equal to the maximum amplitude in the received signal $r(n)$ to make sure there is no overload in the quantization process. Eight quantization levels have been simulated, corresponding to a 3-bit low resolution quantizer. As for the theoretical calculation of BEP, the value of k in equation (7.45) and (7.46) increases from 1 to 8 to balance the implementation performance and accuracy. As a matter of fact, experimental calculations reveals that the large values of k only cause very trivial change to BEP which can be ignored. The simulated and the calculated BEPs are shown in Fig.7.8, Fig. 7.9 and Fig. 7.10 for the impulse responses beneath vehicle chassis, inside vehicle engine compartment and generated by 802.15.3a channel model 3 respectively. These three figures show the similar set of data rates and frame numbers as those in Fig. 7.4 and Fig. 7.6. Because a relatively large frame number is the pre-requisite in derivation of the receiver performance, BEPs for the frame number of 2 are not included here. Again, as we can see, the simulated digital receiver performance matches the theoretically derived one very well. This confirms that equations (7.45)-(7.47) are good representations for the performance of digital SFS TR receivers working with quantization resolution as low as 3 bits.

7.6 Conclusion

This chapter works on the development of a digital UWB SFS TR receiver. The performance of both the full resolution and the quantized digital receiver has been derived. Simulated receiver performance, based on the channel data of intra-vehicle environment beneath chassis and inside engine compartment, as well as 802.15.3a channel model 3 and 802.15.4a office NLOS model, agrees well with the derived closed-form performance representation. This confirms the accuracy of the derived BEP, hence indicates the possibility of implementing a low cost low complexity digital UWB SFS TR receiver. In addition, simulated and calculated results also indicate that such a digital SFS TR receiver performs much better for those environments with much less multi-paths such as the intra-vehicle environment beneath chassis or inside engine compartment.

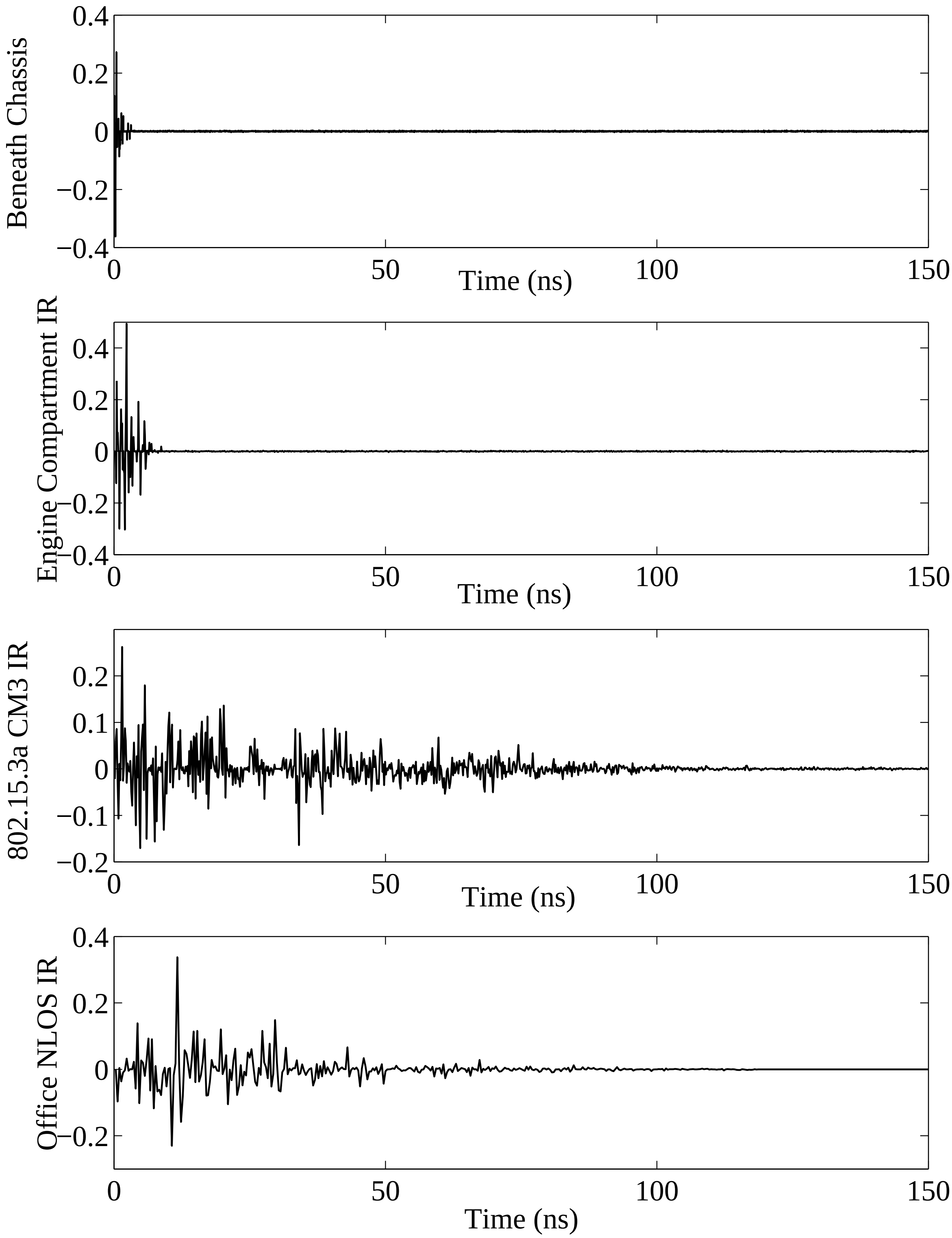

Figure 7.3: Examples of typical impulse responses for the UWB channels beneath chassis, inside engine compartment, 802.15.3a CM3 and 802.15.4a Office NLOS.

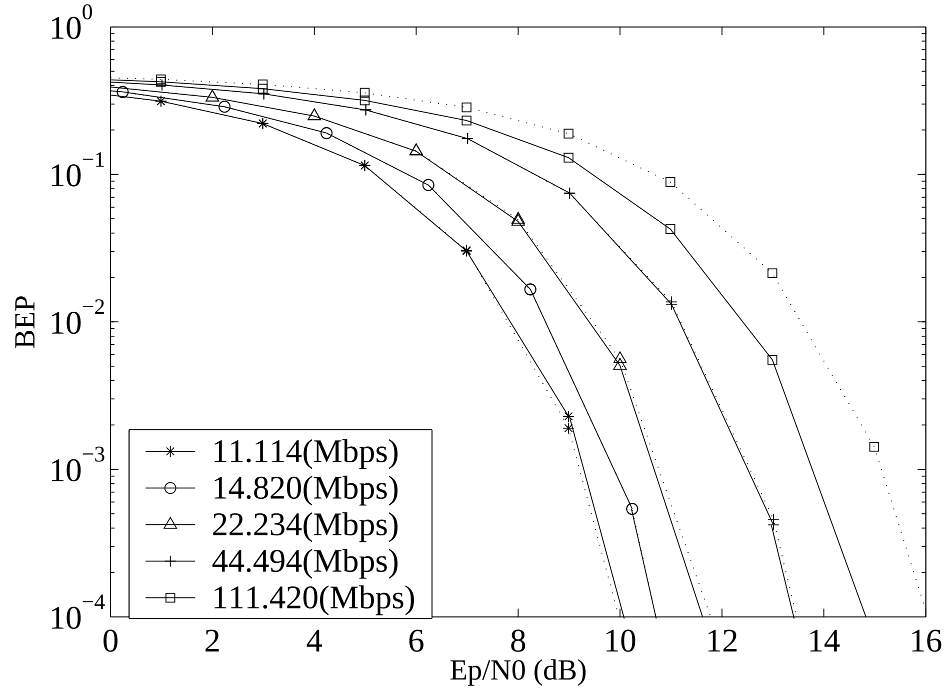

Figure 7.4: Simulated and calculated BEP versus UWB pulse energy of the discrete time full resolution SFS TR receiver for the channel beneath chassis.

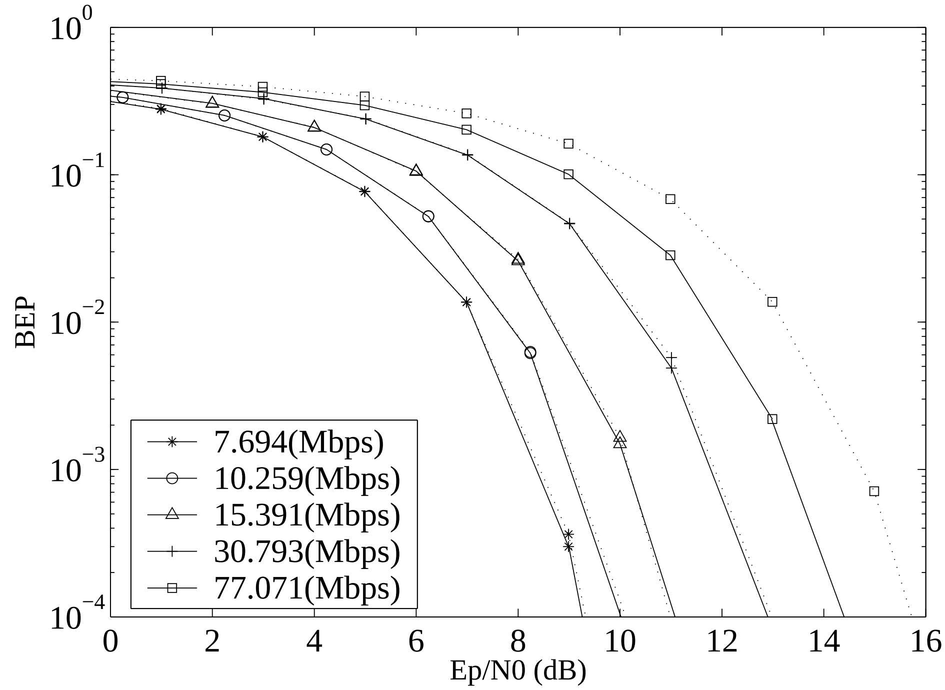

Figure 7.5: Simulated and calculated BEP versus UWB pulse energy of the discrete time full resolution SFS TR receiver for the channel inside engine compartment.

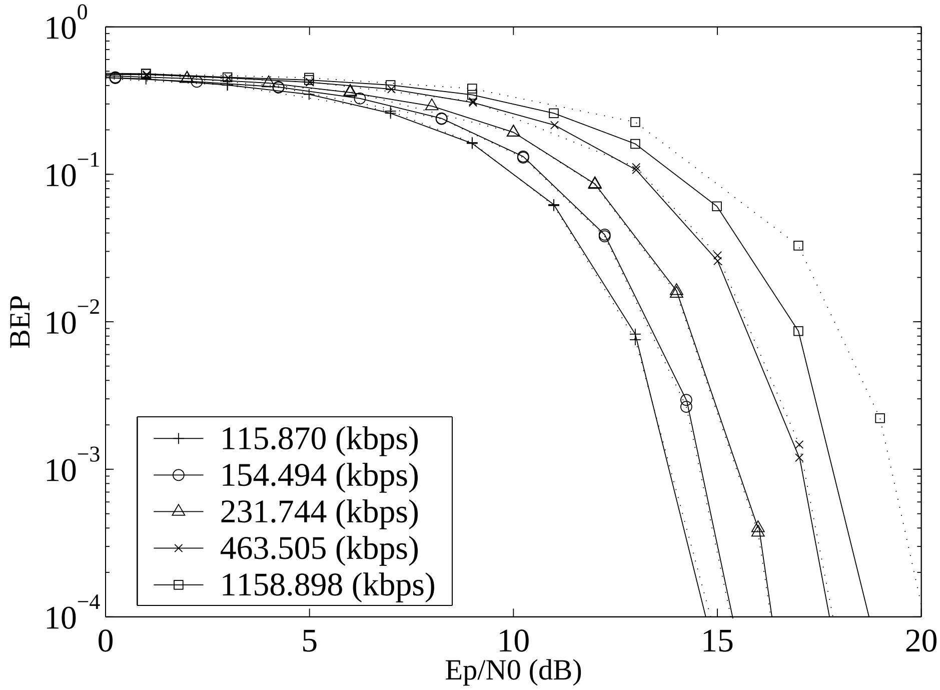

Figure 7.6: Simulated and calculated BEP versus UWB pulse energy of the discrete time full resolution SFS TR receiver for 802.15.3a CM3.

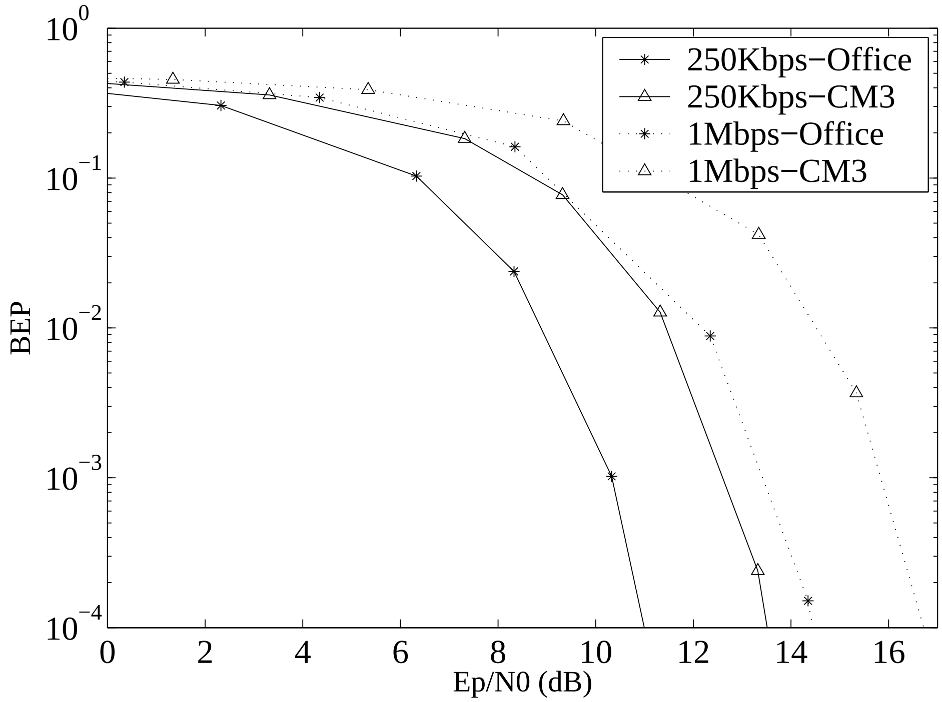

Figure 7.7: Performance of the discrete time full resolution SFS TR receiver in 802.15.3a CM3 and 802.15.4a office NLOS environments at the same data rates.

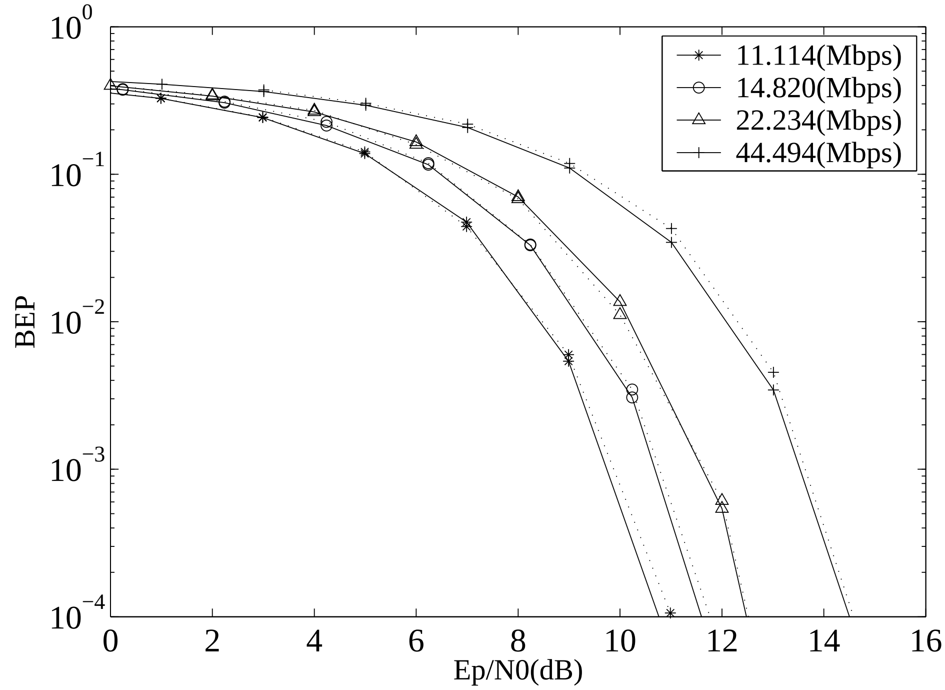

Figure 7.8: Simulated and calculated BEP versus UWB pulse energy of the quantized digital SFS TR receiver with 3-bit resolution for the channel IR beneath chassis.

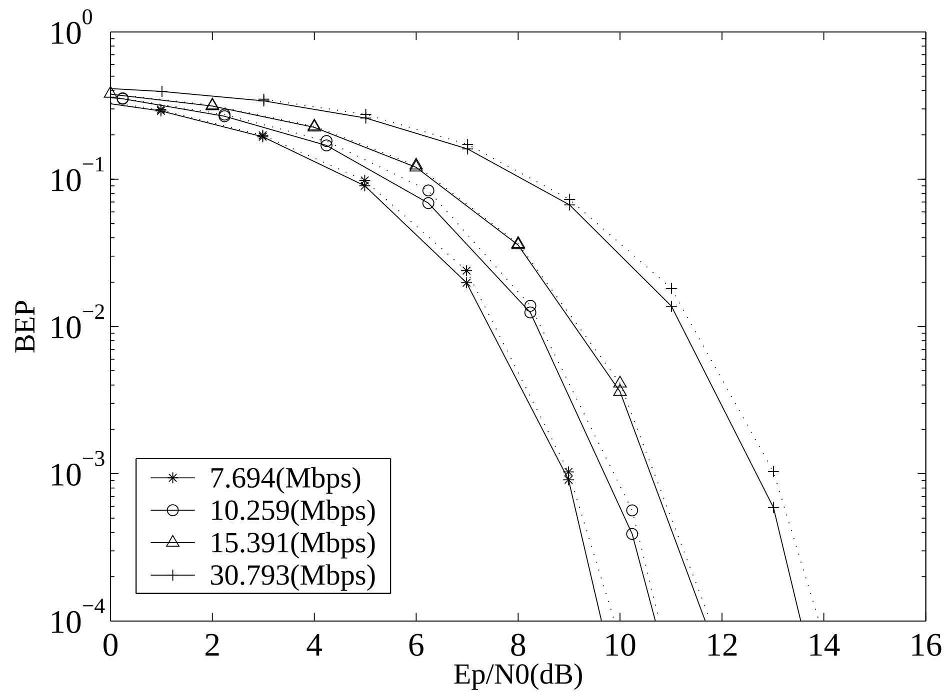

Figure 7.9: Simulated and calculated BEP versus UWB pulse energy of the quantized digital SFS TR receiver with 3-bit resolution for the channel IR inside engine compartment.

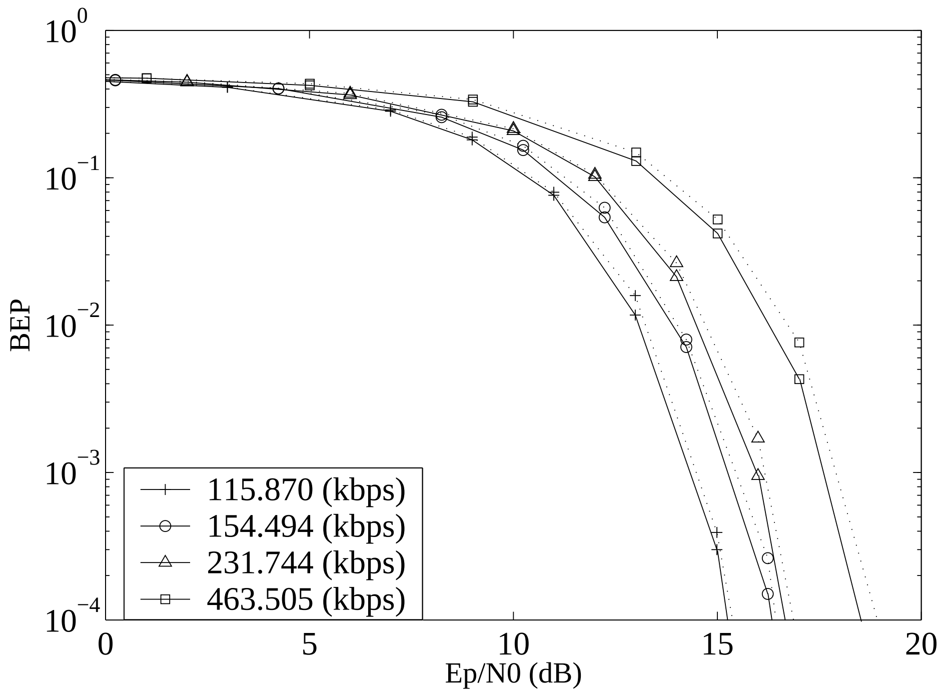

Figure 7.10: Simulated and calculated BEP versus UWB pulse energy of the quantized digital SFS TR receiver with 3-bit resolution for 802.15.3a CM3.

CHAPTER 8
SUMMARY AND FUTURE WORK

The IR-UWB technique is considered a promising way to construct intra-vehicle wireless sensor network in a commercial automotive for the purpose of reducing vehicle weight and simplifying vehicle architecture design. Knowledge of UWB propagation in the intra-vehicle environment is needed before any intra-vehicle UWB communication system can be implemented. In the literature, extensive channel measurement campaigns have been conducted for indoor and outdoor environments by many UWB researchers. And their channel modeling contributions have been summarized in IEEE 802.15.3a as well as 802.15.4a channel modeling reports. However, very few researchers have performed and reported the UWB channel characteristics within commercial vehicle environments. Due to the lack of UWB channel investigation in such an environment, this dissertation reports the effort to collect the UWB propagation data and to characterize the channels. Channel measurement has been conducted either beneath the chassis or inside the engine compartments of two commercial vehicles because some sensors are located in such places.

CLEAN algorithm based deconvolution technique has been employed to withdraw the channel impulse responses from the measured profiles. It is observed that clusters exist in the profiles from the engine compartment but there is no clustering phenomenon in the profiles from beneath the chassis. Consequently, this dissertation describes the UWB channels in these two cases with different models. A modified S-V channel model is used for the engine compartment case to count for the clustering phenomenon and a tapped-delay-line model is employed for the chassis case. Further statistical analysis has been applied to the impulse responses to extract the model parameters and their values have been compared with those from the indoor or outdoor environments provided by other researchers.

This dissertation also investigates the influences of the vehicle movement on the UWB channel characteristics beneath the chassis. Same set of measurements have been repeated while the vehicle is stationary in a parking building then while it is running around Oakland University campus. This dissertation reports that the movement of the vehicle does not bring much change to the UWB propagation under the chassis based on the comparison between the measured data from the running case and from the stationary case. This will simplify the design of UWB communication system working under the chassis because no special adjustments are needed for the car in movement.

Furthermore, to reduce the heavy task of identifying clusters in huge amount of clustering UWB impulse responses and assure consistent results. An automatic cluster identification algorithm has been developed and implemented in this dissertation. Just like the visual cluster identification process, this algorithm completes the task in two steps. The first step is to identify those non-overlapping clusters by checking the inter-cluster time intervals. Then the resulting clusters will be further processed in the second step to identify those sudden increases in path amplitudes to recognize the over-lapping clusters. Combination of these two steps produces similar results as those from manual identification.

Finally, the effort to design a UWB receiver which can work in the intra-vehicle environment has been reported. Based on the fact that the intra-vehicle sensor network is a low-data-rate application, this dissertation develops a digital version of the slightly frequency shifted TR receiver to provide flexibility, to take advantage of widely available DSP circuits and algorithms, and to reduce the size of the UWB receiver. In the SFS TR signaling scheme, the data signal are transmitted together with a reference signal whose frequency is slightly shifted. At the receiver, the reference signal is correlated with the data signal to decide the information bit. The frequency shift is slight so that it is within the coherence frequency of the channel. In the structure of the digital receiver supporting this signaling scheme, ADCs are added to conduct the sampling and quantization of the received signal before correlation is performed. This dissertation first derived the closed-form performance expression for such a receiver assuming the ADCs are full-resolution, that is, the case when the received signal is discrete in time after being sampled. Simulations have been run for this discrete time full-resolution receiver based on the randomly selected impulse responses not only from the intra-vehicle environment but also from 802.15.3a CM3 and 802.15.4a office models. Analysis shows that the theoretical calculation fits the simulation results very well for all mentioned channels. Then this dissertation continued to derive the performance expression for the receiver with ADCs of very limited resolution. The ADCs only provide low-bit resolution when quantizing the discrete time signal samples because the receiver will be too expensive to implement if high sampling rate high resolution low power ADCs are required. Quantization theorem based digitization process has been used in the detail derivation of the quantized digital SFS TR receiver's BEP expression. Consistent results from simulations and theoretical calculations validated the accuracy of the closed-form BEP representation for such a discrete time and quantized SFS TR receiver.

Following the research reported in this dissertation, if more work will be done in the field of intra-vehicle UWB channel characterization, frequency selectivity for UWB propagation should be considered. As mentioned in Chapter 3, because of the frequency selectivity in the reflection, diffraction or scattering processes, MPCs in UWB impulse responses experience different distortions. Such kind of distortion will be a good topic for future research. In addition, for the signal detection, this dissertation only reported a digital UWB SFS TR receiver with uniform quantizer. In the future, a quantizer with non-uniform stepsize should be considered and compared with the current uniform one.

APPENDIX A

DERIVATIONS FOR THE CALCULATION OF DISCRETE TIME FULL-RESOLUTION SFS TR RECEIVER BEP

This appendix gives the detail derivation steps for $\sum_{n=0}^{N-1} x^2(n)c^2(n)$ of equation (7.24) and $\sum_{n=0}^{N-1} x^2(n)c(n)$ of equation (7.25) in Section 7.3 of Chapter 7.

$$
\begin{aligned}
\sum_{n=0}^{N-1} x^2(n)c^2(n) &= E_s \sum_{l=0}^{L-1} \alpha_l^2 \sum_{n=0}^{N-1} [\sum_{k=0}^{N_f-1} p^2(n-kF-D_l)][\sqrt{\frac{1}{2}} + c(n-D_l)]^2 c^2(n) \\
&\approx E_s \sum_{l=0}^{L-1} \alpha_l^2 \sum_{n=0}^{N-1} \sum_{k=0}^{N_f-1} p^2(n-kF-D_l)[\sqrt{\frac{1}{2}} + c(kF)]^2 c^2(kF+D_l) \\
&= \frac{E_s}{t_s} \sum_{l=0}^{L-1} \alpha_l^2 \sum_{k=0}^{N_f-1} [\sqrt{\frac{1}{2}} + c(kF)]^2 c^2(kF+D_l) \sum_{n=0}^{N-1} p^2(n-kF-D_l) t_s \\
&= \frac{E_s}{t_s} \sum_{l=0}^{L-1} \alpha_l^2 \sum_{k=0}^{N_f-1} [\sqrt{\frac{1}{2}} + c(kF)]^2 c^2(kF+D_l) \frac{1}{N_f} \\
&= \frac{E_s}{N_f t_s} \sum_{l=0}^{L-1} \alpha_l^2 \sum_{k=0}^{N_f-1} [\sqrt{\frac{1}{2}} + c(kF)]^2 c^2(kF+D_l) \\
&\approx \frac{E_s}{t_s} \frac{1}{N} \sum_{l=0}^{L-1} \alpha_l^2 \sum_{n=0}^{N-1} [\sqrt{\frac{1}{2}} + c(n)]^2 c^2(n+D_l) \\
&= \frac{E_s}{t_s} \frac{1}{N} \sum_{l=0}^{L-1} \alpha_l^2 \sum_{n=0}^{N-1} [\frac{1}{2} c^2(n+D_l) + \sqrt{2} c(n) c^2(n+D_l) + c^2(n) c^2(n+D_l)] \\
&= \frac{E_s}{t_s} \frac{1}{N} \sum_{l=0}^{L-1} \alpha_l^2 [\frac{N}{4} + \sum_{n=0}^{N-1} c^2(n) c^2(n+D_l)] \\
&= \frac{E_s}{t_s} \frac{1}{N} \sum_{l=0}^{L-1} \alpha_l^2 [\frac{N}{4} + \frac{N}{4} + \frac{1}{4} \sum_{n=0}^{N-1} c(2n) c(2n+2D_l)] \\
&= \frac{E_s}{t_s} \frac{1}{N} \sum_{l=0}^{L-1} \alpha_l^2 [\frac{N}{2} + \frac{1}{8} \sum_{n=0}^{N-1} c(2D_l)] \\
&= \frac{E_s}{t_s} \sum_{l=0}^{L-1} \alpha_l^2 [\frac{3}{8} + \frac{1}{4} c^2(D_l)]. \qquad \text{(A.1)}
\end{aligned}
$$

The first approximation in the above derivation is established because in time domain the discrete UWB pulse $p(n)$ is so narrow compared with the discrete cosine signal $c(n)$ so that their product can be treated as the process of sampling $c(n)$ at the time delay $kF + D_l$. The second approximation is derived by the application of Riemann Integral based on the assumption that N_f is relatively large, e.g 20 [95].

Following similar process, we also get

$$\sum_{n=0}^{N-1} x^2(n)c(n) = \sum_{n=0}^{N-1} [\sum_{l=0}^{L-1} \alpha_l s(n-D_l)]^2 c(n)$$

$$= \sum_{n=0}^{N-1} [\sum_{l=0}^{L-1} \sum_{m=0}^{L-1} \alpha_l s(n-D_l) \alpha_m s(n-D_m)] c(n)$$

$$= \sum_{l=0}^{L-1} \sum_{m=0}^{L-1} \alpha_l \alpha_m [\sum_{n=0}^{N-1} s(n-D_l) s(n-D_m) c(n)]$$

$$= \sum_{l=0}^{L-1} \sum_{m=0}^{L-1} \alpha_l \alpha_m \sum_{n=0}^{N-1} c(n) u(n-D_l) u(n-D_m)$$

$$[\sqrt{\frac{E_s}{2}} + \sqrt{E_s} c(n-D_l)][\sqrt{\frac{E_s}{2}} + \sqrt{E_s} c(n-D_m)]$$

$$= E_s \sum_{l=0}^{L-1} \sum_{m=0}^{L-1} \alpha_l \alpha_m \sum_{n=0}^{N-1} [\sum_{k=0}^{N_f-1} p(n-kF-D_l)][\sum_{i=0}^{N_f-1} p(n-iF-D_m)]$$

$$[\sqrt{\frac{1}{2}} + c(n-D_l)][\sqrt{\frac{1}{2}} + c(n-D_m)] c(n)$$

$$= E_s \sum_{l=0}^{L-1} \alpha_l^2 \sum_{n=0}^{N-1} [\sum_{k=0}^{N_f-1} p^2(n-kF-D_l)][\sqrt{\frac{1}{2}} + c(n-D_l)]^2 c(n)$$

$$\approx E_s \sum_{l=0}^{L-1} \alpha_l^2 \sum_{n=0}^{N-1} \sum_{k=0}^{N_f-1} p^2(n-kF-D_l)[\sqrt{\frac{1}{2}} + c(kF)]^2 c(kF+D_l)$$

$$= \frac{E_s}{t_s} \sum_{l=0}^{L-1} \alpha_l^2 \sum_{k=0}^{N_f-1} [\sqrt{\frac{1}{2}} + c(kF)]^2 c(kF+D_l) \sum_{n=0}^{N-1} p^2(n-kF-D_l) t_s$$

$$= \frac{E_s}{t_s} \sum_{l=0}^{L-1} \alpha_l^2 \sum_{k=0}^{N_f-1} [\sqrt{\frac{1}{2}} + c(kF)]^2 c(kF+D_l) \frac{1}{N_f}$$

$$= \frac{E_s}{N_f t_s} \sum_{l=0}^{L-1} \alpha_l^2 \sum_{k=0}^{N_f-1} [\sqrt{\frac{1}{2}} + c(kF)]^2 c(kF+D_l)$$

$$
\begin{aligned}
&\approx \frac{E_s}{t_s}\frac{1}{N}\sum_{l=0}^{L-1}\alpha_l^2\sum_{n=0}^{N-1}[\sqrt{\frac{1}{2}}+c(n)]^2 c(n+D_l) \\
&= \frac{E_s}{t_s}\frac{1}{N}\sum_{l=0}^{L-1}\alpha_l^2\sum_{n=0}^{N-1}[\frac{1}{2}c(n+D_l)+\sqrt{2}c(n)c(n+D_l)+c^2(n)c(n+D_l)] \\
&= \frac{E_s}{t_s}\frac{1}{N}\sum_{l=0}^{L-1}\alpha_l^2[\sqrt{2}\sum_{n=0}^{N-1}c(n)c(n+D_l)] = \frac{1}{\sqrt{2}}\frac{E_s}{t_s}\sum_{l=0}^{L-1}\alpha_l^2 c(D_l). \qquad \text{(A.2)}
\end{aligned}
$$

APPENDIX B

JOINT MOMENTS OF RECEIVED SIGNAL AND QUANTIZATION ERROR

This appendix describes the detail steps to derive $E[r^2(n)e_q^2(n)]$, $E[r(n)e_q^3(n)]$ and $E[r^3(n)e_q(n)]$, the three joint moments of the discrete time full-resolution signal $r(n)$ and the quantization error $e_q(n)$, for equations (7.42)-(7.44) in Section 7.4 of Chapter 7.

As we know, because

$$\phi_{r_q}^{(n)}(\omega)|_{\omega=0} = j^n E[r_q^n], \tag{B.1}$$

We have

$$E[r_q^4(n)] = \phi_{r_q}^{(4)}(\omega)|_{\omega=0}. \tag{B.2}$$

For convenience, let $A = \omega - \frac{2k\pi}{\Delta}$ and $B = \frac{\Delta\omega}{2} - k\pi$, equation (7.41) can be re-written as below

$$\phi_{r_q}(\omega) = \sum_{k=-\infty}^{\infty} \phi_r(A)\frac{\sin B}{B}. \tag{B.3}$$

Then, the first order derivative of $\phi_{r_q}(\omega)$ is

$$\phi_{r_q}^{'}(\omega) = \sum_{k=-\infty}^{\infty} \frac{\phi_r^{'}(A)B\sin B + \phi_r(A)\frac{\Delta}{2}(B\cos B - \sin B)}{B^2}. \tag{B.4}$$

Based on equation (B.4), the second order derivative of $\phi_{r_q}(\omega)$ is

$$\begin{aligned} \phi_{r_q}^{''}(\omega) = & \sum_{k=-\infty}^{\infty} \frac{\phi_r^{''}(A)B^2\sin B}{B^3} \\ & - \sum_{k=-\infty}^{\infty} \frac{\phi_r(A)\frac{\Delta^2}{2}(\frac{B^2\sin B}{2} + B\cos B - \sin B)}{B^3} \\ & + \sum_{k=-\infty}^{\infty} \frac{\phi_r^{'}(A)\Delta B(B\cos B - \sin B)}{B^3}. \end{aligned} \tag{B.5}$$

Again, based on equation (B.5), we can get the third order derivative of $\phi_{r_q}(\omega)$ as

$$
\begin{aligned}
\phi_{r_q}^{(3)}(\omega) = & \sum_{k=-\infty}^{\infty} \frac{\phi_r^{(3)}(A) B^3 \sin B}{B^4} \\
& + \sum_{k=-\infty}^{\infty} \frac{\phi_r''(A) \frac{3\Delta}{2} B^2 (B \cos B - \sin B)}{B^4} \\
& + \sum_{k=-\infty}^{\infty} \frac{\phi_r'(A) \frac{3\Delta^2}{2} B (\sin B - B \cos B - \frac{B^2}{2} \sin B)}{B^4} \\
& - \sum_{k=-\infty}^{\infty} \frac{\phi_r(A) \frac{3\Delta^3}{4} (\frac{B^3 \cos B}{6} - \frac{B^2 \sin B}{2} - B \cos B + \sin B)}{B^4}.
\end{aligned} \tag{B.6}
$$

Finally, taking advantage of the result in equation (B.6), we can derive the fourth order derivative of $\phi_{r_q}(\omega)$ as

$$
\begin{aligned}
\phi_{r_q}^{(4)}(\omega) = & \sum_{k=-\infty}^{\infty} \frac{\phi_r^{(4)}(A) B^4 \sin B}{B^5} \\
& + \sum_{k=-\infty}^{\infty} \frac{\phi_r^{(3)}(A) 2\Delta B^3 (B \cos B - \sin B)}{B^5} \\
& + \sum_{k=-\infty}^{\infty} \frac{\phi_r''(A) 3\Delta^2 B^2 (\sin B - B \cos B - \frac{B^2}{2} \sin B)}{B^5} \\
& - \sum_{k=-\infty}^{\infty} \frac{\phi_r'(A) 3\Delta^3 B (\frac{B^3 \cos B}{2} - \frac{B^2 \sin B}{2} - B \cos B + \sin B)}{B^5} \\
& + \sum_{k=-\infty}^{\infty} \frac{\phi_r(A) \frac{3\Delta^4}{2} (\frac{B^4}{24} \sin B + \frac{B^3}{6} \cos B - \frac{B^2}{2} \sin B)}{B^5} \\
& + \sum_{k=-\infty}^{\infty} \frac{\phi_r(A) \frac{3\Delta^4}{2} (-B \cos B + \sin B)}{B^5}.
\end{aligned} \tag{B.7}
$$

Hence, we have

$$E[r_q^4] = \phi_{rq}^{(4)}(\omega)|_{\omega=0} = \sum_{k=-\infty}^{\infty} [\phi_r^{(4)}(\frac{-2k\pi}{\Delta})\frac{\sin k\pi}{k\pi}$$
$$+ \phi_r^{(3)}(\frac{-2k\pi}{\Delta})\frac{2\Delta(\sin k\pi - k\pi\cos k\pi)}{k^2\pi^2}$$
$$+ \phi_r''(\frac{-2k\pi}{\Delta})\frac{3\Delta^2(\sin k\pi - k\pi\cos k\pi - \frac{k^2\pi^2\sin k\pi}{2})}{k^3\pi^3}$$
$$+ \phi_r'(\frac{-2k\pi}{\Delta})\frac{\Delta^3(\frac{k^3\pi^3\cos k\pi}{2} - \frac{3k^2\pi^2\sin k\pi + 6k\pi\cos k\pi - 6\sin k\pi}{2})}{k^4\pi^4}$$
$$+ \phi_r(\frac{-2k\pi}{\Delta})\frac{\Delta^4(\frac{k^4\pi^4\sin k\pi}{16} + \frac{k^3\pi^3\cos k\pi}{4} - \frac{3k^2\pi^2\sin k\pi}{4})}{k^5\pi^5}$$
$$+ \phi_r(\frac{-2k\pi}{\Delta})\frac{\Delta^4(-\frac{3k\pi\cos k\pi}{2} + \frac{3\sin k\pi}{2})}{k^5\pi^5}]. \tag{B.8}$$

By comparing equation (B.8) with equation (7.39), it is obvious that we will get the following equations.

$$4E[r^3(n)e_q(n)] = \sum_{k=-\infty}^{\infty} \phi_r^{(3)}(\frac{-2k\pi}{\Delta})2\Delta\frac{\sin k\pi - k\pi\cos k\pi}{k^2\pi^2}, \tag{B.9}$$

$$6E[r^2(n)e_q^2(n)] = \sum_{k=-\infty}^{\infty} \phi_r''(\frac{-2k\pi}{\Delta})3\Delta^2\frac{\sin k\pi - k\pi\cos k\pi}{k^3\pi^3}$$
$$- \sum_{k=-\infty}^{\infty} \phi_r''(\frac{-2k\pi}{\Delta})\frac{3\Delta^2}{2}\frac{k^2\pi^2\sin k\pi}{k^3\pi^3}, \tag{B.10}$$

$$4E[r(n)e_q^3(n)] = \sum_{k=-\infty}^{\infty} \phi_r'(\frac{-2k\pi}{\Delta})\Delta^3\frac{k\pi\cos k\pi - 3\sin k\pi}{2k^2\pi^2}$$
$$- \sum_{k=-\infty}^{\infty} \phi_r'(\frac{-2k\pi}{\Delta})\Delta^3\frac{6k\pi\cos k\pi - 6\sin k\pi}{2k^4\pi^4}. \tag{B.11}$$

By use of L'Hospital's Rule, we can get

$$E[r^3(n)e_q(n)] = \frac{\Delta}{2}\sum_{k=-\infty}^{\infty}\phi_r^{(3)}(\frac{-2k\pi}{\Delta})\frac{\sin k\pi}{k^2\pi^2} - \frac{\Delta}{2}\sum_{k=-\infty}^{\infty}\phi_r^{(3)}(\frac{-2k\pi}{\Delta})\frac{\cos k\pi}{k\pi}$$

$$= -\frac{\Delta}{2}\sum_{k\neq 0}\phi_r^{(3)}(\frac{-2k\pi}{\Delta})\frac{(-1)^k}{k\pi}, \tag{B.12}$$

$$E[r^2(n)e_q^2(n)] = \Delta^2\sum_{k=-\infty}^{\infty}\phi_r''(\frac{-2k\pi}{\Delta})\frac{\sin k\pi}{2k^3\pi^3} - \Delta^2\sum_{k=-\infty}^{\infty}\phi_r''(\frac{-2k\pi}{\Delta})\frac{\cos k\pi}{2k^2\pi^2}$$

$$- \Delta^2\sum_{k=-\infty}^{\infty}\phi_r''(\frac{-2k\pi}{\Delta})\frac{\sin k\pi}{4k\pi}$$

$$= \frac{\Delta^2(x^2(n)+\sigma^2)}{12} - \sum_{k=1}^{\infty}\phi_r''(\frac{-2k\pi}{\Delta})\frac{(-1)^k\Delta^2}{2k^2\pi^2}, \tag{B.13}$$

$$E[r(n)e_q^3(n)] = \Delta^3\sum_{k=-\infty}^{\infty}\phi_r'(\frac{-2k\pi}{\Delta})\frac{\cos k\pi}{8k\pi} - \Delta^3\sum_{k=-\infty}^{\infty}\phi_r'(\frac{-2k\pi}{\Delta})\frac{3\sin k\pi}{8k^2\pi^2}$$

$$- \Delta^3\sum_{k=-\infty}^{\infty}\phi_r'(\frac{-2k\pi}{\Delta})\frac{3\cos k\pi}{4k^3\pi^3} + \Delta^3\sum_{k=-\infty}^{\infty}\phi_r'(\frac{-2k\pi}{\Delta})\frac{3\sin k\pi}{4k^4\pi^4}$$

$$= \frac{\Delta^3}{8}\sum_{k=1}^{\infty}\phi_r'(\frac{-2k\pi}{\Delta})\frac{(-1)^k}{k\pi} - \frac{3\Delta^3}{4}\sum_{k=1}^{\infty}\phi_r'(\frac{-2k\pi}{\Delta})\frac{(-1)^k}{k^3\pi^3}, \tag{B.14}$$

in which the first, second and third order derivatives of $\phi_r(\omega)$ respectively are

$$\phi_r'(\omega) = [jx(n) - \sigma^2\omega]e^{jx(n)\omega - \frac{\sigma^2\omega^2}{2}}, \tag{B.15}$$

$$\phi_r''(\omega) = [-x^2(n) + \sigma^4\omega^2 - \sigma^2 - 2jx(n)\sigma^2\omega]e^{jx(n)\omega - \frac{\sigma^2\omega^2}{2}}, \tag{B.16}$$

$$\phi_r^{(3)}(\omega) = [3\sigma^4\omega - \sigma^6\omega^3 + 3\sigma^2x^2(n)\omega] + j[3\sigma^4x(n)\omega^2 - 3\sigma^2x(n) - x^3(n)]e^{jx(n)\omega - \frac{\sigma^2\omega^2}{2}}. \tag{B.17}$$

REFERENCES

[1] T. Costlow, "Sensing significant growth," *Society of Automotive Engineers (SAE) Automotive Engineering International*, pp. 74–78, May 2004.

[2] W. J. Fleming, "Overview of automotive sensors," *IEEE Sensors Journal*, vol. 1, no. 4, pp. 296–308, Dec. 2001.

[3] G. Leen and D. Hefferna, "Vehicles without wires," *Computing and Control Engineering Journal*, pp. 205–211, Oct. 2001.

[4] Hsin-Mu Tsai, W. Viriyasitavat, O. K. Tonguz, C. Saraydar, T. Talty, and A. Macdonald, "Feasibility of In-car Wireless Sensor Networks: A Statistical Evaluation," in *4th Annual IEEE Communications Society Conference on Sensor, Mesh and Ad Hoc Communications and Networks 2007 (SECON '07)* , Jun. 2007, pp. 101–111.

[5] G. Leen, D. Heffernan, and A. Dunne, "Digital networks in the automotive vehicle," *Computing & Control Engineering Journal* , vol. 10, no. 6, pp. 205–211, Dec. 1999.

[6] T. ElBatt, C. Saraydar, M. Ames, and T. Talty, "Potential for intra-vehicle wireless automotive sensor networks," in *2006 IEEE Sarnoff Symposium*, Mar. 2006, pp. 71–78.

[7] J. R. Foerster, "The Effects of Multipath Interference on the Performance of UWB Systems in an Indoor Wireless Channel," in *IEEE VTS 53rd*, vol. 2, 2001, pp. 1176–1180.

[8] A. H. Muqaibel, "Characterization of ultra wideband communication channels," Ph.D. dissertation, The Bradley Department of Electrical and Computer Engineering, Virginia Polytechnic Institute and State University, 2003.

[9] R. J.-M. Cramer, R.A. Scholtz, and M.Z. Win, "On the analysis of UWB communication channels," in *IEEE Military Communications Conference 1999 (MILCOM 1999)*, vol. 2, 1999, pp. 1191–1195.

[10] K. Mandke, H. Nam, L. Yerramneni, and C. Zuniga, "The evolution of UWB and IEEE 802.15.3a for very high data rate WPAN," The University of Texas at Austin, Tech. Rep. EE 381K-11 Wireless Communications, May 2003. [Online]. Available: http://users.ece.utexas.edu/~wireless/EE381K11_Spring03/projects/10.3.%pdf

[11] "First report and order 02-48," Federal Communications Commission, Feb. 2002.

[12] A. F. Molisch, J. R. Foerster, and M. Pendergrass, "Channel models for ultrawideband personal area networks," *IEEE Wireless Communications*, vol. 10, no. 6, pp. 14–21, Dec. 2003.

[13] R. A. Scholtz and M. Z. Win, "Impulse radio," in *IEPIMRC'97- Helsinki*, 1997, pp. 245–267.

[14] M. Z. Win and R. A. Scholtz, "Impulse radio : How it works," *IEEE Communications Letters*, vol. 2, no. 2, pp. 36–38, Feb. 1998.

[15] G. Schiavone, P. Wahid, R. Palaniappan, J. Tracy, E. V. Doorn, and B. Lonske, "Outdoor propagation analysis of ultra wide band signals," in *Antennas and Propagation Society International Symposium*, vol. 2, Jun. 2003, pp. 999–1002.

[16] M. Z. Win, F. Ramirez-Mireles, R. A. Scholtz, and M. A. Barnes, "Ultra-wide bandwidth (UWB) signal propagation for outdoor wireless communications," in *1997 IEEE 47th Vehicular Technology Conference*, vol. 1, May 1997, pp. 251–255.

[17] M. Z. Win, R. A. Scholtz, and M. A. Barnes, "Ultra-wide bandwidth signal propagation for indoor wireless communications," in *1997 IEEE International Conference on Communications*, vol. 1, Jun. 1997, pp. 56–60.

[18] J. Choi, N.-G Kang, Y.-S Sung, and S.-C Kim, "Empirical ultra wide band channel model for short range outdoor environments," in *IEEE 65th Vehicular Technology Conference*, Apr. 2007, pp. 1579–1583.

[19] R. J.-M. Cramer, R. A. Scholtz, and M. Z. Win, "Evaluation of an ultra-wide-band propagation channel," *IEEE Transactions on Antennas and Propagation*, vol. 50, pp. 561–570, May 2002.

[20] Q. Spencer, M. Rice, B. Jeffs, and M. Jensen, "A statistical model for angle of arrival in indoor multipath propagation," in *IEEE 47th Vehicular Technology Conference*, vol. 3, May 1997, pp. 1415–1419.

[21] J. R. Foerster et al., "Channel modeling sub-committee report final," IEEE P802.15-02/490r1-SG3a, Feb. 2003.

[22] A. F. Molisch, K. Balakrishnan, D. Cassioli, C.-C Chong, S. Emami, A. Fort, J. Karedal, J. Kunisch, H. Schantz, U. Schuster, and K. Siwiak, "IEEE 802.15.4a channel model - final report," IEEE 802.15-04-0662-00-004a, Nov. 2004.

[23] P. C. Richardson, W. Xiang, and W. Stark, "Modeling of ultra-wideband channels within vehicles," *IEEE Journal on Selected Areas in Communications*, vol. 24, pp. 906–912, Apr. 2006.

[24] M. Z. Win and R. A. Scholtz, "On the energy capture of ultrawide bandwidth signals in dense multipath environments," *IEEE Communications Letters*, vol. 2, no. 9, pp. 245–247, Sep. 1998.

[25] M. Z. Win, R. A. Scholtz, "On the robustness of ultra-wide bandwidth signals in dense multipath environments," *IEEE Communications Letters*, vol. 2, pp. 51–53, Feb. 1998.

[26] M. A. Rahman, S. Sasaki, J. Zhou, and H. Kikuchi, "On rake reception of UltraWideband signals over multipath channels from energy capture perspective," *IEICE Transactions on Fundamentals*, vol. E88-A, no. 9, pp. 2339–2349, Sep. 2005.

[27] M. Z. Win, G. Chrisikos, and N. R. Sollenberger, "Impact of spreading bandwidth and diversity order on the error probability performance of RAKE reception in dense multipath channels," in *IEEE Wireless Communications and Networking Conference*, vol. 3, Sep. 1999, pp. 1558–1562.

[28] ——, "Performance of RAKE reception in dense multipath channels: implications of spreading bandwidth and selection diversity order," *IEEE Journal on Selected Areas in Communications*, vol. 18, no. 18, pp. 1516–1525, Aug. 2000.

[29] R. A. Scholtz, "The origins of spread-spectrum communications," *IEEE Transactions on Communications*, vol. 30, no. 5, pp. 822– 854, May 1982.

[30] R. Hoctor and H. Tomlinson, "Delay-hopped transmitted-reference RF communications," in *2002 IEEE Conference on Ultra Wideband Systems and Technologies*, Aug. 2002, pp. 265–269.

[31] N. van Stralen, A. Dentinger, K. Welles II, R. Gaus Jr., R. Hoctor, and H. Tomlinson, "Delay hopped transmitted reference experimental results," in *2002 IEEE Conference on Ultra Wideband Systems and Technologies*, Aug. 2002, pp. 93– 98.

[32] J. Choi and W. Stark, "Performance of ultra-wideband communications with suboptimal receivers in multipath channels," *IEEE Journal on Selected Areas in Communications*, vol. 20, no. 9, pp. 1754–1766, Sep. 2002.

[33] Y. Chao and R. A. Scholtz, "Optimal and suboptimal receivers for ultra-wideband transmitted reference systems," in *IEEE Global Telecommunications Conference 2003 (GLOBECOM 2003)*, vol. 2, Dec. 2003, pp. 759–763.

[34] ——, "Novel UWB transmitted reference schemes," in *Thirty-Eighth Asilomar Conference on Signals, Systems and Computers*, vol. 1, Nov. 2004, pp. 652–656.

[35] ——, "Ultra-wideband transmitted reference systems," *IEEE Transactions on Vehicular Technology*, vol. 54, no. 5, pp. 1556–1569, Sep. 2005.

[36] T. Q. S. Quek and M. Z. Win, "Analysis of UWB transmitted-reference communication systems in dense multipath channels," *IEEE Journal on Selected Areas in Communications*, vol. 23, no. 9, pp. 1863–1874, Sep. 2005.

[37] D. L. Goeckel and Q. Zhang, "Slightly frequency-shifted reference ultra-wideband (UWB) radio: TR-UWB without the delay element," in *IEEE Military Communications Conference 2005 (MILCOM 2005)*, vol. 5, Oct. 2005, pp. 3029–3035.

[38] ——, "Slightly frequency-shifted reference ultra-wideband (UWB) radio," *IEEE Transactions on Communications*, vol. 55, no. 3, pp. 508–519, Mar. 2007.

[39] Q. Zhang, "Slightly frequency-shifted reference ultra-wideband radio," Ph.D. dissertation, Electrical and Computer Engineering, the University of Massachusetts Amherst, 2006.

[40] W. Niu, J. Li, and T. Talty, "Intra-vehicle UWB communication testbed," in *IEEE Military Communications Conference 2007 (MILCOM 2007)*, Oct. 2007.

[41] J. R. Foerster, M. Pendergrass, and A. F. Molisch, "A channel model for Ultra Wideband indoor communication," Mitsubishi Electric Research Laboratories, Tech. Rep. TR2004-074, Oct. 2003. [Online]. Available: http://www.merl.com/publications/TR2004-074/

[42] D. Cassioli, M. Z. Win, and A. F. Molisch, "The ultra-wide bandwidth indoor channel: from statistical model to simulations," *IEEE Journal on Selected Areas in Communications*, vol. 20, no. 6, pp. 1247–1257, Aug. 2002.

[43] M. Z. Win and R. A. Scholtz , "Characterization of ultra-wide bandwidth wireless indoor channels: a communication-theoretic view," *IEEE Journal on Selected Areas in Communications*, vol. 20, no. 9, pp. 1613–1627, Dec. 2002.

[44] D. Cassioli, M. Win, and A. Molisch, "A Statistical Model for the UWB Indoor Channel," in *IEEE Conference on Vehicular Technology 53rd VTC*, vol. 2, 2001, pp. 1159–1163.

[45] S. M. Yano, "Investigating the ultra-wideband indoor wireless channel," in *IEEE 55th Vehicular Technology Conference 2002 (VTC Spring 2002)*, vol. 3, 2002, pp. 1200–1204.

[46] W. Ciccognani, A. Durantini, and D. Cassioli, "Time domain propagation measurements of the UWB indoor channel using PN-sequence in the FCC-compliant band 3.6-6 GHz," *IEEE Transactions on Antennas and Propagation*, vol. 53, no. 4, pp. 1542–1549, Apr. 2005.

[47] A. Muqaibel, A. Safaai-Jazi, B. Woerner, and S. M. Riad, "Ultrawideband through-the-wall propagation," in *The 2002 45th Midwest Symposium on Circuits and Systems (MWSCAS-2002)*, vol. 3, Aug. 2002, pp. III–605–608.

[48] M. D. Renzo, F. Graziosi, R. Minutolo, M. Montanari, and F. Santucci, "The ultra-wide bandwidth outdoor channel: from measurement campaign to statistical modelling," *Mobile Networks and Applications*, vol. 11, no. 4, pp. 451–467, Aug. 2006.

[49] C.-C. Chong and S. K. Yong, “A Generic Statistical-Based UWB Channel Model for High-Rise Apartments,” *IEEE Transactions on Antennas and Propagation*, vol. 53, no. 8, pp. 2389–2399, Aug. 2005.

[50] J. Keignart and N. Daniele, “Subnanosecond UWB channel sounding in frequency and temporal domain,” in *2002 IEEE Conference on Ultra Wideband Systems and Technologies. Digest of Papers*, 2002, pp. 25–30.

[51] P. Pagani and P. Pajusco, “Characterization and Modeling of Temporal Variations on an Ultrawideband Radio Link,” *IEEE Transactions on Antennas and Propagation*, vol. 54, no. 11, pp. 3198–3206, Nov. 2006.

[52] T.S. Rappaport, *Wireless Communications, Principles & Practice.* Prentice Hall Inc., 1996.

[53] C. R. Anderson, T. S. Rappaport, K. Bae, A. Verstak, N. Ramakrishnan, W.Tranter, C. Shaffer, and L. Watson, “In-Building wideband multipath characteristics at 2.5 and 60 GHz,” in *IEEE 56th Vehicula Technology Conference*, vol. 1, 2002, pp. 97–101.

[54] G. D. Durgin and T. S. Rappaport, “Theory of multipath shape factors for small-Scale fading wireless channels,” *IEEE Transactions on Antennas an Propagation*, vol. 48, no. 5, pp. 682–693, May 2000.

[55] A. M. Hayar and G. M. Vitetta, “Channel Models for Ultra-Wideband Communications: an Overview,” in *14th IST Mobile & Wireless Communications Summit*, Jun. 2005.

[56] J. Choi and W. Stark, “A generic statistical-based UWB channel model for high-rise apartments,” *IEEE Journal on Selected Areas in Communications*, vol. 53, no. 8, pp. 2389– 2399, Aug. 2005.

[57] A. Saleh, and R. A. Valenzuela, “A statistical model for indoor multipath propagation,” *IEEE Journal on Selected Areas in Communications*, vol. 5, pp. 128–137, Feb. 1987.

[58] J. A. Högbom, “Aperture synthesis with a nonrectangular distribution of interferometer baselines,” *Astronomy and Astrophysics*, vol. 15, pp. 417–427, 1974.

[59] R. H. T. Bates and M. J. McDonnell, *Image Restoration and Reconstruction.* U.K.: Clarendon Press, 1989.

[60] R. G. Vaughan and N. L. Scott, “Super-resolution of pulsed multipath channels for delay spread characterization,” *IEEE Transactions on Communications*, vol. 47, no. 3, pp. 343–347, Mar. 1999.

[61] J. G. Proakis, *Digital Communications 5TH Edition.* New York: McGraw-Hill, 2007.

[62] H. Hashemi, "The indoor radio propagation channel," in *Proceedings of the IEEE*, vol. 81, Jul. 1993, pp. 943–968.

[63] ——, "Impulse response modeling of indoor propagation channels," *IEEE Journal on Selected Areas in Communications*, vol. 11, no. 7, pp. 967–978, Sep. 1993.

[64] A. F. Molisch, "Ultrawideband propagatiton channels-theory, measurement, and modeling," *IEEE Transactions on Vehicular Technology*, vol. 54, no. 5, pp. 1528–1545, Sep. 2005.

[65] R. M. Buehrer, A. Safaai-Jazi, @. Davis, and D. Sweeney, "Ultra Wideband Propagation Measurements and Modeling," Virginia Tech, Tech. Rep. Final Report to DARPA NETEX Program, Jan. 2004. [Online]. Available: http://www.mprg.org/people/buehrer/ultra/pdfs/Chapter1_ExecutiveSummar%y.pdf

[66] A. Muqaibel, A. Safaai-Jazi, A. Bayram, A. M. Attiya, and S. M. Riad, "Ultrawideband through-the-wall propagation," in *IEEE Proceedings of Microwaves, Antennas and Propagation*, Dec. 2005, pp. 581–588.

[67] J. Choi, N.-G Kang, Y.-S Sung, J.-S Kang, and S.-C Kim, "Frequency-Dependent UWB Channel Characteristics in Office Environments," *IEEE Transactions on Vehicular Technology*, vol. 58, no. 7, pp. 3102–3111, Sep. 2009.

[68] W. Q. Malik, D. J. Edwards, and C. J. Stevens, "Frequency Dependence of Fading Statistics for Ultrawideband Systems," *IEEE Transactions on Wireless Communications*, vol. 6, no. 3, pp. 800–804, Mar. 2007.

[69] W. Zhang, T. D. Abhayapala, and J. Zhang, "Frequency Dependency in UWB Channel Modelling ," Scientific Commons, 2008. [Online]. Available: http://citeseerx.ist.psu.edu/viewdoc/summary?doi=10.1.1.60.5617

[70] L. Ma, "Investigation of transmission, propagation, and detection of uwb pulses using physical modeling," Ph.D. dissertation, Electrical Engineering, North Carolina State University, 2006.

[71] J. A. Dabin, A. M. Haimovich, and H. Grebel, "A statistical ultra-wideband indoor channel model and the effects of antenna directivity on path loss and multipath propagation," *IEEE Journal on Selected Areas in Communications*, vol. 24, no. 4, pp. 752–758, Apr. 2006.

[72] Z. Irahhauten, H. Nikookar, and G. J. M. Janssen, "An overview of ultra wide band indoor channel measurements and modeling," *IEEE Microwave and Wireless Components Letters*, vol. 14, no. 8, pp. 386–388, Aug. 2004.

[73] A. F. Molisch et al., "A comprehensive model for ultrawideband propagation channels," in *IEEE Global Telecommunications Conference 2005 (GLOBECOM 2005)*, Dec. 2005.

[74] A. F. Molisch, D. Cassioli, C.-C Chong, S. Emami, A. Fort, B. Kannan, J. Karedal, J. Kunisch, H. G. Schantz, K. Siwiak, and M. Z. Win, "A comprehensive standardized model for ultrawideband propagation channels," *IEEE Transactions on Antennas and Propagation*, vol. 54, pp. 3151–3166, Nov. 2006.

[75] W. C. Jakes, *Microwave Mobile Communications.* New York : Wiley, Feb. 1972.

[76] M. Ghavami, L. B. Michael, and R. Kohno, *Ultra Wideband Signals and Systems in Communication Engineering.* John Wiley and Sons, 2004.

[77] R. A. Scholtz, R. J.-M. Cramer, and M. Z. Win , "Evaluation of the propagation characteristics of ultra-wideband communication channels," in *IEEE Antennas and Propagation Society International Symposium 1998*, vol. 2, Jun. 1998, pp. 626–630.

[78] J. D. Parsons, *The Mobile Radio Propagation Channel*, 2nd ed. John Wiley and Sons, 2000.

[79] D. Shutin, "Cluster Analysis of Wireless Channel Impulse Responses," in *Int. Zurich Seminar on Communications*, Feb. 2004, pp. 124–127.

[80] D. Shutin and G. Kubin, "Cluster Analysis of Wireless Channel Impulse Responses with Hidden Markov Models," in *IEEE Internationa Conference on Acoustics, Speech, and Signal Processing*, vol. 4, May 2004, pp. 949–952.

[81] Hojoon Lee, Byungchil Han, Yoan Shin, and Sungbin Im, "Multipath characteristics of impulse radio channels," in *51st Vehicula Technology VTC 2000*, vol. 3, 2000, p. 87.

[82] O. H. Woon and S. Krishnan, "Identification of Clusters in UWB Channel Modeling," in *Proc. Of IEEE Vehicular Technology Conference 2006*, Fall 2006, pp. 1–5.

[83] J. Salo, J. Salmi, N. Czink, and P. Vainkainen, "Automatic Clustering of Nonstationary MIMO Channel Parameter Estimates," in *International Conference on Telecommunications'05*, May 2005.

[84] L. Kaufman and P. J. Rousseeuw, *Finding Groups in Data: an Introduction to Cluster Analysis.* John Wiley and Sons, Inc., 1990.

[85] W. Niu, J. Li, and T. Talty, "Ultra-wideband channel modeling for intra-vehicle environment," *EURASIP Journal on Wireless Communications and Networking*, vol. 2009, no. 806209, Mar. 2009.

[86] M.Z. Win and R. A. Scholtz, "Energy capture vs. correlator resources in ultra-wide bandwidthindoor wireless communications channels," in *MILCOM 1997 Proceedings*, vol. 3, Nov. 1997, pp. 1277–1281.

[87] M. Z. Win and Z. A. Kostic, "Impact of spreading bandwidth on RAKE reception in dense multipathchannels," *IEEE Journal on Selected Areas in Communications*, vol. 17, no. 10, pp. 1794–1806, Oct. 1999.

[88] M. Choi and A. A. Abidi, "A 6 b 1.3 GSample/s A/D converter in 0.35 μm CMOS," in *2001 IEEE International Solid-State Circuits Conference*, Feb. 2001, pp. 126–127.

[89] P. P. Newaskar, R. Blazquez, and A. R. Chandrakasan, "A/D precision requirements for an ultra-wideband radio receiver," in *IEEE Workshop on Signal Processing Systems 2002*, Oct. 2002, pp. 270–275.

[90] L. Ke, H. Yin, W. Gong, and Z. Wang, "Finite-resolution digital receiver design for impulse radio ultra-wideband communication," *IEEE Transactions on Wireless Communications*, vol. 7, no. 12, pp. 5108–5117, Dec. 2008.

[91] S. Franz and U. Mitra, "Quantized UWB transmitted reference systems," *IEEE Transactions on Wireless Communications*, vol. 6, no. 7, pp. 2540–2550, Jul. 2007.

[92] J. Tang, Z. Xu, and B. M. Sadler, "Performance analysis of b-bit digital receivers for TR-UWB systems with inter-pulse interference," *IEEE Transactions on Wireless Communications*, vol. 6, no. 2, pp. 494–505, Feb. 2007.

[93] A. B. Sripad and D. L. Snyder, "A necessary and sufficient condition for quantization errors to be uniform and white," *IEEE Transactions on Acoustics, Speech, and Signal Processing*, vol. 25, no. 5, pp. 442–448, Oct. 1997.

[94] S. Hoyos, B. M. Sadler, and G. R. Arce, "Monobit digital receivers for ultrawideband communications," *IEEE Transactions on Wireless Communications*, vol. 4, no. 4, pp. 1337–1344, Apr. 2005.

[95] "Riemann Integral," Wolfram MathWorld. [Online]. Available: http://mathworld.wolfram.com/RiemannIntegral.html

PUBLICATIONS

[1] W. Niu, J. Li and T. Talty, "Intra-Vehicle UWB Communication Testbed," in *IEEE Military Communications Conference 2007 (MILCOM 2007)*, Oct. 2007, pp. 1-6.

[2] W. Niu, J. Li and T. Talty, "Intra-vehicle UWB Channel Measurements and Statistical Analysis," in *IEEE Global Telecommunications Conference 2008 (GLOBECOM 2008)*, Dec. 2008, pp. 1-5.

[3] W. Niu, J. Li and T. Talty, "Intra-vehicle UWB Channels in Moving and Stationary Scenarios," in *IEEE Military Communications Conference 2009 (MILCOM 2009)*, Oct. 2009, pp. 1-6.

[4] W. Niu, J. Li and T. Talty, "Ultra-wideband Channel Modeling for Intra-vehicle Environment," *EURASIP Journal on Wireless Communications and Networking*, vol. 2009, Article ID 806209, 12 pages, 2009.

[5] W. Niu, J. Li, et al, "Simulating Ultra-wideband Imaging for the Early Detection of Tissue Injury," in *2009 SPIE Medical Imaging Conference*, vol. 7258, Feb. 2009.

[6] M. Corrigan, A. Walton, W. Niu, J. Li and T. Talty, "Automatic UWB Clusters Identification," in *2009 IEEE Radio and Wireless Symposium*, Jan. 2009, pp. 376-379.

[7] W. Niu, J. Li and T. Talty, "Quantization of UWB TR Receiver with Slightly Frequency Shifted Reference," accepted to *2011 IEEE Radio and Wireless Symposium*, 2011.

[8] W. Niu, J. Li and T. Talty, "Performance Analysis of Quantized UWB Systems with Slightly Frequency-Shifted Reference," submitted to *IEEE Transactions on Wireless Communications*.